The Investigation of Isomers using Differential Mobility Spectrometry and Ultraviolet Photodissociation Spectroscopy

by

Nour Mashmoushi

A thesis

presented to the University of Waterloo

in fulfillment of the

thesis requirement for the degree of

Doctor of Philosophy

in

Chemistry

Waterloo, Ontario, Canada, 2022

Examining Committee Membership

The following served on the Examining Committee for this thesis. The decision of the Examining Committee is by majority vote.

Supervisor	Dr. W. Scott Hopkins Associate Professor Department of Chemistry, Faculty of Science University of Waterloo, Waterloo, ON, Canada
Internal Member	Dr. Germán Sciaini Associate Professor & Canada Research Chair in Atomically Resolved Dynamics and Ultrafast High-Resolution Imaging Department of Chemistry, Faculty of Science University of Waterloo, Waterloo, ON, Canada
Internal-external Member	Dr. Brendan McConkey Professor of Biology Department of Biology, Faculty of Science University of Waterloo, Waterloo, ON, Canada
External Examiner	Dr. Lars Konermann Professor Department of Chemistry, Faculty of Science The University of Western Ontario, London, ON, Canada
Other Members	Dr. J. Larry Campbell Adjunct Professor Department of Chemistry, Faculty of Science University of Waterloo, Waterloo, ON, Canada Cofounder Bedrock Scientific Inc, Milton, ON, Canada

Author's Declaration

This thesis consists of material all of which I authored or co-authored: see Statement of Contributions included in the thesis. This is a true copy of the thesis, including any required final revisions, accepted by my examiners.

I understand that my thesis may be made electronically available to the public.

Statement of Contributions

I, Nour Mashmoushi, was the sole author for Chapters 1, 2, and 6, which were written under the supervision of Dr. W. Scott Hopkins and were not written for publication. My contributions to other chapters relating to this thesis are summarized below:

Research presented in Chapter 3:

Chapter 3 is reproduced from the following publication:

Mashmoushi, N; Campbell, J. L.; di Lorenzo, R.; Hopkins, W. S. Rapid separation of cannabinoid isomer sets using differential mobility spectrometry and mass spectrometry. Analyst **2022**, 147, 10, 2198-2206.

My contributions to this work include conducting the computational and experimental investigations. Drs. Campbell and di Lorenzo provided chemical standards for the study. Dr. W. S. Hopkins supervised the study and aided in preparation of the manuscript for publication.

Research presented in Chapter 4:

Chapter 4 was written under the supervision of Dr. W. Scott Hopkins and is written for future publication. My contributions to this work includes conducting the computational and experimental investigations of the isomers. Dr. Neville Coughlan participated in conducting experimental investigations. Dr. Scott Hopkins supervised the study and aided in the preparation of the manuscript for publication.

Research presented in Chapter 5:

Chapter 5 is reproduced from the following publication:

Mashmoushi, N; Juhasz, D. R.; Coughlan, N. J. A.; Schneider, B. B.; Le Blanc, J. C. Y.; Guna, M; Ziegler, B. E.; Campbell, J. L.; Hopkins, W. S. UVPD spectroscopy of differential mobility-selected prototropic isomers of Rivaroxaban. The Journal of Physical Chemistry A **2021**, 125, 37, 8187–8195

My contributions to this work include conducting the computational and experimental investigations. Dr. Coughlan and Dan Juhasz aided in some experimental studies. Dan Juhasz also performed some computational optimizations of the proposed structures. Dr. Scott Hopkins supervised the study and aided in preparation of the manuscript for publication.

Abstract

The analysis of complex mixtures in mass spectrometry (MS) is often complicated by the presence of isomers exhibiting the same mass-to-charge ratios. Tandem MS can simplify isomer analysis and enable ion characterization based on their fragmentation patterns. While mass spectrometry dominates the analysis of samples in various fields, it is often paired with orthogonal separation methods to allow for the analysis of complex mixtures. This workflow improves sample throughput for analysis by minimizing time-consuming steps involving sample preparations and modifications required to create distinct fragmentation patterns.

The studies detailed in this thesis investigate differential mobility spectrometry (DMS) as a tool for separating and characterizing isomeric species prior to MS. Often used as a prefilter to mass spectrometry, DMS is a variant of ion mobility spectrometry (IMS) that employs an asymmetric electric field to separate ions based on their differential mobility using alternating regions of high- and low-field strength. The resolving power of DMS can be enhanced by the introduction of polar neutral molecules into the gas phase to induce intermolecular interactions with the ions. The resulting gas-phase clusters and dynamic processes taking place in the DMS are dependent on the physicochemical properties of the analytes. With isomers, subtle differences in their properties can be leveraged to induce large differences in the ion behaviour in the DMS. In turn, the DMS behavior of ions can be reverse traced to probe the physicochemical properties of the analytes in the gas phase.

In this thesis, different isomeric species are investigated, separated, and characterized using DMS-MS. Thorough investigations are conducted to understand the gas-phase behaviour of ion clusters in the DMS, and computational studies are conducted concurrently to rationalize the observations made. We also probed the electronic structure of DMS-isolated compounds with ultraviolet photodissociation (UVPD) spectroscopy, as while DMS helps separate isomers prior to MS, UVPD can be used to distinguish isomers that are otherwise indistinguishable by tandem MS. The instrumental setup is employed in

the study of functional isomers, prototropic isomers and conformers, along with positional isomers.

In this thesis, isomers that were challenging to distinguish by MS techniques alone were separated using DMS. Five main cannabinoid isomers are separated by seeding the carrier gas of the DMS with polar solvent vapor. In the case of these ions, it was determined that the composition of the electrospray ionization (ESI) solvent and the polar solvent vapor influenced the survival of ESI-formed adducts. Next, positional isomers, nortriptyline and protriptyline were used to assess the use of DMS-MS coupled with UVPD in the characterization of isomers that present the same fragment ions. UVPD analysis yielded stark differences in their photodissociation efficiencies. Lastly, prototropic isomers of Rivaroxaban—a drug molecule—formed during the ESI process were preserved in the DMS and characterized via UVPD. The coupling of DMS and UVPD to MS provided additional tools in the separation, quantification, and characterization of isomers.

The distinct uses of DMS in the analysis of various isomers are highlighted. Identification and characterization were made easier with the ability to probe the interaction potentials of the isomers with solvent modifiers in the DMS and the ability to probe their electronic structures via UVPD.

Acknowledgements

First and foremost, I would like to acknowledge my supervisor, Dr. W. Scott Hopkins, whose never-ending support and guidance has helped in my growth throughout my PhD studies. Without his support, knowledge, and expertise, I would not have gotten to where I am today.

I would like to thank my committee members, Dr. J. Larry Campbell and Dr. Gérman Sciaini, who took time to provide me with advice throughout my PhD. Dr. Campbell has greatly improved my understanding of the DMS and has helped with advice regarding my projects. Dr. Sciaini has helped in my understanding of fundamentals of spectroscopy and laser setups. I would also like to thank Dr. Wojcech Gabryelski for taking part in my advisory committee. Next, I would like to acknowledge my external examiners, Dr. Lars Konermann and Dr. Brendan McConkey for reviewing and critiquing this thesis.

Throughout my PhD, I have had help from several coworkers and colleagues, whose suggestions and insights have expanded my knowledge in the field. Dr. Neville Coughlan, Dr. Alex Haack, and Dr. Jeffrey Crouse, have all been instrumental in my academic career and their advice has helped me find my way with work and experimentation. I would like to further extend my gratitude to Dr Coughlan, Dr. Haack, and Arthur Lee who have not only taken the time to support just me, but also anyone else who would have troubles within the Hopkins group. I am truly grateful for not only their expertise, but also the rapport that I have built with them. Furthermore, I have learned a great deal from my colleagues Christian Ieritano, Arthur Lee, Daniel Rickert, and Cailum Stienstra and I am very glad that we have grown within the same academic family. I'd also like to acknowledge alumni from the Hopkins group: Yuting Li, Su Ji Lim, Weiqiang Fu, Fiorella Villanueva. All of those mentioned here have been great friends, coworkers, and sometimes much needed critics.

Lastly, I would like to acknowledge my family and friends for their support beyond the scope of my PhD. Especially Gabi, Denzel, Mark, and Henry, for always being available whenever I needed help.

Table of Contents

List of Figures

List of Abbreviations

ACE	Acetone
B3LYP	Becke-3-Lee-Yang-Parr
BH	Basin Hopping
BO	Born-Oppenheimer
CAM	Coulomb attenuated method
CBC	Cannabichromene
CBD	Cannabidiol
CBDA	Cannabidiolic acid
CCS	Collision cross section
CE	Collision energy
CID	Collision induced dissociation
CV	Compensation voltage
DC	Direct current
DFT	Density functional theory
DMS	Differential mobility spectrometry
DNA	Deoxyribonucleic acid
DP	Declustering potential
ECD	Electron capture dissociation
ECT	Excited charge transfer
EID	Electron induced dissociation
ESI	Electrospray ionization
FAIMS	High field asymmetric waveform ion mobility spectrometry
FC	Franck-Condon
FCF	Franck-Condon factors
GC	Gas chromatography
HDX	Hydrogen deuterium exchange
HO	Harmonic oscillator

HOTO	Highest occupied transition orbital
HPLC	High performance liquid chromatography
IMS	Ion mobility spectrometry
IPA	Isopropyl alcohol
IR	Infrared
LC	Liquid chromatography
LIT	Linear ion trap
LUTO	Lowest unoccupied transition orbital
MeCN	Acetonitrile
MeOH	Methanol
MM	Molecular mechanics
MO	Molecular orbital
MRM	Multiple reaction monitory
MS	Mass spectrometry
MS^n	Tandem mass spectrometry
NTO	Natural transition orbital
OPO	Optical parametric oscillator
PA	Projection approximation
PCM	Polarizable continuum models
PES	Potential energy surface
RF	Radiofrequency
SID	Surface induced dissociation
SV	Separation voltage
THC	Tetrahydrocannabinol
THCA	Tetrahydrocannabinolic acid
TM	Trajectory method
UFF	Universal force field
UV	Ultraviolet
UVPD	Ultraviolet photodissociation

VDW	van der Waals
VG	Vertical gradient
VIS	Visible

Chapter 1: Motivation

1.1 The Interest in Isomer Investigation

There is an increasing demand for the development of comprehensive and efficient diagnostic screening methods for industrial, medical, environmental, and research sectors.[1] Currently, analyte characterization requires extensive preparation of acquired sample mixtures prior to analysis, and is inefficient, non-comprehensive, and offers little opportunities to explore molecular interactions through property investigations. Furthermore, the applicability of analytical workflows that employ conventional techniques is limited by their ability to resolve compositionally identical but structurally distinct molecules, i.e. isomers. Although subtle, these structural differences between isomers can result in varying physicochemical properties that lead to contrasts in functionalities and biological activities.[2–4]

Isomers can be grouped into several categories. The simplest cases are conformers, which are sets of molecules that share the same molecular formula and connectivity but differ by their 3D configuration and intramolecular interactions. This is especially prevalent in large molecules and is a central theme of research in the field of proteomics, as conformational changes to protein structures dictate the activity of the protein.[5,6] On a similar note, sets of molecules that share the same molecular formula but differ in connectivity are known as functional isomers. Differences in connectivity can lead to dramatic shifts in the physicochemical behaviour of the molecule.[7] A subset of functional

isomers are sets of molecules that differ by double bond placement or configuration (cis or trans) and are referred to as configurational isomers. Another subset of interest includes prototropic isomers, which differ by the location of the protonated site. While other isomeric types exist, they are beyond the scope of this thesis and will not be discussed.

The many possible configurations of isomeric species can lead to an immense array of permutations for a given molecular formula. Studies of various biologically relevant isomers have demonstrated that minute differences in the connectivity of isomers can lead to substantial changes in their physicochemical behaviour.[2] As such, the expression of different isomeric species can result in significant and observable biological effects. For instance, the presence of tautomers in nucleobase analogues of DNA have been linked to the survival of genetic mutations.[8,9] In physiological conditions, in which nucleobases can be protonated, the site of protonation influences the intermolecular interactions present between the nucleobases of each DNA strand. Proton transfers into an uncommon site may affect the Watson-Crick base pairing and hence the structural integrity of DNA.[8,9] The distinction of the tautomeric forms of nucleobases is therefore relevant to understand the mechanisms of DNA mutations and folding.

Research in the field of metabolomics presents several studies that have linked the expression of metabolite isomers to the health of the individual.[10,11] In the case of positional isomers, the increased presence of the n-6 fatty acids was correlated to a reduced risk in heart disease in adult patients.[12] While the mechanism of action responsible for the correlation to risk is not yet known, it is evident that distinguishing isomeric pairs is necessary when developing diagnostic methods. Improved diagnostic methods result in further understanding of the effects of the physiological conditions on the expression of metabolites and vice versa.

Ultimately, determining isomer-specific behaviour provides valuable insight into functional groups and their effects on the properties of a molecule. Furthermore, information on the differences in interactions between isomers in a given environment can be used to improve separation and characterization methodologies. Probing the properties

of a molecule, such as its biological activity, can be achieved via thorough investigations in the gas or solution phase. However, to perform isomer characterization, techniques such as mass spectrometry must first be employed to conclusively distinguish between analytes of interest.

1.2 Mass spectrometry in the analysis of isomers

Mass spectrometry (MS) is a widely used technique for the detection and quantification of ions. Within MS, ions in vacuum are separated and isolated by their mass-to-charge ratios (m/z) in the presence of an electric or magnetic field.[13] Analytes in sample mixtures are resolved by m/z with accuracies dependent on the MS instrument employed (e.g., quadrupole,[14] time-of-flight,[15] orbitrap,[16] etc.). However, the prevalence of isomers and isobars—or molecules possessing the same nominal mass—in complex mixtures complicates the application of MS. Tandem mass spectrometry (MS^n) is typically used to distinguish isomers, where ions can be fragmented, and their characteristic product ions identified. As isomers of different connectivity may produce different fragments or fragmentation patterns, tandem MS addresses the issue by distinguishing isomers based on their m/z values.

The information acquired from tandem MS is heavily dependent on the collision technique employed. In collision-induced dissociation (CID), ions are accelerated through the collision cell to collide with an inert collision partner (e.g., N_2, Ar, He) and induce fragmentation. CID is often implemented for the analysis of structural isomers due to its simplicity and versatility.[17] Surface-induced dissociation (SID) involves the fragmentation of ions through their acceleration and collision with a surface. SID has proven useful for the structural analysis of proteins and complexes by sequentially cleaving the weakest connections.[18] CID and SID may result in different fragmentation patterns when investigating multiply-charged ions, providing similar but at times complementary information. Evidence of this is shown in studies that employ SID to provide information on the connectivity between complexes.[19] Another form of MS^n techniques involves the use of electron capture dissociation (ECD). The analysis of ions via ECD presents an additional

means for the analysis of fragmentation patterns. ECD analysis of peptides leads to the production of fragments not observed in CID. As such, a more thorough mapping of the peptide 2D structure can be achieved. Additionally, ECD preserves intermolecular bonding, providing greater information into the intramolecular interactions and thus the 3D structures of peptides and proteins.[20]

MS analysis is a ubiquitous analytical technique because of its wide applicability. Tandem MS techniques can simplify and sometimes enable the isomer analysis by identifying characteristic fragmentation patterns. However, given the innumerable possible isomers present in some complex sample mixtures, the characterization and separation of all possible isomers in a sample is still unattainable. As such, orthogonal separation techniques are typically added prior to MS to alleviate this limitation. Chromatographic techniques, such as liquid chromatography (LC)[21,22] and gas chromatography (GC)[23], are well-known methods introduced prior to MS.

MS coupled with LC or GC have expanded the capabilities of isomer separation, making these setups widely adopted for the analysis and quantitation of complex mixtures. However, to probe the behaviour of isomers, instrumentation that provides more than just structural information is required. Probing other physicochemical properties of isomers beyond structure improves our understanding of how structural, conformational, and configurational changes affect the interaction potentials and mechanisms of ions. In turn, this new information proves useful for future use in areas such as targeted diagnostic methods and targeted product design.

1.3 Scope of this thesis

In this thesis, differential mobility spectrometry (DMS) coupled with ultraviolet photodissociation (UVPD) is explored as an orthogonal technique to MS to probe differences in isomer behavior for several biologically relevant compounds. Each method is evaluated for their capabilities and limitations. DMS is a variant of ion mobility spectrometry (IMS) that employs an asymmetric radiofrequency waveform to separate ions

based on their mass, size, and charge.[24] DMS operates in atmospheric pressures, and allows for the probing of gas-phase clusters and utilization of the characteristic interaction potentials within clusters to separate isomeric species.[24,25] This work will show that DMS and UVPD are useful orthogonal tools to MS, not only to separate isomeric species, but to also provide greater insight into the physicochemical properties of gas-phase ions.

Chapter 2 details the theory and background behind experimental and computational methods employed. We delve into the dynamics of clustering and declustering that occur in the DMS and the physicochemical behaviours that lead to differences in the clustering behaviour. The effect of electrospray ionization (ESI) as a form of introducing ions into the DMS is also discussed, as the presence and yield of ion-solvent adducts are affected by the makeup of the solvent and ESI parameters. Additionally, the mechanisms, setup, and uses of UVPD are described.

In Chapter 3, DMS-MS is examined as a tool for separating two structural cannabinoid isomer sets: (1) tetrahydrocannabinol (THC), cannabidiol (CBD), and cannabichromene (CBC), and their acidic counterparts (2), tetrahydrocannabinolic acid (THCA) and cannabidiolic acid (CBDA). It is found that the chemical composition of the ESI solvent and the gas-phase environment of the DMS influence the separation capabilities of the DMS for the cannabinoid compounds. The favourability in the survival of ESI-formed adducts through the DMS were heavily influenced by two factors: the interaction potentials experienced by the ion to the ESI solvent, and the neutral solvent vapor in the DMS. The separation of the structural isomers was attributed to differences in the isomers' binding strengths towards neutral solvents introduced into the DMS.

Chapter 4 studies positional isomers, nortriptyline and protriptyline, by coupling the DMS-MS instrument to UVPD. Upon analysis with tandem MS, nortriptyline and protriptyline presented the same fragment ions. To separate the isomers, the DMS carrier gas was seeded with a polar solvent modifier that allowed subsequent analysis using UVPD. UVPD analysis of the isomers yielded distinct spectra that were complemented by vibronic spectra calculations. It was also noted that the two isomers yielded different

fragmentation efficiencies. It is concluded therein that the use of UVPD allows for a simplified means of quantification and identification for future use.

Lastly, in Chapter 5 the coupling of DMS-MS with UVPD was employed for the characterization of prototropic isomers of Rivaroxaban, an anticoagulant drug molecule. ESI and DMS conditions were found to affect the yield and population of ESI-formed prototropic isomers of Rivaroxaban. Although CID failed to distinguish the isomers, UVPD analysis conclusively identified separation of the ion populations by their action spectra. The techniques showcased can be applied to other prototropic isomers or conformers that yield different intramolecular interactions.

Chapter 2: Background and Theory

In this chapter, the background and theory behind the main experimental and computational setups used in the investigation of isomers are discussed. To best understand the applications of each method, certain considerations and drawbacks are also highlighted.

2.1 The Investigation of Analytes in the Gas Phase

Considerations must be taken when characterizing biologically relevant molecules in the gas phase, as the gas-phase behaviour may starkly differ from those observed in solution phase. It is thus important to not only consider the differences between gas-phase and solution-phase properties, but to also induce a gas-phase environment that most resembles the environment observed in solution phase. The use of differential mobility spectrometry, which will be discussed in detail in Section 2.3, overcomes this challenge by inducing microsolvation in the cell.[26,27] The generation of microsolvated states may help preserve solution-dependent conformations that are otherwise lost in the gas phase.[28,29] However, the population and preservation of isomers are highly dependent on the conditions used during ionization, and a suitable ionization technique is required to maintain the structural integrity of the ions in question. Employing electrospray ionization as the ionization technique addresses the presented issues.

2.1.1 The Ionization of Analytes via ESI

A wide range of ionization methods are available to introduce analytes into the gas phase for MS analysis.[30–32] Popular ionization methods such as electron impact (EI) ionization and matrix assisted laser desorption ionization (MALDI) present several

limitations in the analysis of ions for solution-phase properties. EI involves the bombardment of gaseous/volatile analytes with a high-voltage electron beam. This high energy process can lead to fragmentation of the ions, which may be undesirable but may also present the opportunity to observe characteristic fragmentation patterns for a given ion.[30] This is because the subsequent fragmentation of ions presents a challenge for analyzing the geometric structure of the intact parent species. As such, EI is largely used in the identification of analytes by their fragmentation patterns. Additionally, EI requires the analysis of gaseous or volatile analytes, which is sometimes challenging for solution-phase species and can hinder structural analysis of some samples in solution.[31,33]

Soft ionization techniques are required in the case of many biologically relevant molecules to prevent in-source fragmentation or structural rearrangement during the ionization process. Employing ionization methods that generate clusters to be preserved in the gas phase provides an added advantage of gaining greater insight into the mechanisms taking place in the interaction potentials between isomers. In this regard, two main soft ionization techniques are commonly used: atmospheric pressure chemical ionization (APCI) and electrospray ionization (ESI). Both involve the ionization of analytes via proton transfer between chemical reagents or solvents and the analytes.[31] For cationic species, this is done by protonation, and for anionic species, deprotonation.[31] Within the scope of this thesis, ESI is discussed, with details on the process of APCI available for referenced elsewhere.[30]

ESI provides a soft ionization mechanism that can preserve the structure of the parent ion and limit ionization-induced fragmentation.[34] ESI is an ionization technique used in the analysis of samples ranging from organic compounds to inorganic compounds.[30–32] ESI also addresses the limitations of MS studies of large ions—such as proteins and peptides—by lowering *m/z* through generation of ions with multiple charges.[34] In ESI, charged droplets are generated by the application of a high voltage about a capillary (see Figure 2-1). The applied electric field results in the separation of charge at the solution. As a result, the solvent at the capillary tip takes the shape of a Taylor cone, from which charged droplets are expelled. Charges are concentrated on the surface of the solvent, where the

electrochemical process of charge formation is concentrated. As the Taylor cone reaches the Rayleigh limit, or the point at which repulsive forces of the charges equals the opposing forces of the solvent surface tension, the ejection of droplets occurs.[34,35] The droplets released into the atmospheric pressure then experience gradual solvent evaporation, resulting in an increase in charge density about the shrinking droplet surface. The Rayleigh limit is once again reached, leading to Coulombic fission, or the generation of multiple smaller droplets from the parent charged droplets. The solvent evaporation process and Coulombic fission events are repeated until a single charged ion or ion-solvent adduct is formed that can be analyzed further by MS.[30,34] Modern discourse however is concentrated on the mechanisms of ionization post droplet formation. While several mechanisms have been proposed, two main mechanisms encompass the modes of ionization relevant to the scope of this thesis.[36,37]

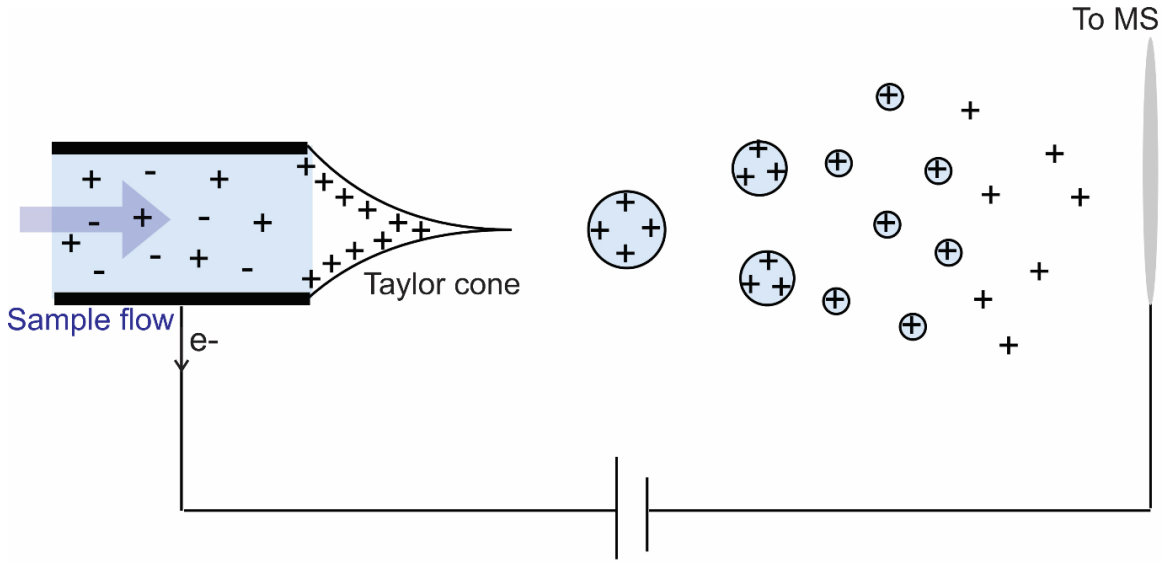

Figure 2-1. Electrospray ionization is formed from the formation of charged droplets emitted from the Taylor cone that experience graduation solvent evaporation until the Rayleigh limit is reached leading to Coulombic fission.

The ion ejection model (IEM) of low mass species (and those covered in this thesis) theorizes that charged species are generated by the gradual ejection of solvated ions due to the high electric field.[36] While ions experiences attraction forces towards the charge created as a result of the polarization of surrounding solvent molecules, this attraction is overcome

by the excess charge in the droplet that ejects the ion out of the droplet. The ejected ion is often microsolvated and is partially desolvated post-ejection as it enters the vacuum manifold of the MS. In IEM, ions positioned towards the surface of the droplet (surface-active ions) are more likely to be ejected and hence observed. Ions located closer to the center of the droplet experience greater forces, preventing ejection.

The charged residue model (CRM) describes the behavior of large molecules comparable to the size of the Rayleigh droplet. Large molecules, such as globular proteins, are found in the interior of the droplet and are ionized by the gradual desolvation of the surrounding solvent molecules.[36,37] As the solvation shells are evaporated, the residual charge of the droplet is transferred to the analyte. As a result, a multiply charged ion is formed with an overall charge approaching the Rayleigh charge of the droplet.[36] CRM is typically attributed to the ionization of structured proteins.[36,37]

Adjusting the source parameters in ESI greatly affects ion signal and the detected adduct, and can be altered to populate or to destabilize geometric structures and protomers of ions.[38,39] The selected solvent system for ESI may at times influence the observed isomer populations as a result of the proton transfer reactions taking place.[39,40] As such, ESI often generates a wide distribution of conformers that can be further investigated by gas-phase techniques. Gas-phase techniques, such as MS and ion mobility, are available for probing various properties of the isomers.

2.1.1.1 The Significance of ESI

The soft ionization of ESI presents opportunities for the investigation of gas-phase clusters. Due to the preservation of electrostatic interactions, the observation and analysis of ion-solvent adducts is possible.[41] As such, one can investigate the gas-phase conformers of analytes as they pertain to their solution-phase structures.[42] Novel modifications to ESI offer the ability to conduct kinetic studies on ion behaviour. The incorporation of rapid mixing systems prior to ESI can be used to monitor conformational changes of analytes.[43] Additionally, variable temperature ESI, in which the temperature of the capillary needle can be fine-tuned, has expanded the applicability of kinetic studies of ESI. Variable

temperature ESI in recent studies provided greater detail into temperature effects on the conformation of analytes.[44,45] With the advantages of ESI stated, the coupling of ESI to ion mobility—and more specifically to atmospheric IMS—has become more desirable than other ionization methods, as ion-neutral adducts and ion conformers can be carried through and better preserved for in-depth characterization.

2.2 Ion Mobility Spectrometry

Ion mobility spectrometry (IMS) is a gas-phase chromatographic method used to separate ions based on their size, charge, and mass.[46] In IMS, ions are driven towards a detector by the force of an electric field potential, with a drift velocity, v_d, that is proportional to the strength of the electric field, E, and the mobility of the ion, K (equation 2-1):[46]

$$v_d = K\vec{E} \qquad [\ 2\text{-}1\ ]$$

As ions are guided through the cell by the electric field potential, they collide with neutral gas molecules (i.e., the collision gas) that are introduced into the cell. As a result of momentum transfer, ions yield a loss in kinetic energy.[47] Therefore, the ion mobility, K, is also affected by the number density of the gas molecules and the resulting collision cross section (CCS) of the ion-neutral complex. The Mason-Schamp equation defines the factors affecting ion mobility and is shown in equation 2-2:[47]

$$K(0) = \frac{3q}{16N}\sqrt{\frac{2\pi}{\mu k_B T}}\frac{1}{\Omega^{(1,1)}(T)} \qquad [\ 2\text{-}2\ ]$$

where q describes the charge of the ion, N is the number density of the drift gas, μ is the reduced mass of the ion and the collision gas, k_B is the Boltzmann constant, T is the temperature, and Ω is the CCS of the ion-neutral pair. As IMS typically separates ions based on differences in their CCS, the factors leading to different CCS values must be considered.

2.2.1 The Collision Cross Section

The ion-neutral CCS provides information on the overall structure of the ion and its interaction potential about the surrounding environment. More specifically, the CCS relates to the orientationally averaged collisional overlap area between two particles.[48,49] For a pair of particles, the collision cross section is dependent on the impact parameter and the final scattering angle.[48,49] These parameters are in turn dependent on the conformation and orientation of the particles. Thus, the collision cross section represents an average of all the conformations, orientations, and scattering parameters involved between the particle pair. In the case of an ion-neutral pair, the CCS is also affected by the long-range interactions at play (i.e., ion-induced dipole interactions, ion-quadrupole interactions, and van der Waals interactions).[48–50] These interactions affect the trajectory of the colliding neutral gas molecules. Therefore, the CCS of an ion-neutral pair can lead to multiple scattering paths, as are depicted in Figure 2-2.

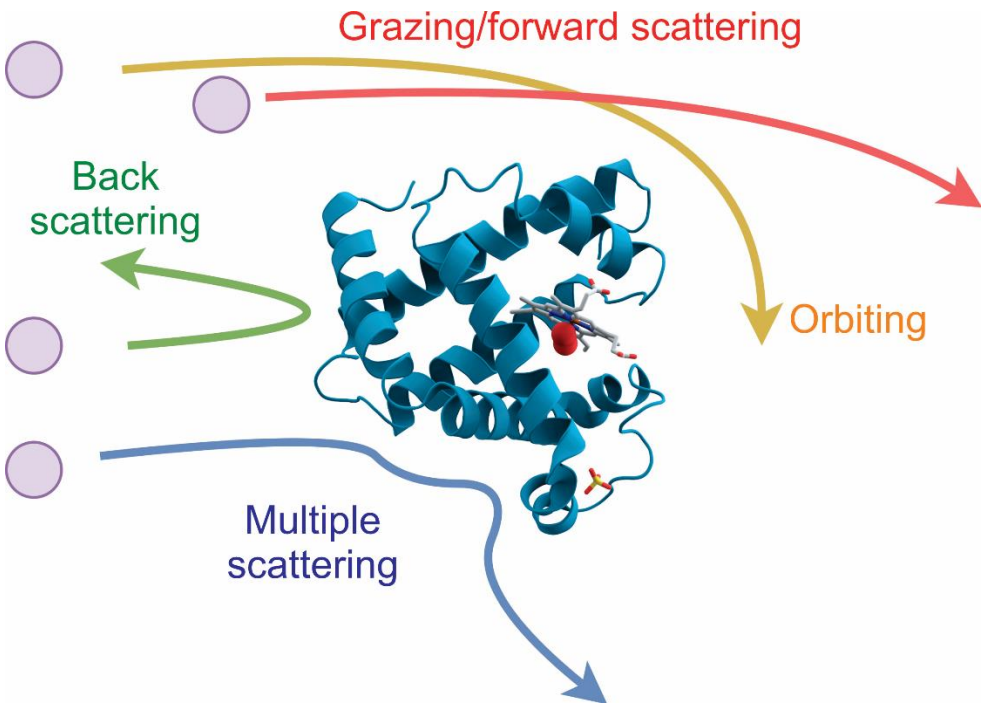

Figure 2-2. The scattering paths of neutral molecules taken upon collision/interaction with an ion.

In drift-tube IMS, the CCS can be directly related to the arrival time distribution of the analyte ion and the electric field potential, proving IMS to be a useful probe for the structure

of an ion.[51,52] The identity of the neutral gas can be altered to modify the CCS of the ion-neutral pair, improving the resolving power of IMS between ions of similar CCS values.[53] The experimentally determined CCS values can then be compared with computationally predicted CCS to identify the conformation of the ion of interest.

2.2.2 Variants of IMS

Variants of IMS involve the modification of the instrumental setup to offer different ways of separating molecules based on their size and interactions in the environment presented. One variant of IMS, the trapped IMS (TIMS), includes the trapping of ions carried through the cell by a flow of neutral gas using a DC voltage ramp.[54,55] The DC voltage is then gradually lowered to release and separate ions based on their CCS values.[54] The effective trapping of ions in the TIMS setup can be applied to the investigation of ion reactions.

Another variation includes modifying the electric field. Two main modifications used at present include the use of a travelling wave to separate ions based on their CCS and the use of an alternating electric field with high- and low-strength portions to separate ions based on their differential ion mobilities. In the former, the travelling wave (TWIMS) instruments applies various DC voltages to a series of rings to generate a wave that pushes the ions forward. One can modify parameters of the travelling wave to better resolve ions of closer CCS values. Detailed information on TWIMS are found elsewhere.[56]

The introduction of an alternating electric field is also observed in high field asymmetric waveform ion mobility spectrometry (FAIMS), which employs an alternating radiofrequency waveform across two electrodes to induce separation of ions based on their clustering behaviour at high and low electric fields.[24-26] FAIMS instruments can be found in two configurations: cylindrical and planar FAIMS, also known as c-FAIMS and p-FAIMS, respectively. The geometry of the FAIMS instrument can affect the homogeneity of the electric field across the cell, leading to differences in ion transmission.[35] Planar FAIMS, now referred to as differential mobility spectrometry (DMS) is used extensively in the scope of this thesis and will be discussed in the next section.

2.3 Differential Mobility Spectrometry

Differential mobility spectrometry (DMS) is a variant of IMS that takes advantage of the nonlinear dependence of the ion mobility on an applied electric field to affect ion separation.[24] In DMS, an asymmetric radiofrequency waveform composed of portions of high and low electric field is applied across two planar electrodes. Ions are carried through the cell by neutral gas molecules referred to as the carrier gas (typically N_2). As ions traverse the cell, the amplitude of the asymmetric waveform known as the separation voltage (SV) causes an off-axis shift in the ion trajectory.[24,25] The extent of the shift is dependent on the differential ion mobility between the high and low field portions of the waveform and leads to the neutralization of ions upon collision with one of the electrodes. To allow transmission, a direct current, known as the compensation voltage (CV), is applied. The magnitude of the CV required for ion transmission is dependent on the extent of off-axis trajectory of the ion and is characteristic of the ion's differential mobility and can be used in the separation of isomers.[24]

It is important to note that the ion mobility under low electric field (<30 Td) is proportional to the electric field strength. At high electric fields, the ion mobility exhibits a nonlinear dependence on the electric field strength, and can be described by equation 2-3:[57]

$$K\left(\frac{E}{N}\right) = K(0)\left[1 + \alpha_2\left(\frac{E}{N}\right)^2 + \alpha_4\left(\frac{E}{N}\right)^4 + \cdots\right] \qquad [\ 2\text{-}3\ ]$$

where $K(0)$ describes the zero-field ion mobility coefficient (representative of electric field effects below 10 Td), and α is a function that described the ion mobility dependence on the electric field. The increase in $\frac{E}{N}$ in the high-field portion of the DMS waveform requires an expansion of the effective temperature in the cell to account for the field contribution, as shown in equation 2-4:[47]

$$T_{eff} = T_{gas} + T_{field} = T_{gas} + \frac{M}{3k_B}v^2, \qquad [\ 2\text{-}4\ ]$$

where M is the mass of the neutral gas species, k_B is the Boltzmann constant, and v is the drift velocity. In equation 2-4, not only is the effective temperature, T_{eff}, related to the temperature of the bath gas, T_{gas}, but it is also dependent on the field-induced heating, T_{field}. Field-induced heating then influences the ion mobility during the high-field portion of the waveform through affecting CCS of the ion as a result of conformational changes and changing the strength of ion-neutral interactions.[24] With these factors considered, the ion mobility under high and low electric field defer by not just the mobility coefficient dependence on the electric field strength, but also the effective CCS under each electric field portion. As such, the differential mobility of an ion in DMS becomes dependent on the ion mobility, the effective CCS, and the rate of CCS change as the waveform progresses.

Solvent molecules can be seeded into the carrier gas to enhance the differential mobility observed. This in turn improves the separation of analytes based on the physicochemical properties of each ion.[58,59] The solvent molecules, or modifiers, can form clusters around the charged and polar sites of ions through ion-induced dipole, ion-dipole, and/or hydrogen-bonding interactions.[26] The strength of these intermolecular interactions depends on dipole moments and polarizabilities of the collision species.[26,60] As analyte ions travel through the DMS, they experience periodic clustering and declustering during low and high electric field conditions, respectively. At these varying points of the waveform, the mobility of the ion differs, owing to the fact that its CCS artificially increases with microsolvation. The stronger the interactions between the analyte and collision gas molecules, the more reduced its relative mobility at low field.[26,61] Moreover, because an ion experiences thousands of duty cycles during its transit, subtle differences in ion-solvent interactions between geometrically similar species (e.g., isomers, conformers) are greatly magnified, leading to significantly improved spatial separation.[25,58,59] Since this spatial separation is encoded in the optimal CV for ion transmission, the information of the analyte's physicochemical properties (*i.e.*, CCS, interaction potential) is also encoded.

Since it is not obvious *a priori* which chemical modifier will yield the best separation for a given analyte, it is common to screen several options. Common choices of modifier

include isopropyl alcohol (IPA), methanol (MeOH), ethanol (EtOH), acetone (ACE), acetonitrile (MeCN), and water. Given that these solvent molecules have different polarizabilities, dipole moments, etc., the interactions that take place between the analyte ions and solvent molecules vary depending on the identity of the modifier. This manifests as subtle differences in dynamic clustering and, therefore, ion trajectory.

By recording the CV value for optimal transmission at different SVs, one can generate a dispersion plot; a visual demonstration of the changing DMS behaviour for the analyte under certain environmental conditions. In addition to differential mobility data, the DMS can be coupled with a MS to facilitate the detection and further MS-based identification of the compounds in the sample.

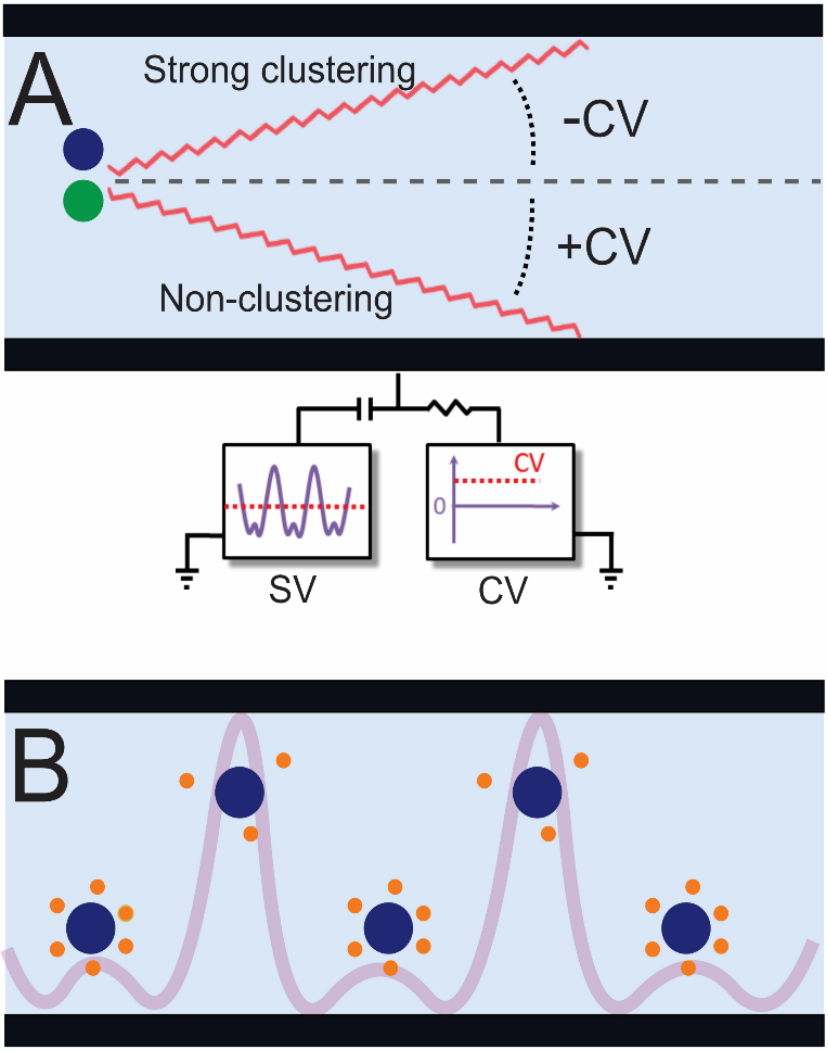

Figure 2-3. (A) A depiction of the different trajectories ions follow through the DMS, based on interactions. Ions are separated by their clustering interactions with solvent vapour in the DMS, as determined by the (B) dynamic clustering and declustering processes taking place during the low and high field portion of the SV waveform, respectively.

Generally, there are three main types of clustering behaviour observed in the DMS: Type A, B, and C. Type A clustering behaviour signifies a strong clustering interaction between the ion and molecules in the DMS cell. This leads to a reduced mobility at low fields as the cluster grows (owing to the artificially large CCS) compared to high electric fields, wherein the ion exhibits a relatively higher mobility due to declustering.[24,26] Under these conditions, the ion requires an increasingly negative CV value as SV increases to correct its trajectory. In comparison, Type C clustering behaviour is indicative of hard-sphere interaction (little clustering at low electric field).[24,26] Type C ions require a positive

CV value to correct their trajectory as SV increases. Type B behaviour is observed when ions cluster at relatively low SV but then adopt Type C behaviour at voltages above some critical SV.[24,26] This is a result of the higher SVs introducing sufficient thermal energy to dissociate the clusters formed and inhibit reformation at low field.[26] Other exotic type dispersion curves that do not follow the conventional clustering behaviours outlined are sometimes observed.[64] These curves include Type D and E behaviours, which show strongly bound ion-neutral clusters that vary in behaviour appear unaffected by the applied SV until the introduction of a critical SV point.[26] In the case of Type D clustering, the ion-neutral cluster exhibits hard-sphere behaviour at low SVs and then begins to dynamically cluster and decluster at high SV values, resulting in a curve that is the opposite to that of Type B.[26] Type E behaviour adheres to the ion-neutral cluster dynamically clustering as one entity with the modifier at low SV values. Once a critical SV point is reached, the neutral molecule is permanently desolvated leaving the ion to dynamically cluster with surrounding modifier. Details of these exotic behaviours are reported elsewhere.[26,62]

2.3.1 The Dynamic Clustering Process in DMS

Characteristic to the asymmetric waveform and the atmospheric pressure of the DMS, ions traversing the DMS cell experience dynamic clustering and declustering with the surrounding neutral gas. Ions experience thousands of dynamic clustering events in coherence with the oscillations between high- and low-electric field. The cycling of dynamic clustering enhances the spatial separation of ions based on subtle differences in their physiochemical properties. As ions collide with neutral molecules, electrostatic interactions such as ion-dipole, ion-induced dipole, and hydrogen-bonding forces, lead to attractive interactions that dictate the formation of clusters. Physicochemical properties of the ions such as resonance, steric, electronic, and geometric effects along with the polarity, polarizability, and functional groups of the neutral molecules dictate the type of interactions experienced.[63]

The clustering of ions in the DMS is heavily dependent on the conditions in the cell. At low electric field, ions cluster with N number of solvents—dependent on the forces at

play—and the binding strength of the ion-neutral interaction and the neutral-neutral interaction. A distribution of cluster sizes may exist in the DMS. Each cluster size is populated and depopulated based on the conditions in the cell and experience different ion mobilities based on their apparent CCS. Under high electric fields, large clusters are desolvated due to the induced field heating, resulting in a distribution of smaller cluster sizes. The alternating population of the various cluster sizes leads to differences in the apparent CCS of the ensemble under high- and low-electric field, adding to large differences in the differential mobility of an ion.

With the rapidly oscillating electric field, clusters populated and depopulated in the DMS are not in equilibrium. Instead, the rate of forming and desolvating of each cluster is heavily dependent on their respective rates of formation and dissociation in competition with the rate of oscillation between the field strengths.[64] As such, the faster a cluster ensemble can reach association and dissociation, the more prevalent the differential mobility under the alternating fields will be. In this case, a more Type A behavior is observed. On the other hand, clusters that cannot be formed rapidly cause little to no change in the apparent CCS of the ensemble under the two electric field strengths, and result in a more Type C behaviour.

With the inclusion of ESI-formed adducts, the clustering process in the DMS becomes more complicated. Ion-solvent adducts formed in the ESI may at times survive the rapid clustering and declustering taking place in the DMS and can be resolved from the bare ion population as a result of differences in the ensemble differential mobility. More often, due to the relatively high concentrations of the neutral solvent vapour in the DMS during modifier studies, ESI adducts are easily replaced, causing these adducts to not be detected.

2.3.3 Significance

Several studies of the analytical capabilities of the DMS in the separation of isomers have demonstrated the high resolving power of the DMS instrument, while maintaining a more cost-effective and less time-consuming workflow than conventional methods such as high-performance liquid chromatography (HPLC) for the analysis of some sample

mixtures.[63,65–67] These studies demonstrated the ability of DMS to distinguish structural isomers, stereoisomers, and tautomers through the introduction of modifiers.[40,63,65,67] In addition, DMS has been shown to provide insight with respect to structural and electronic properties.[63,68] As an example, through the study of 4-aminobenzoic acid under various modifiers, different charge sites were discovered in which protonation either occurred at the carboxylic acid or the ammonium group depending on the electrospray solvent used.[28,69] Furthermore, the DMS clustering behaviour of tetraalkylammonium species demonstrated the importance of steric effects and charge shielding on the degree of clustering observed.[70]

An important new development in DMS is the ability to relate observed gas-phase properties of an analyte to those observed in solution.[68] Investigating analyte interactions with water modifier is of particular importance, as it allows for the study of conformations and hydrogen-bonding sites available to an analyte in aqueous media. Hydrogen-deuterium exchange (HDX) experiments have also provided insight into the conformation a molecule takes, as inferred by which hydrogens are most labile and accessible.[71] Note, however, that to thoroughly investigate gas-phase interaction and reliably predict analyte properties in solution, computational analyses must be employed.

2.4 Computational Investigations of Gas-Phase Reactions

Computational calculations of the likely ion structures taking form in the DMS complement experimental findings to better understand and rationalize the behaviour observed.

2.4.1 Geometry Optimizations

Determining the global minimum conformation of a molecule can be a challenging and tedious task, due to a molecule's large set of possible conformations. A main issue with obtaining reliable data in the search for global optimization is possessing a well-defined energy minimum that is kinetically accessible over a relevant temperature range. Of the global optimization methods, the basin hopping routine is a good choice for locating the global minimum and other local minima efficiently.

2.4.1.1 Basin Hopping

Basin hopping (BH) employs a modified Monte Carlo with minimization approach.[72] The initial local minimum geometry is first randomly perturbed, then optimization occurs to determine a new local minimum. This move is then either accepted or rejected, depending on the energy difference between the new local minimum and ground state. If the newly formed geometry has an energy that is less than that of the current lowest energy geometry, the move is accepted.[72] However, if this energy value is larger, the new geometry is only accepted if the energy difference remains within a specified acceptance value, e.g. 0.5, as assessed via a Boltzmann distribution (see equation 2-5):

$$\alpha = e^{-\Delta E/k_B T} \leq 0.5\,, \qquad [\ 2\text{-}5\ ]$$

=where α is the acceptance ratio, and ΔE is the difference in energy between the newly found local minimum and the previously accepted minimum. This process is reiterated until all relevant local minima of the molecule are determined.[72,73] Figure 2-4 depicts the BH process:

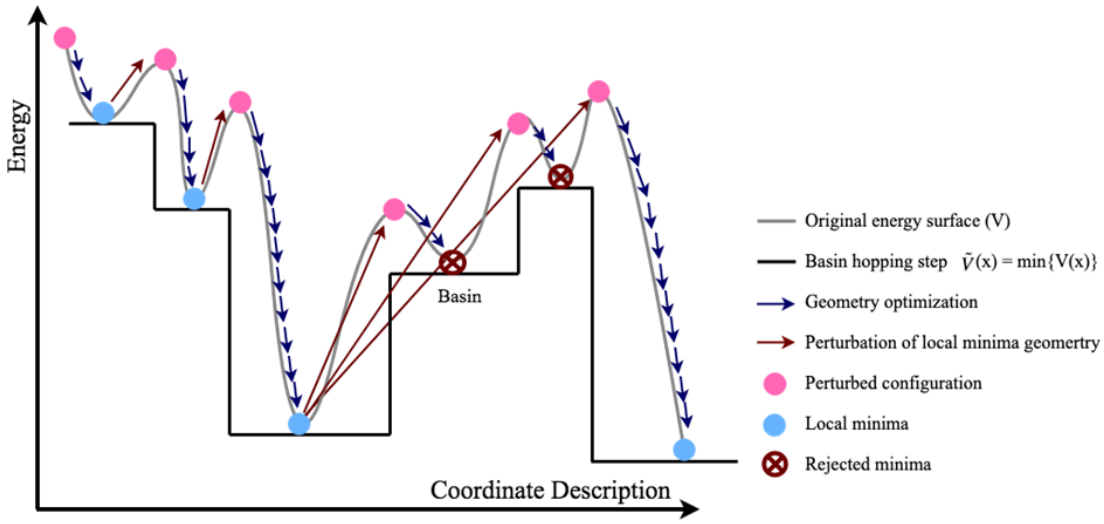

Figure 2-4. The BH process. An initial guess configuration is optimized, reaching a basin, this local minima is then perturbed in geometry. The perturbed configuration is optimized, forming another basin. If the energy of this basin is lower than that of the previous local minima, it is accepted. If not, the BH process is repeated at the last accepted local minima until a new basin is achieved. Image modified from a paper by Hashmi *et al.*[73]

BH explores numerous conformations to reach a global minimum. To limit the computational cost of running such an extensive search, molecular mechanics are employed when optimizing perturbed configurations to reach a local minimum. Molecular mechanics (MM) calculations utilize classical force fields to model atoms.[74] In this work, the Universal Force Field (UFF) approach is used. UFF employs hybridization-dependent atomic bond radii, angles, van der Waals (VDW) parameters, partial nuclear charges, and bond/angle force constants.[75] Unlike other conventional force fields, such as AMBER and CHARMM,[76] which apply only to main group atoms, UFF can be applied to all atoms on the periodic table. The atomic force fields defined by UFF can then be used for calculating the potential energy, V, of a structure, as described in equation 2-6:[75]

$$V_{tot} = V_R + V_\beta + V_\phi + V_w + V_{VDW} + V_{elec} \qquad [\ 2\text{-}6\ ]$$

Here, V_R represents the energy resulting from bond stretching, V_β is the bond angle bend energy, V_ϕ represents the energy from dihedral angle torsion, and V_w represents the inversion energy term. These terms model covalent interactions using the harmonic oscillator model.[75] The UFF also considers nonbonding interactions in the form of van der Waals (VDW) interaction, V_{VDW}, and electrostatic interactions, V_{elec}, between partial charges.[75]

2.4.1.2 Density Functional Theory

The BH process identifies possible local and global minima conformers at a low level of theory (MM). These conformers must therefore be re-evaluated and re-optimized at a higher level for property calculations. For this, DFT is a method that balances computational accuracy and efficiency. Briefly, DFT performs quantum mechanical calculations based on the idea that simply the electron density can be used to determine the parameters of the electronic structure of a system and is sufficient in determining the system's total electronic energy.[77,78] In the Kohn-Sham (KS) DFT framework, the electronic energy of a system is a sum of several components that assume a noninteracting system. These components include: the kinetic energy of noninteracting electrons, and the classical Coulombic interaction potentials.[78] To account for the nonclassical electrostatic interaction

energy and the difference between the kinetic energy of noninteracting and interacting systems, the KS DFT formalism also includes an additional term, the exchange correlation term.[78] Although no exact functional is given to solve the many-body exchange correlation term, DFT relies on functionals that solve this term approximately.[79] In the scope of this thesis, the functional selected is the Becke 3 parameter Lee Yang Parr (B3LYP) functional. The B3LYP functional is a hybrid functional of both Hartree Fock and DFT contributions.[80] B3LYP defines the dynamic electron correlation by using three parameters to mix the exact HF exchange correlation with the Lee Yang and Parr correlation functional. B3LYP has demonstrated high accuracy in defining the exchange correlation term and is employed in for most studies in this thesis.[80]

2.4.2 Thermochemical and Property Calculations

After identifying low-energy structures, vibrational frequencies are calculated to determine local minima on the potential energy surface and to estimate thermochemical corrections. The binding energy, ΔG_{bind}, of a cluster can be determined from the Gibbs energies, G, of ion solvent complexes and of the isolated species (as demonstrated in equation 2-7).

$$\Delta G_{bind} = G_{X\cdot solvent(n-1)} + G_{solvent} - G_{X\cdot solvent(n)}. \qquad [\ 2\text{-}7\ ]$$

One can also calculate the relative stability of a cluster with ion X and n solvent molecules as per equation 2-8:

$$\Delta G_{form} = G_X + nG_{solvent} - G_{cluster}. \qquad [\ 2\text{-}8\ ]$$

This calculation can be utilized when assessing the hypothesized cluster size of the observed species in the DMS. The ΔG_{form} for a cluster of size n can be compared with clusters of other sizes to determine the likelihood that the ion will form such clusters. The values here can then be used to determine the relative population of clusters at various temperatures to infer the distribution of cluster sizes likely observed in the DMS. However, it is important to note that given the dynamic clustering process taking place in the DMS

cell, the calculations above do not account for field effects and kinetics that may affect cluster size at any given moment.

2.4.3 CCS Calculations

Various models exist to calculate the CCS of ion-neutral pairs for comparison with experimentally acquired values. Some methods for CCS calculations include different approximations that simplify the calculation to ease computational costs while others trend towards greater accuracy while increasing computational costs. Of the approximations available, the simplest model includes the projection approximation (PA) model.[49] This model is a relatively inexpensive model that depicts each atom as spherical with having a fixed radius specific to the element.[49] The molecules are projected onto a plane along a certain direction, and the area of this projection is noted. The direction of projection is then altered to obtain more projection areas, and an average is taken to estimate the CCS of the ion. However, the PA model presents several drawbacks that limit its accuracy. For example, long-range interactions taking place between the neutral gas and components past the surface of the ion are neglected.[49] Additionally, as the ion surface roughness is not accounted for. This may affect the contribution of multiple scattering between the ion and neutral pair and lead to further inaccuracies.[49]

A more accurate model, and the method used in this thesis, employs the trajectory method (TM) approximation.[49,50,81] In the trajectory method approximation, momentum transfer integrals averaged over all possible velocities and geometries of the ion-neutral pair are used.[50,81] The TM method improves the accuracy of CCS prediction through modelling of explicit trajectories, temperature and charge state effects, along with the 3D geometry of the molecules.[50,81] In the Mobcal-MPI suite,[81] gas trajectories are computed using the intermolecular potential as defined by the van der Waals, ion-induced dipole, and ion-quadrupole forces. The software offers parameterized VDW interaction potentials using scaling factors, which leads to an improved accuracy in calculated CCS values.[81]

The CCS values cannot be directly related to the DMS behaviour of ions due to the complex processes occuring in the cell. In 2018, a machine learning algorithm was

developed by the Hopkins group to relate the CCS of an ion to that the respective DMS behaviour in a pure N_2 environment.[68] As such, it is currently possible to determine the CCS of an analyte from its DMS behaviour. The calculation of CCS values in other modified environments becomes more complex, however, as the incorporation of ion-neutral interactions between the solvent vapor and the ion along with the ion-N_2 pair is required. While the alignment of the calculated CCS of a probable structure to the experimentally acquired values may aid in the characterization of the conformation of species, a more selective process is required for the identification of similar CCS isomers.

2.5 Ultraviolet Photodissociation

The use of MS for the identification of ions is widespread. Yet, in cases when ion/isomer identification is challenging, the introduction of an orthogonal method for ion characterization is needed. Ultraviolet photodissociation is a technique that can be added to mass spectrometry to enhance ion characterization and identification.

2.5.1 The Mechanisms Behind Ultraviolet Photodissociation

Molecular excitation via absorption of a photon can lead to multiple processes, including dissociation, isomerization, ionization, and relaxation through photon emission.[82] The molecular properties and excited state dynamics dictate the rate, efficiency, and probability of the process taken.[82] Photodissociation is a process of dissociation resulting from absorption of light. Photodissociation spectroscopy is an action spectroscopic method that can be used to measure the spectrum of molecules by monitoring the dissociation efficiency of a molecule into its fragment constituents.[83,84] In photodissociation, photons of resonant energies are absorbed, exciting the molecule into an excited state that is either dissociative or coupled to a dissociative state, and leads to fragmentation into constituent components.[83–85] Photodissociation is generally coupled with mass spectrometric techniques to monitor the relative intensities of parent and fragment ions as the absorbed wavelength is sequentially varied.[83–85] Photodissociation can be executed in a wide range of electromagnetic wavelengths and is typically employed in the infrared (IR), ultraviolet (UV), and visible (VIS) regions.[83–85] In this thesis, the central focus is on ultraviolet

photodissociation (UVPD) due to its high fragmentation efficiency, versatility, and rich sampling of ions.

UVPD involves the irradiation of molecules with high-energy photons, leading to excitation into electronic states higher than the ground state. This method allows access to fragmentation pathways not typically observed/accessed in low-energy dissociation methods, such as collision induced dissociation (CID) and IR multiple photon dissociation (IRMPD).[83,86,87] While CID and IRMPD can result in the excitation of a molecule into its thermodynamic threshold at the ground electronic state, UVPD typically involves excitation to even higher electronic states.[83]

For the case of small molecules, UVPD includes three main dissociative processes: pre-dissociation, direct dissociation, and radiative dissociation.[88] In pre-dissociation, the molecule is excited into a higher electronic bound state, which couples to a dissociative state non-radiatively. This process consists of transitions to discrete energy levels, reflecting the product of the oscillator strength of the initial absorption and the dissociation efficiency of the excited level involved in the transition.[88] Direct dissociation refers to the excitation of the molecule directly to an electronic state that is repulsive with respect to the nuclear coordinate, leading to dissociation. The photodissociation cross section of direct dissociation is continuous as a function of photon energy, due to slow spontaneous emission back into the ground state, and peaks close to the vertical excitation energy described by the Franck-Condon principle.[82] Lastly, in spontaneous radiative dissociation, the molecule is excited into a higher electronic state and relaxes radiatively into either a lower lying dissociative state, or into the ground state at the vibrational continuum. Radiative dissociation efficiency is determined by the competition with spontaneous emission to lower-lying bound states, resulting in discrete cross section peaks.[82] Figure 2-5 represents the three main mechanisms of photodissociation in the case of a diatomic molecule.

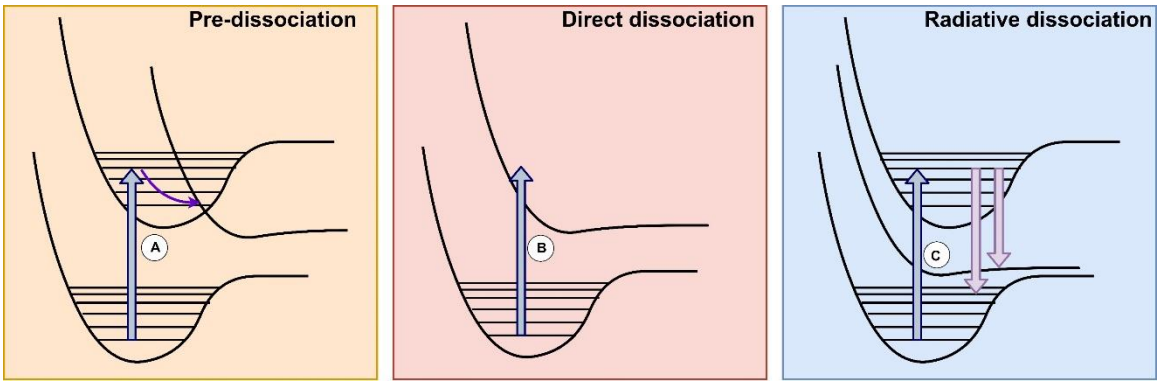

Figure 2-5. The mechanisms of photodissociation (illustrated with potential energy curves of a diatomic molecule). There are three main mechanisms: pre-dissociation (left), direct dissociation (middle), and radiative dissociation (right). Blue arrows represent excitation into an electronic state. Pink arrows represent radiative decay into a lower electronic state. Purple arrows represent nonradiative decay or coupling into another electronic state.

For a large number of atoms, N, the vibrational level density becomes large, forming a quasi-continuum that excited states can couple to non-radiatively in a process called internal conversion.[82] The molecule thus relaxes to a low-lying electronic state at a highly excited vibrational level. With the high density of states exhibited by molecules, the described processes are all likely to be observed. However, photodissociation is heavily dependent on whether a dissociative state and/or threshold is reached to allow fragmentation. Therefore, the kinetic considerations into photodissociation are necessary.[82] Significant factors for the observation of fragmentation include the lifetime of the molecule in the excited state, and the competition between (1) the thermal relaxation back to the ground state, (2) fluorescence, and (3) fragmentation.. Furthermore, the rate of unimolecular dissociation must be considered. Nevertheless, as coupling to excited dissociative states is achievable, fragments that are not seen in CID and IRMPD may be observed.[83] As a result, UVPD has been heavily used due to its selective fragmentation and is acclaimed for its abilities in determining backbone structure of peptides, resulting in fragments that are complementary to IRMPD and CID techniques.[83]

2.5.2 The Implementation of UVPD

UVPD techniques have been implemented in one of two ways: single wavelength UVPD and scanning wavelength UVPD spectroscopy. In single wavelength UVPD, light

is set to a specific wavelength to irradiate trapped ions and induce fragmentation.[89–91] This is beneficial when requiring selective fragmentation to identify structural moieties/components in a molecule of interest. Due to some instrument limitations in identifying isomers, the field of metabolomics has utilized various laser sources for selective fragmentations. One popular source includes the Nd:YAG laser for its use in generating its third and fourth harmonic wavelengths, 355 nm and 266 nm, respectively. As peptides readily absorb at 266 nm, the irradiation of peptides at this wavelength results in richer fragmentation of the peptide into its amino acid constituents.[87,88,90] Other popular laser sources include the excimer laser, ArF which produces the heavily employed 193 nm wavelength for the fragmentation of double bonds in lipids for characterization.[89]

In other UVPD spectroscopy methods, the wavelength is scanned to probe the vibronic spectrum of molecules through measurement of the fragmentation efficiency as a function of wavelength.[92] With the vibronic spectrum of a molecule sampled, one can determine the geometric and electronic structures of the molecule, providing detailed characterization and identification of molecules of interest.[82] UVPD spectroscopy has been implemented in several studies for the investigation of isomeric species.[89,92,93]

2.5.3 Experimental Apparatus

In 2020, Coughlan et al. modified a DMS-MS instrument in the Hopkins Lab to couple it with UVPD experiments for the thorough analysis of ions in the gas phase.[94] Figure 2-6 depicts a schematic diagram of the DMS-MS setup coupled to UVPD.

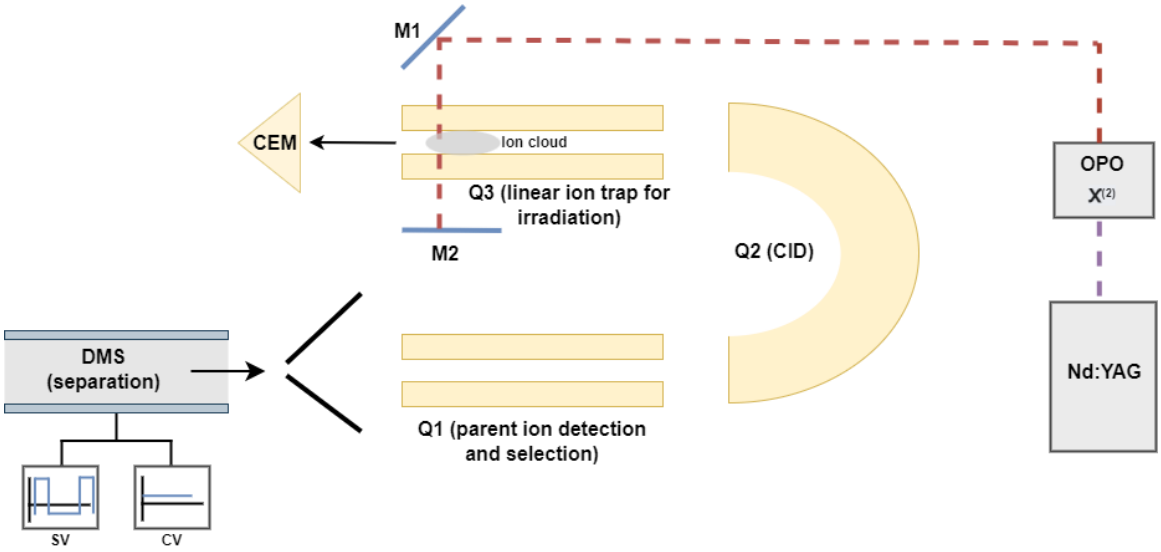

Figure 2-6. Experimental setup for DMS-MS coupled with UVPD investigations. Ions are separated in the DMS and subsequently mass selected in Q1. CID is minimized in Q2 to yield the highest intensity of the parent ion which is then trapped at the linear ion trap at Q3. A Nd:YAG-pumped OPO is then used to direct a laser beam towards the trapped ion cloud for irradiation and fragmentation, as detected by the detector.

A window into the triple quadrupole mass spectrometer was added to the back of the instrument to allow irradiation from a Nd:YAG-pumped optical parametric oscillator (OPO) laser to pass through the third quadrupole, Q3. Mirrors are added to allow for the light to pass orthogonal to the direction of ion flow in Q3 at the position of the ion cloud trapped by the linear ion trap (LIT). Employing the OPO provides the significant advantage of expanding the probing wavelength ranges from the UV region all the way to the IR region. Thus, the OPO setup can be used for spanning the entire UV and VIS range to gain an action spectrum of ions of interest.

In the experimental setup, the DMS is set to an ion filtration technique, in which an SV/CV pair is selected to isolate an isomer of the desired analytes. The triple quadrupole is set to the enhanced multicharged scan, which has been modified to allow for optimal trapping of ions and irradiation. In this scan mode, the first quadruple, Q1, is set as a filter to allow only the desired *m/z* value through. The second quadrupole is set as the collision cell and cannot be modified into an ion-guide. To limit dissociation by means of CID, the collision cell parameters are set to the lowest settings. In the enhanced scan mode, the LIT is activated to allow trapping of the desired ions for irradiation. Ions are trapped in the LIT

for 500 ms and irradiated for a length of 30 s with wavelengths ranging from 200 nm to 400 nm. Spectra are generated by determining the fragmentation efficiency of ions, $I(\lambda)$, as a function of wavelength, as described by equation 2-9:

$$I(\lambda) = \frac{\lambda}{E_p(\lambda)} - log\left[\frac{\sum I_{parent,\lambda}}{\sum I_{fragment,\lambda} + \sum I_{parent,\lambda}}\right], \qquad [\ 2\text{-}9\ ]$$

and scaled to the pulse energy at each wavelength, $E_p(\lambda)$, as measured by a power meter at the optical pathway. The setup was recently further improved by realigning the linear accelerator in the ion trap to navigate and trap the ions closer to the laser beam. The modification led to a significant improvement of the cross section of the beam path with the trapped ions, resulting in more observable fragmentation efficiencies.

2.5.4 Drawbacks and other Considerations

Given the UVPD mechanisms described previously, it is important to note a few things about the accuracy of the experimental setup. Action spectroscopy is dependent on the fragmentation efficiency of the ion, thus UV excitation that is not coupled to a dissociative state will not be accounted for in the generated spectrum. As such, one can expect a variation in spectral intensities when comparing action spectra of ions with their respective absorption spectra. Furthermore, the detection of fragmentation in the current UVPD setup requires the generation of fragment ions, such that they may be detected and identified by their mass-to-charge ratio. Any neutral fragments formed from UVPD do not contribute to the action spectrum of the molecule. Finally, it is important to consider the possibility of secondary fragmentation processes taking place, in which a fragment ion formed from photodissociation is subsequently irradiated leading to secondary fragment formation. The changes in intensities from subsequent photodissociation affects the generated spectra, leading to false description of the electronic spectrum of the molecule. Depletion of the fragment ion from irradiation due to formation of neutral fragments could lead to low reporting of the fragmentation efficiency of the ion.

In the case of negative ions, it is important to also consider their electron detachment thresholds. In the case when the electron detachment energy threshold is lower than the

electronic excitation threshold of an anion, irradiation of the anion may instead lead to the detachment of an electron, neutralizing the parent ion and thus depleting the anion intensity.[95] In this case, a photodissociation spectrum cannot be acquired and a photodepletion spectrum is instead required.[95]

With the considerations described above, the immediate identification and classification of isomers may not be readily attainable without the comparison to simulated spectra. As such, computational calculations are performed to simulate the vibronic spectrum of the analyte ions and compare them to what is observed experimentally.

2.6 Excited State Calculations

The identification and characterization of the electronic structure of isomers investigated in the DMS-MS and UVPD setup is complemented with simulations of the excited state dynamics of the optimized structures. Therefore, an in-depth understanding of the factors that affect the electronic structure of each isomer is obtained.

2.6.1 Excited State Theory

For a many-body system, such as atoms/molecules with more than one electron, it becomes exhaustive to computationally simulate the properties of systems. Approximations must be employed for computational efficiency while still maintaining a relatively high level of accuracy.

Given that electronic transitions occur at a much faster rate than nuclear transitions, approximations can be made to decouple electronic and nuclear components. In the case of excited state dynamics, the intensity of a transition between two states is dictated by the transition dipole integral between the two states, given by equation 2-10:[96]

$$\langle \mu_{i,f} \rangle = \frac{\langle \psi_i | \hat{\mu} | \psi_f \rangle}{\sqrt{\langle \psi_i | \psi_i \rangle \langle \psi_f | \psi_f \rangle}} \qquad [\ 2\text{-}10\ ]$$

where Ψ_i and Ψ_f are the molecular wavefunctions for the initial and final states, respectively. As electronic transitions occur at a significantly faster timescale than those of

nuclear transitions, the calculation of the transition dipole can be simplified by applying the Born-Oppenheimer (BO) approximation. The electronic and nuclear wavefunctions can thus be treated separately, such that an electronic wavefunction at any instantaneous nuclear geometry can be determined.[96] Applying this approximation results in the following (equation 2-11):

$$\langle \mu_{i,f} \rangle \approx \frac{\langle \chi_i | \langle \phi_i | \hat{\mu} | \phi_f \rangle | \chi_f \rangle}{\delta_{i,f} \sqrt{\langle \chi_i | \chi_i \rangle \langle \chi_f | \chi_f \rangle}} \qquad [\ 2\text{-}11\ ]$$

where ϕ represents the electronic wavefunction, χ represents the nuclear wavefunction, and the electronic wavefunction, $\langle \phi_i | \phi_f \rangle = \delta_{i,f}$, is orthonormal.

One issue that arises from the excitation of a molecule from one electronic state to another is the subsequent change in nuclear coordinates and normal modes. One must decouple the internal (vibrational) and external (rotational and translational) motions for simplification. For semi-rigid molecules—molecules with a PES possessing a well-defined minimum—this is done by assuming the Eckart-Sayvetz conditions are met, which allow for the separation between the external and internal motions.[96] Once external motions are factored out, the transition dipole integral between two states can be defined as shown in equation 2-12:[96]

$$\langle \mu_{i,f} \rangle \approx \frac{\langle \chi_i^v | \langle \phi_i^v | \hat{\mu} | \phi_f^v \rangle | \chi_f^v \rangle}{\delta_{i,f} \sqrt{\langle \chi_i^v | \chi_i^v \rangle \langle \chi_f^v | \chi_f^v \rangle}} \qquad [\ 2\text{-}12\ ]$$

When looking at vibrational spectra, the harmonic oscillator (HO) approximation is used. In the HO approximation, the Morse potential of a molecule is approximated to resemble a HO centered around the equilibrium geometry, in which the frequencies are defined by the molecule's vibrational normal modes. This approximation is sufficient in describing the potential energy well about low-lying vibrational states[97] The vibrational HO Hamiltonian can be given by equation 2-13:

$$\hat{H} = \hat{V} + \hat{T} = \sum_{i=1}^{N} \frac{1}{2} \omega_i (\hat{q}_i^2 + \hat{p}_i^2) \qquad [\ 2\text{-}13\ ]$$

where N represents the total number of normal modes, ω represents the HO frequency, and $\hat{q}$ and $\hat{p}$ represent normal coordinates and conjugate momenta, respectively. When accounting for dissociation processes, which typically occur around the higher vibrational levels, corrections for anharmonic behaviour is required. Anharmonicity, or the deviation from a HO potential, adds to the accuracy of the spectra close to the dissociation threshold.

While pure vibrational spectra are rather straightforward, electronic and vibronic spectra add another level of complexity, as the normal coordinates differ between the initial and final electronic states. Electronic spectra span over a large energy range, and thus there is a need to look at a large set of transitions between vibrational states. Furthermore, transitions to higher vibrational states in the electronic excited state, $v' > 0$, tend to have larger oscillator strengths as compared with those close to the excited state minimum, $v' = 0$. Yet, calculating integrals for the transitions requires a clear definition of common basis sets between the initial and final electronic states. The Duschinsky effect describes the phenomenon in which the normal modes and frequencies differ between electronic states.[96] A solution to this problem is to express one set of mass-weighted normal modes with respect to the other. This is described by the following equation:

$$\vec{Q}_i = \overleftrightarrow{J}\,\vec{Q}_F + \vec{K} \qquad [\ 2\text{-}14\ ]$$

in which Q represents the normal coordinates of electronic state, i or f, $\overleftrightarrow{J}$ is the Duschinsky matrix, and $\vec{K}$ is the displacement vector that accounts for the shift between the equilibrium geometries.[96] The definition of $\overleftrightarrow{J}$ and $\vec{K}$ is dependent on the type of calculation applied when determining the transition overlap integrals.

Calculations of the electronic transition moment depend on the nuclear coordinates. Tackling this dependence can be done in two main ways: the Franck-Condon approximation or the Herzberg-Teller (HT) approximation. The Franck-Condon (FC)

approximation assumes that electronic transition probabilities depend on the vibrational wavefunction overlap integral (i.e., more likely if the ground and excited state have similar vibrational wavefunctions). The Herzberg Teller approximation (also referred to as the FCHT) was introduced to the FC approximation to account for symmetry-forbidden transitions that are observed experimentally. These transitions are rationalized by intensity borrowing from vibrational transitions. The FC approximation assumes no nuclear dependence on the electronic transition dipole moment. However, this is restrictive and is not observed to be true.[98] Nuclei tend to shift slightly during the transitions, causing a change in the electronic dipole moment. As a result of the slight shift, a Taylor series expansion about the equilibrium is used to introduce the HT term. The HT term relates the electronic dipole moment to the coordinates of the normal modes.[98] A vibrational distortion of the molecule at the excited state can result in a transition that is symmetry allowed or what has been referred to as intensity borrowing. In general, when dealing with symmetry forbidden transitions, the FC term goes to zero while a non-zero HT term can result in a nonzero transition dipole.[98] However, cases in which the HT term must be accounted for are not relevant to the scope of this thesis. As such, excited state transitions are calculated using harmonic Franck Condon factors.

2.6.2 Harmonic Franck Condon Factors

Harmonic Franck Condon factors (FCF) are the overlap integrals between the wavefunctions of two vibronic states. These calculations are dependent on both the Born Oppenheimer and HO approximation.[99] As a result, FC calculations determine electronic transition probabilities at instantaneous initial nuclear geometry, generally at the equilibrium geometry. Calculation of the FCF for each transition requires a determination of the Hessian (or the matrix of second derivatives with respect to the molecular coordinates of the potential energy surface). The Hessian represents the curvature of the PES, which subsequently allows for the determination of vibrational frequencies for the harmonic oscillator, along with the corresponding normal mode coordinates. Figure 2-7 depicts the general transitions being considered in FCF calculations.

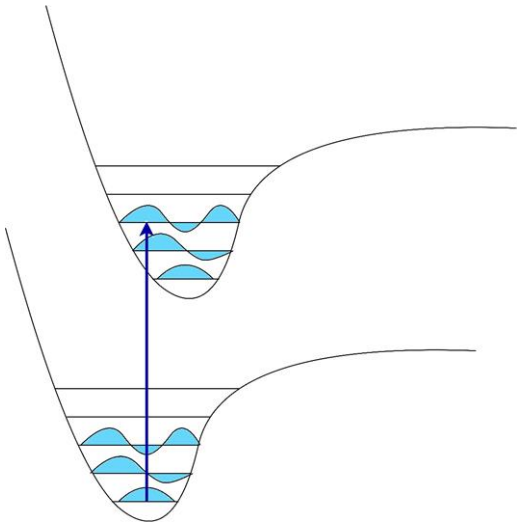

Figure 2-7. Franck Condon calculations determine the overlap of the wavefunctions of the initial and final vibronic states.

In this work, FCF are used to calculate the transition dipole, or the oscillator strength, for transitions from the ground vibronic state to an excited vibronic state. It is important to note that the total transition probability, P, is dependent on both the electronic, M_{el}, and vibronic, M_{vib}, transition probabilities as highlighted in equation 2-15:[100]

$$P = M_{el}M_{vib}. \qquad [\ 2\text{-}15\ ]$$

The square of the total transition probability results in the intensity of each transition,

$$I = |P|^2 \qquad [\ 2\text{-}16\ ]$$

where the vibrational dipole moment is expressed as:

$$M_{vib} = \langle \psi'_{vib}|\hat{\mu}_{el}(Q)|\psi''_{vib}\rangle. \qquad [\ 2\text{-}17\ ]$$

Calculating the probability of each transition is determined through the overlap integral over all nuclear coordinates,[100]

$$\int [\psi'_{vib}(Q')] * \psi_{vib}"(Q")dQ' = \langle v'_1 \dots v'_{Nvib}|v_1"\dots v''_{Nvib}\rangle\,. \qquad [\ 2\text{-}18\ ]$$

The relationship between lower state vibrational quanta, v_i'', and upper state quanta, v', for a non-zero FCF is nontrivial. We can qualitatively view transitions between vibronic states as vertical and represent the vibrational functions using HO.[100] In this approximation, excitation from the lower vibrational state, $v'' = 0$, is favored for higher quanta of the excited state, v', as the PES of the upper states is shifted relative to the ground electronic state. More general treatments of FCF yield increased accuracy in results but still employ assumptions to expedite calculations and/or make computation feasible. The assumptions used for calculating the PES of each state determines the type of FC calculation being run.

2.6.3 Computational Setup

For this thesis, vibronic absorption spectra of molecules are simulated using the ORCA suite.[101,102] For most molecules, the simplest form of the Franck-Condon approximation (the Vertical Gradient approach) is used in an effort to reduce computational time but maintain a certain level of accuracy. Since electronic transitions occur at a much faster timescale, it is expected that the most intense transitions will be those of the vertical excitations.[103,104] The VG FC approach builds upon the BO approximation by assuming little to no change in the nuclear coordinates as the molecule undergoes an electronic excitation.[103,104] As a result, VG FC simplifies the computational workflow by assuming the Hessian, normal modes, and frequencies of the initial ground state for the excited state. Instead, the potential energy at isolated points along the nuclear coordinates of the excited state are determined.[103,104] The gradient along these values is then calculated to determine the shift in equilibrium geometry at the specified excited state.[103,104]

The simplifications in the VGFC model make it a time-feasible approach for the calculation of molecular spectra and is employed for the calculation for large molecules at a broad energy range.[105] Its accuracy has also been proven, as vertical excitations are the most probable transitions when the HO approximations are valid. However, this approximation breaks down when there is a large shift in the normal modes between the

two states – or when the HO breaks down.[96] Figure 2-8 shows the mechanism of calculating FCF using the VG approximation.

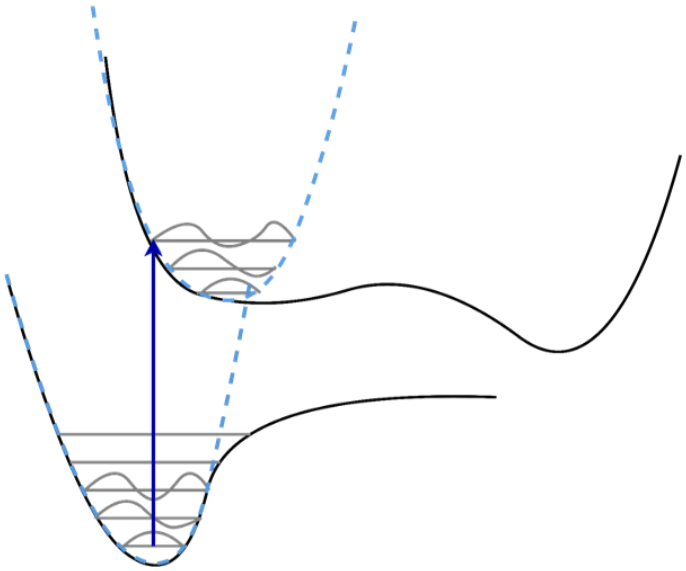

Figure 2-8. VG FC assumes the Hessian, normal modes, and frequencies of the ground state and calculates the gradient to shift the excited state about the equilibrium geometry. Transitions are calculated vertically from the minimum of the ground state.

In the case of excited state dynamics, the Coulomb attenuated method B3LYP (CAM-B3LYP) functional is employed. The modified functional addresses issues with accuracy of the exchange potential for long-range systems.[80] In CAM-B3LYP, the exchange interaction is partitioned into long-and short-range components, improving the performance of the functional when dealing with excitations using TD-DFT, especially in the case of Rydberg and charge transfer excitation energy calculations.[80] In this correction, the exchange potential is split into two terms, to allow for mixing of both HF exchange for short-range systems and DFT exchange for long-range systems.[80] Several studies have demonstrated the high accuracy of CAM-B3LYP in determining the excited state dynamics of compounds, making it a suitable functional for the scope of this thesis.[106,107]

Chapter 3: The Separation of Cannabinoid Isomers using DMS

DMS can separate isomers based on differences in their differential mobilities and clustering behaviour. In this chapter, we explore the use of DMS in the separation of five cannabinoid isomers. The properties of the modified DMS environment were demonstrated to affect the survival of ESI-formed ion-solvent adducts, complicating the separation of isomers by the presence of multiple solvent peaks. It was found that a protic modifier solvent was required to displace the ESI-formed adducts and improve the separation of all cannabinoid isomers. In this case, the use of isopropyl alcohol as the modifier in the DMS carrier gas allowed for separation based on their clustering behaviour.

The work described in this chapter was published in 2022 following peer-review in Analyst and can be found in *Analyst*, **2022**, 147, 2198-2206.

3.1 Introduction

Reliable testing methods for the detection of cannabinoid molecules in extracts and sample mixtures are crucial for the regulation and quality assurance of cannabis products. Demand for rapid testing, especially for psychoactive cannabinoids, has increased in recent years as restrictions on cannabis products are loosened globally.[108] In particular, Δ^9-tetrahydrocannabinol (Δ^9-THC) and its isomers have garnered attention, as these are the active ingredients in cannabis products that present psychoactive or pharmacological activity owing to their binding affinity with the two cannabinoid receptors found in humans.[109] Structural differences between the cannabinoid isomers influence their

biological activities. For instance, cannabidiol (CBD) has shown effectiveness as a treatment for Parkinsons' symptoms, whereas other cannabinoids exhibit limited activity in this regard.[110,111]

A variety of cannabis extracts are also produced for recreational use and thus require fast and accurate quantitation for quality control purposes. Typically, quantitation can be achieved by tandem mass spectrometry since many cannabinoid derivatives are distinguishable by their mass and unique fragmentation pathways.[112] However, several of the most important cannabinoid molecules are present in isomeric forms that produce the same multiple reaction monitoring (MRM) transitions. Consequently, an additional, orthogonal separation step, most commonly liquid chromatography (LC),[113] is required prior to their characterization by mass spectrometry. The five most common cannabinoid molecules found in cannabis products are shown in Figure 3-1. Δ^9-THC, CBD, and cannabichromene (CBC) are three isomers that exhibit identical collision induced dissociation products.

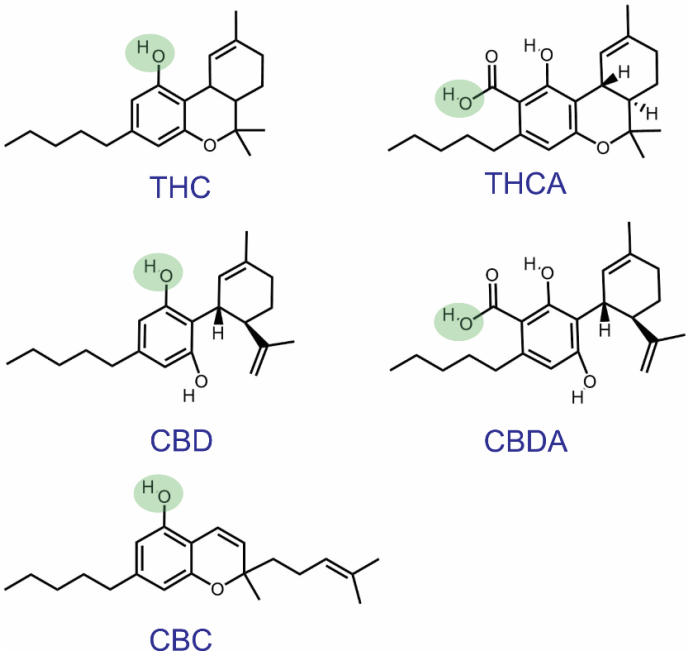

Figure 3-1. The Δ^9-THC, CBD, and CBC isomers exhibit m/z 313.2 for the deprotonated molecules. (−)-THCA and CBDA isomers exhibit m/z 357.2 for the deprotonated ions. Deprotonation sites (based on calculation; *vide infra*) are highlighted for each molecule in green.

Similarly, the cannabidiolic acid (CBDA) and (−)-tetrahyrdocannabinolic acid ((−)-THCA) isomer pair also exhibits identical fragmentation products and are thus challenging to distinguish by mass spectrometry.[112] Although the carboxylated isomers are typically the most abundant in marijuana flower, the decarboxylated counterparts are responsible for the psychoactive and pharmaceutical effects associated with cannabis products.[113–115]

To overcome the challenges associated with quantifying cannabinoid isomers, liquid chromatography (LC) is commonly employed to separate isomers prior to the identification and quantification by mass spectrometry.[21,108,116–119] Yet, this approach can be relatively time-inefficient, requiring rigorous sample pre-processing and >15 min per LC-MS analysis.[120] An alternative method for rapid testing of cannabinoid molecules is the use of colorimetric tests that employ fast blue BB salt.[121] However, this method lacks specificity, as it typically leads to false positives for samples that contain other phenolic compounds.[122]

Ion mobility spectrometry (IMS) is a technique that has been used to great effect for analysis of complex mixtures, and it can be used to separate isomeric compounds in milliseconds based on differences in their collision cross sections (CCSs).[123,124] Several variants of IMS exist, in which the electric field component, device geometry, and gas-phase properties are altered to address different target outcomes better (e.g., analyte separation, CCS measurement).[123,124] With regard to the application of IMS technology in cannabinoid analysis, Hädener et al. and Tose et al. published studies outlining methods for separating cannabinoid isomers using drift tube IMS (DTIMS) and ultrahigh pressure liquid chromatography coupled with travelling wave IMS (UPLC-TWIMS), respectively.[120,125] Hädener's DTIMS-MS work demonstrated the separation of the Δ^9-THC/CBD and (−)-THCA/CBDA isomer pairs in a "dilute-and-shoot" extraction based on differences in CCSs for the protonated and deprotonated analytes.[120] In Tose's study UPLC to isolate Δ^9-THC, CBD, and (−)-THCA based on their characteristic retention times, and TWIMS was introduced to resolve the cis and trans isomers, albeit only partially.[56,125]

Here, we investigate the use of differential mobility spectrometry (DMS) coupled with MS as a rapid, direct-infusion approach for separating and quantifying of cannabinoid isomers. The manipulation of an ion's DMS behaviour by introducing a low percentage of solvent vapour to the carrier gas is now well documented and has been used to separate many isomeric and isobaric species.[25,63,65,126] The enhanced separation power afforded by solvent-modification of the collision environment stems from the subtle differences in ion-solvent interaction strengths for isomeric species; the thousands of dynamic clustering duty cycles over the course of DMS transit magnify these differences and ultimately results in spatial separation.[58] Herein, we identify DMS conditions to separate the cannabinoid isomers Δ^9-THC, CBD, and CBC, effectively, as well as the carboxylated analogues, (−)-THCA and CBDA. Once optimal conditions are identified for isomer separation, we demonstrate the use of DMS to quantify the amount of these cannabinoid isomers in a marijuana flower sample.

3.2 Methods

3.2.1 Experimental Methods

The DMS-MS apparatus used in this study is described in detail elsewhere.[24,59,63] All HPLC-grade solvents were purchased from Sigma Aldrich, USA. Ultra-pure grade ammonium acetate was purchased from Amresco, USA. Analytical standards of Δ^9-THC, CBD, CBC, (−)-THCA-A, and CBDA (Cerilliant, Canada) were dissolved in 1:1 HPLC-grade acetonitrile:methanol with 5 mM ammonium acetate buffer and were diluted to 100 ng/mL. The compounds were electrosprayed (TurboV, SCIEX, Canada) into the DMS-MS device (SelexION, SCIEX, Canada) and analyzed in negative ion mode with a triple-quadrupole mass spectrometer (QTRAP 5500, SCIEX, Canada). The carrier gas, N_2, was seeded with 1.5% (*v/v*) of HPLC-grade acetone (ACE), acetonitrile (MeCN), or isopropyl alcohol (IPA) to create different modifier environments for separation and characterization purposes, as described previously, with greater detail provided elsewhere.[58–60,63] Enhanced product ion (EPI) scans in negative ion mode were used to isolate the $[M-H]^-$ ion signals at *m/z* 313.2 (for Δ^9-THC and its isomers) and 357.2 (for the carboxylated species). A

detailed description of the experimental setup and instrument parameters are provided in Appendix A Table A- 1. The Analyst 1.7 software was used to operate the SCIEX DMS-MS setup. The introduction of resolving gas (N_2) led to an improvement in the resolution of the separation methods employed. The resolving gas, referred to as DR in the controlling software, was modified to fine tune the flow rate of gas introduced in the throttle region of the DMS. Increasing the flow rate of the resolving gas increased the residence time of ions in the DMS, subsequently improving the separation at the expense of ion signal. Details on the resolving gas parameters used are found in Appendix A Table A- 2.

3.2.1 Marijuana Flower Sample Preparation

A marijuana flower sample (Blueberry Haze; Ontario Cannabis Store) was obtained to test the analytical performance of the method developed for the five cannabinoid isomers. A sample of mass 0.829 g was coarsely ground and extracted in 50 mL of HPLC-grade IPA. The sample was centrifuged and 100 µL of the supernatant was diluted in 900 µL of 1:1 MeOH:MeCN with 5 mM ammonium acetate to produce a 1:10 dilution. Subsequent serial dilutions were performed to produce a solution of 400 ng/mL concentration (ng of flower / mL of solvent) in 1:1 MeOH:MeCN with 5 mM ammonium acetate when back calculated to the original flower mass. No additional preparative methods were employed. Two other marijuana flower samples from other brands (Pure Sun and Skunk Haze; Buddies Cannabis Store) were also tested using the same extraction method and dilution to a solution of 200 ng/mL concentration).

3.2.3 Computational Methods

To support experimental findings and rationalize the observed DMS behaviour, computational investigations of the cannabinoid ions and potential ion-solvent clusters that could be formed in the DMS device were conducted. A custom-written basin hopping (BH) algorithm was employed to determine candidate structures for bare $[M-H]^-$ and analyte-solvent clusters by mapping their respective potential energy surface (PES) to identify low-lying energy conformers.[72,127,128] Dihedral angles were rotated in Φ = 10° increments, while oligomer groups were translated (in the x, y, z directions) by θ = 0.5 Å and rotated by

η = 15°, respectively. The BH search ran for 10,000 iterations (sampling ~20,000 geometric structures with a 0.5 acceptance ratio for each molecule and cluster) to identify candidate structures for DFT optimization. The Gaussian 16 suite[129] was then employed to model gas-phase molecules and clusters at the DFT B3LYP/6-311G ++ (d,p) level of theory including D3 dispersion corrections.[80,130] Thermochemical calculations and corrections were acquired for each structure of interest.

3.3 Results and Discussion

3.3.1 Determining Optimal Separation Conditions

The DMS behaviour of deprotonated Δ^9-THC under four gas-phase environment conditions is shown in Figure 3-2A (see Appendix A Figure A-4 to Figure A- 6 for the studies conducted on the other analogues). For the N_2, ACE-modified, and MeCN-modified environments, multiple ionogram peaks were observed at high SV values.

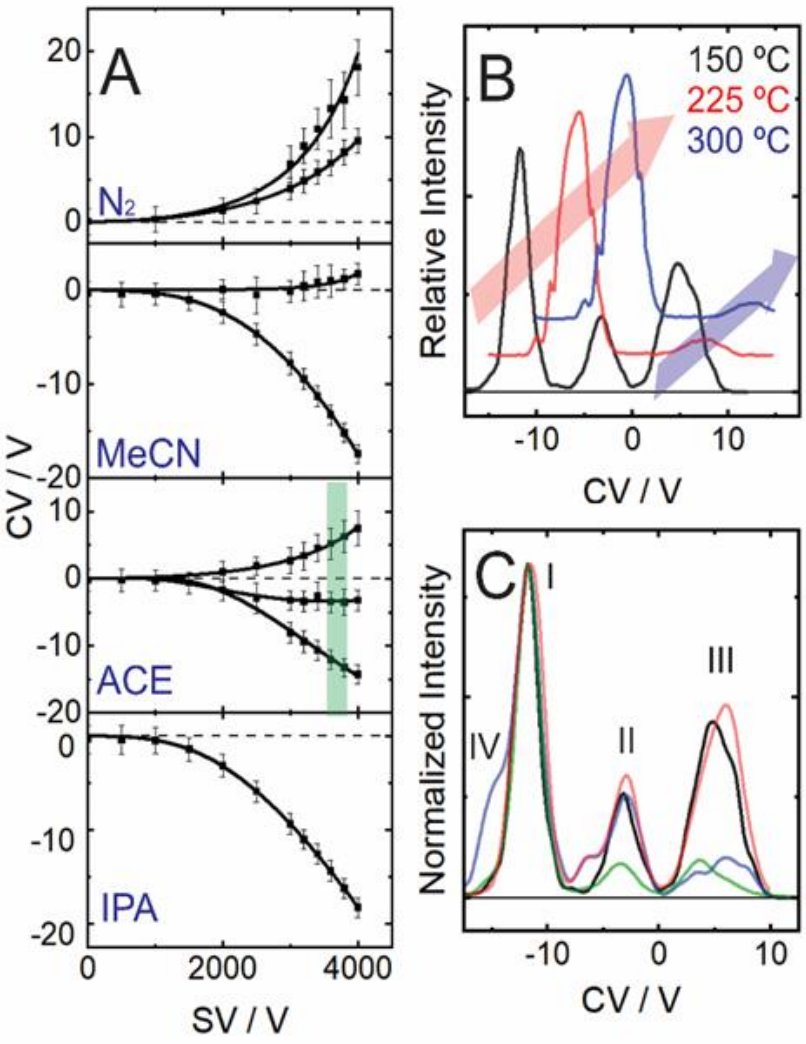

Figure 3-2. (A) The dispersion plots recorded for deprotonated Δ^9-THC standard in N_2 and in N_2 environments modified with 1.5% (*v/v*) MeCN, ACE, and IPA at T = 150 °C. (B) The ionogram of deprotonated Δ^9-THC in N2 seeded with 1.5 % (v/v) ACE at SV = 3600 V for T 150, 225, and 300 °C. (C) The ionogram of deprotonated Δ^9-THC (T = 150 °C, SV = 3600 V, 1.5% ACE) as observed for four ESI solvent systems: (black) 5mM ammonium acetate in MeOH:MeCN, (green) 7 mM NH4OH in MeOH:MeCN, (red) 5mM ammonium acetate in MeOH, and (blue) 5mM ammonium acetate in MeCN.

The observation of multiple peaks typically arises when multiple isomeric forms are present or when a larger ion-solvent cluster that contains the analyte fragments post-DMS and prior to mass selection.[59,65,67] To identify the species giving rise to the observed ionogram features, peak dependence on temperature and ESI solvent composition was studied. For example, in the case of deprotonated Δ^9-THC in the ACE-modified

environment at SV = 3600 V, the ionogram peak at CV = −11 V was relatively unaffected by temperature whereas the peaks at CV = −4 V and CV = 5 V depleted with increasing temperature (see Figure 3-2B). This depletion behaviour is typically associated with dissociation of weakly-bound clusters at higher bath gas temperatures.[131] To further test whether this was the case in this experiment, the gas temperature was set to the lowest value, DP was reduced to 0 V, and precursor ion scans were conducted (see Figure A- 7 for the case of THC and Figure A- 8 for those of its isomers). Precursor ion scans for the peak at CV = −16 V showed only the $[M-H]^-$ ion in the mass spectrum. Given the DMS behaviour of the ion population, we associate the ion population at CV = −16 V with strongly bound ion-solvent clusters that fragment during transit from the atmospheric pressure conditions of the DMS to the vacuum conditions in MS.[67] Precursor ion scans of the features at CV = −11 V and CV = −4 V showed a mass peak corresponding to $[M-H+116]^-$ and $[M-H+60]^-$, respectively, which are attributed to clustering with two acetone molecules for the peak at CV=−11 V and a Δ^9-THC anion adducted with acetic acid (AA) at CV = −4 V. On the other hand, precursor ion scans of the CV = +5 V population showed a mass peak at $[M-H+314]^-$. We attribute this to a proton-bound dimer of THC transiting the DMS with hard-sphere behaviour.

We corroborated the identity of the AA-containing cluster by substituting NH_4OH for AA, which substantially reduced the peak intensity in the ESI solution (see Figure 3-2C). ESI solvent composition studies showed ESI solvent dependence of the THC dimer observed at CV = +5 V. The fact that this ionogram peak is observed when employing the MeOH:MeCN + ammonium acetate and MeOH with ammonium acetate ESI solutions, but not when spraying from the MeCN with ammonium acetate solution, suggests that dimer formation in the ESI process may be affected by the ESI solvent composition and may be associated with a weakly-bound MeOH cluster. We also note that the CV = +5 V peak is somewhat wider than the other peaks suggesting that multiple species may contribute to this ionogram feature. Regardless, the presence of multiple confounding peaks when only a single isomeric species is expected for Δ^9-THC is not ideal when the goal is to separate Δ^9-THC from the CBD and CBC isomers.

Under IPA-modified conditions, Δ^9-THC, CBD, and CBC each exhibit two ionogram peaks, one of which was substantially more intense than the other. The separation of the two ionogram peaks for a given analyte increased with increasing SV, and the intensity of the minor feature diminished to the point of absence (see Appendix A Figure A- 11). Temperature studies and IPA-modifier concentration studies (see Appendix A Figure A-12 and A-13) indicate that the smaller feature is associated with large ion-solvent clusters. Note that only a single ionogram peak is observed for THCA and CBDA across all SV values. To simplify the ionograms for analytical purposes, a single ionogram peak can be generated by operating at high SV values for all five cannabinoid molecules, with optimal separation occurring at T = 150 °C for THC/CBD/CBC and T = 225 °C for THCA/CBDA.

To rationalize the observed clustering behaviour, computational studies of the possible ion-solvent interactions were conducted. The calculated binding energies of the five deprotonated cannabinoid molecules with the various solvent molecules studied are provided in Appendix A Table A- 3. We find that protic solvents bind more strongly with the analytes than do aprotic solvents owing to the formation of relatively strong hydrogen bonds. We also see that in cases where ESI solvent adducts are more strongly bound than ion-modifier clusters, the ESI solvent adducts survive transit of the DMS cell. For example, when MeCN is employed as an ESI solvent and ACE is employed as a modifier, MeCN adducts are observed. However, when IPA is used as a modifier, IPA displaces MeCN from the ion-solvent clusters. The phenomenon of preferential solvation in modified DMS environments has been described in detail previously.[131]

3.3.2 Isomer Separation

Dispersion plots and ionograms at optimal separation conditions are plotted for the five cannabinoid species in Figure 3-3. Figure 3-3A shows the Type A dispersion plots for the Δ^9-THC, CBD, and CBC isomers at T = 150 °C and the ionograms recorded for the individual chemical standards at SV = 4250 V with a low resolving gas (aka throttle gas) setting of DR = 20 are overlaid in Figure 3-3B. Separation can be further improved by increasing the resolving gas flow, but at the expense of ion signal.[24] Figure 3-3C plots the

ionogram recorded for a 1:1:1 mixture of Δ^9-THC:CBD:CBC standards at SV = 4250 V. Under these conditions, near base-line separation of the ionogram peaks is possible. Differences in peak intensity are due to differences in ionization efficiency between the three analytes. We recommend this SV/DR pair setting for analysis of Δ^9-THC/CBD/CBC since ion transmission diminishes at higher residence times and electrical breakdown may occur at higher SV values.

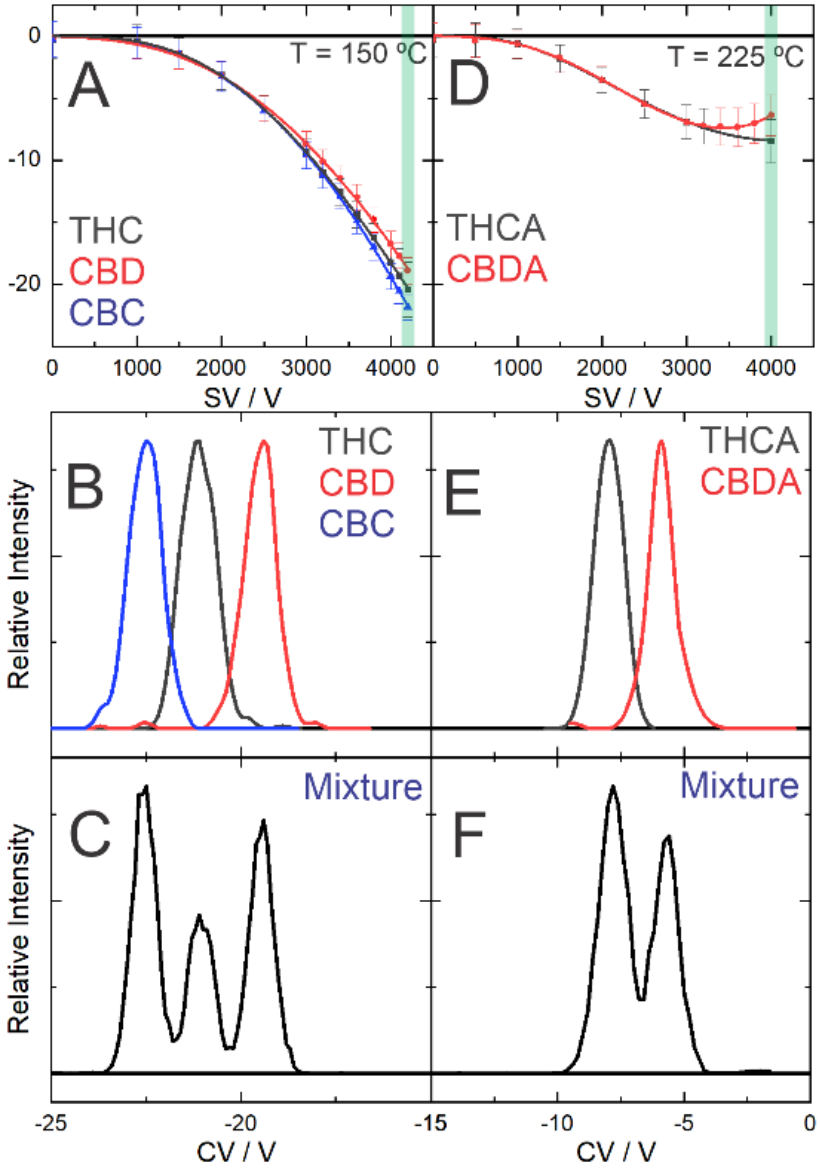

Figure 3-3. Dispersion plots of (A) decarboxylated and (D) carboxylated cannabinoid isomers at optimal IPA modifier conditions. Ionograms of the (B) decarboxylated and (E) carboxylated standards taken at SV = 4250

V with a DR = 20 and 10, respectively. Ionograms of a (C) 1:1:1 mixture of Δ^9-THC, CBD, and CBC and a (F) 1:1 mixture of (−)-THCA and CBDA.

In applying similar methodology to (−)-THCA and CBDA, optimal separation conditions were identified at a temperature of T = 225 °C with a resolving gas setting of DR = 10 (see Figure 3-3D and Figure 3-3E). Under these conditions, both ions exhibit Type B clustering behaviour and are resolvable at SV > 3750 V. The more negative CV deflection of (−)-THCA, compared to CBDA, indicates that THCA interacts more strongly with the IPA modifier, which correlates with the computed binding energies of the ion-solvent clusters.[63,94] A DMS cell temperature higher than T = 150 °C was required to affect separation; see Appendix A Figure A-15 for the resolution of (−)-THCA and CBDA ionogram peaks under T = 150 °C. Figure 3-3F shows the result of an experiment employing a 1:1 mixture of (−)-THCA and CBDA; THCA and CBDA can be individually selected at CV = −9 V and CV = −7 V, respectively, at SV = 4250 V. As was the case with the decarboxylated analogues, the ion signals for THCA and CBDA in the mixture do not exhibit a 1:1 ratio owing to differences in ionization efficiency. The observed difference in relative intensity (attributed to differences in ionization efficiencies) are consistent with previously reported observations on IMS-separated cannabinoid isomers.[120] Although the ionograms in Figure 3-3C and F do not show baseline separation between the isomers, as can be seen in Figure 3-3B and E, the individual isomers can be selected at their optimal CV values for transmission.

3.3.3 Direct Infusion Analysis of Marijuana Flower Extract

To test our method for DMS-based cannabinoid separation and quantification, a "dilute-and-shoot" approach was investigated for IPA-extracted marijuana flower (Blueberry Haze). Refer to the supplementary information for the quantification of the other extracts. Figure 3-4A shows the mass spectrum recorded in the *m/z* 0 – 400 region for a 400 ng/mL sample of marijuana flower extracted into IPA. The *m/z* 357.2 ion signal associated with (−)-THCA and CBDA is significantly more intense than the *m/z* 313.2 ion signal associated with the decarboxylated isomers, as is expected.[132–134] Using known multiple reaction monitoring (MRM) transitions, ionograms were recorded

under optimal DMS conditions to conclusively identify and separate the target species. Note that slight shifts are observed between the optimal CV values found for the compounds when analysed in the extracted flower samples compared to the pure standards. These shifts may be attributed to matrix effects. Figure 3-4B plots the ionogram recorded for the *m/z* 357.2 → 313.2 MRM transition associated with (−)-THCA and CBDA. Of the two carboxylated isomeric species, (−)-THCA is by far the larger contributor to the total ion population. Figure 3-4C shows the ionogram recorded when monitoring both the *m/z* 313.2 → 245.2 and *m/z* 313.2 → 191.2 MRM transitions associated with Δ^9-THC, CBD, and CBC. In this case, ion signals associated with Δ^9-THC and CBD were observed in approximately equal intensity, and there was no evidence of CBC contribution to the *m/z* 313.2 mass peak.

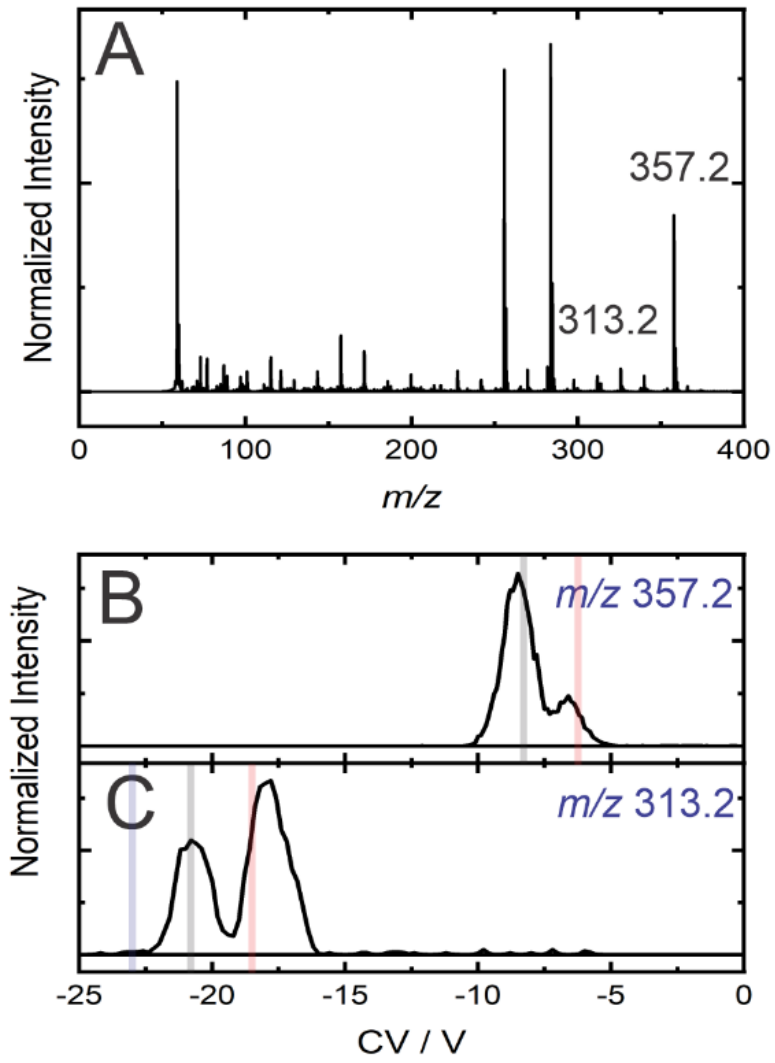

Figure 3-4. (A) The mass spectrum of the 400 ng/mL marijuana flower extracted in IPA shows a high abundance of m/z 357.2 (i.e., (−)-THCA and CBDA) and a relatively low abundance of m/z 313.2 (i.e., Δ^9-THC and CBD). (B) Ionogram showing the presence of a relatively high abundance (−)-THCA and a low relative abundance of CBDA in the extracted sample. (C) Ionogram showing the presence of a relatively high abundance of Δ^9-THC and CBD. CBC, if present, was below the limit of detection. The optimal CV values of the pure standards are marked by vertical lines corresponding to the colours of the standards from Figure 3-3.

To quantify the isomeric species in the marijuana sample, standard addition calibrations were undertaken (see Appendix A Figure A- 16, Figure A- 17, and Table A- 4). For the carboxylated species, this procedure yielded 0.234 g (−)-THCA and 0.0465 g CBDA, corresponding to 21.5% ± 0.6 (*w/w*) (−)-THCA and 2.2% ± 0.2 (*w/w*) CBDA in the

marijuana flower sample. These values align with expectation for commercial marijuana flower.[133] THC, CBD, and CBC were approximately 10 times lower in abundance than CBDA and below the limit of quantification for the dilute-and-shoot method that we employed. These low relative abundances align with expectations based on previous reports of the amounts of decarboxylated cannabinoid isomers in marijuana flower samples.[113–115] Quantification of the isomers in this set is shown in the supporting information (Figure A- 22 to A-24 Table A- 7).

This method of separation and quantification can be extended to other cannabis products (e.g., extracts, tinctures).[135,136] Other applications include drug testing. However, when adapting this method, one should consider matrix effects for different samples. The limits of quantification and detection reported here are associated with the sensitivity of the mass spectrometer. These limits could be improved for the purpose of sample analysis via a preconcentration step (e.g., using SPE or SPME).[137–140]

3.4 Conclusions

DMS-MS is an effective, rapid method for separating and detecting the cannabinoid isomer sets, Δ^9-THC, CBD, CBC, (−)-THCA, and CBDA. Direct infusion via ESI yields protonated and deprotonated species; analysis of the deprotonated isomers was found to yield better results owing to increased relative stability and improved signal-to-noise levels. Optimal DMS separation was achieved at high separation voltages using IPA modifier. IPA was found to disrupt strongly bound adducts generated via ESI, thereby producing single ionogram peaks and simplifying the DMS analysis. Under optimal separation conditions, analysis of equal mixtures of cannabinoid standards indicated that the isomeric species exhibit different ionization efficiencies. Nevertheless, near-baseline resolution and quantification can be achieved.

The use of IPA to extract cannabinoids from marijuana flower enabled testing the DMS-MS separation and quantification method in a rapid dilute-and-shoot workflow. Quantification of the carboxylated isomers, THCA and CBDA, yielded values in agreement with expectations for commercial marijuana samples. The decarboxylated

isomers, THC and CBD, were also detected in the extracted flower, but at levels below limits of quantitation for our standard addition method. The CBC isomer, if present, was below our limit of detection. Should quantification of these species be desirable, pre-concentration methods such as SPE or SPME should be employed in conjunction with DMS-MS.

The use of DMS-MS in a dilute-and-shoot format yields accurate results for cannabinoid isomer quantification within a few minutes from flower extraction to sample analysis, with the extraction step being the process bottleneck. This method can be extended to the analysis of other cannabis products (e.g., edibles, tinctures) and potentially biological samples such as urine, with the caveat that matrix effects should be considered. The throughput could potentially be further improved with the introduction of newer sampling methods such as an open port probe interface,[141] which could enable sampling on-the-fly and on-site analysis in the field.

Chapter 4: The Study of Positional Isomers using DMS and UVPD

In the previous chapter, DMS-MS was shown to allow for the separation, identification, and quantification of isomers. Other means of distinguishing isomers that are indistinguishable through tandem MS alone includes the incorporation of UVPD. In this chapter, the positional isomers, nortriptyline and protriptyline, which exhibit the same *m/z* and fragment ions are investigated using DMS-MS coupled with UVPD. In this case, the application of UVPD is assessed to identify and distinguish the two isomers by selective fragmentation. The work presented in this chapter is prepared for publication.

4.1 Introduction

The utility of mass spectrometry (MS) in the analysis of complex mixtures can be impeded by the presence of isomeric and isobaric compounds that present the same *m/z* values during analysis. Although tandem MS circumvents this issue for most isomeric species by enabling the observation of unique fragmentation patterns, isobars that yield the same product ions with similar relative abundances may still confuse sample analysis. Orthogonal methods, such as high-performance liquid chromatography (HPLC) and gas chromatography (GC), are typically introduced prior to MS to separate closely related isomers. Although versatile, these conventional methods typically require relatively long run times. Another orthogonal technique to MS is differential mobility spectrometry (DMS), which can be used to quickly separate isomers prior to mass spectrometric (MS)

investigations and simultaneously provide information on the physicochemical properties of analytes.[40,65–67,142]

In a recent study, Coughlan et al. successfully separated and characterized positional isomers of quinoline by modifying a DMS-MS instrument to incorporate ultraviolet photodissociation (UVPD) spectroscopy.[143] In this proof-of-concept study, the quinoline isomers presented different product ions in CID methods, allowing for their unambiguous identification without UVPD. In cases where isomers are not distinguishable by MS techniques alone, UVPD can provide richer fragmentation patterns by depositing greater amounts of internal energy into a molecule. UVPD can thus access higher excited states that often lead to fragmentation pathways that may otherwise be unobtainable by lower energy fragmentation methods, such as collisional and electron activation techniques.[83,90] Moreover, the action spectra obtained by UVPD can reliably distinguish DMS-selected prototropic isomers.[69,93] For example, the UVPD investigation of para-aminobenzoic acid distinguished prototropic isomers present at set gas-phase conditions.[69] UVPD analysis in the case of para-aminobenzoic acid allowed for identifying the purity of the populated species, thus, introducing an additional confirmation tool to the DMS analysis of analytes.

In the case of conjugated systems, studies have highlighted the significance of substituent position on a molecule's physicochemical properties.[40,63,68] For instance, the investigation of quinoline and isoquinoline isomers in the DMS showed that the position of the nitrogen atom along the aromatic system influenced both the clustering behavior and the photo-dissociative spectra of the molecules.[143] Meanwhile, Walker et al. noted the effect of an amine substitution in aniline on the ability in forming a carbocation in electrospray ionization.[40] Both studies suggest that the position of substituents can affect the behavior of an ion through resonance and induction effects. On the other hand, positional isomers of phosphocholine lipids were reported to exhibit changes in clustering behavior owing to the steric effects on the geometry of an analyte that can hinder or enhance intermolecular interactions depending on the position of a single double bond.[144]

Nortriptyline and protriptyline are positional isomers that differ by the position of a double bond about the tricyclic region (see Figure 4-1). Perhaps unsurprisingly, the two isomers exhibit approximately the same effectiveness in treating depression, yet, interestingly, they exhibit different side effects.[145] As a result, the isomers are often selected for patient treatment based on their side effects.[145] The positioning of the double bond affects the extent of conjugation exhibited in each isomer. In the case of protriptyline, the position of the double bond extends the π-system of the aromatic ring moiety compared to nortriptyline where the double bond occurs on the alkyl chain (see Figure 4-1).

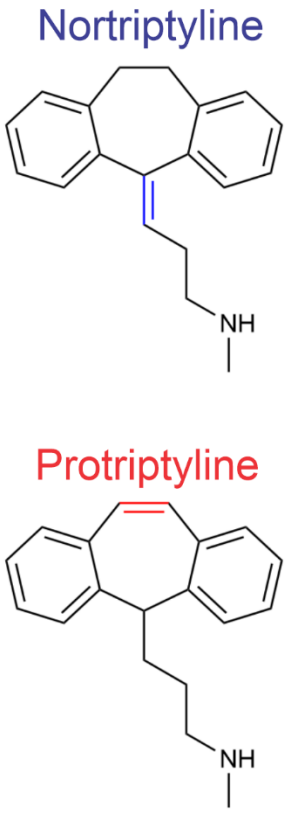

Figure 4-1. The structures of nortriptyline and protriptyline differ by the position of a single double bond highlighted in blue for nortriptyline and red for protriptyline.

While the position of the double bond does not affect the ionization efficiency about the amine group, it may lead to differences in geometric and steric effects along with differences in intramolecular interactions. Extensive studies on the spectroscopic behavior of nortriptyline and protriptyline and their analogues explored the excited state transitions

taking place when irradiating the neutral species.[146–148] Absorption studies attributed the difference in the absorption spectra of nortriptyline and protriptyline to their conjugated systems. These differences can be exploited to separate the two isomers for identification and quantification purposes.

We employed DMS-MS to separate nortriptyline and protriptyline based on the differences in their gas-phase behavior. Using a modified gas environment, we investigated the effect of the double bond position in nortriptyline and protriptyline on their clustering properties in the DMS. Computational work followed to complement the DMS behavior of each isomer. Once separated, isomers were subjected to UVPD studies to obtain their respective action spectra, noting any differences in their electronic structure which may be leveraged for fixed-wavelength UVPD characterization.

4.2 Methods

4.2.1 Experimental methods

Pure standards of nortriptyline and protriptyline (Millipore Sigma) were diluted in a 50:50 mixture of methanol and water containing 0.1% formic acid. Dilute samples were directly infused via electrospray ionization into the DMS-MS instrument for analysis (ESI; TurboV IonSpray, SCIEX, Concord). The analytes were investigated under pure N_2 gas-phase DMS conditions and in N_2 seeded with 1.5% (*v/v*) acetonitrile (MeCN). Upon determining optimal separation conditions, mobility- and mass-selected ions were trapped in the Q3 linear ion trap (LIT) for 500 ms and irradiated with the output of a Nd:YAG pumped optical parameter oscillator (OPO) operating in the 208 – 400 nm range with a frequency of 10 Hz. The mass spectra produced following laser irradiation were acquired for an average of 30 s, averaging 10 MS scans at each wavelength. Plotting the photofragmentation yield as a function of wavelength generated the photodissociation action spectrum for each analyte.

4.2.2 Computational methods

The potential energy surface (PES) of each protonated isomer and each ion-solvent cluster (N=0-3 solvent molecules) was sampled using the basin hopping (BH) algorithm to identify low-lying energy conformers.[72,127,128] Approximately 20,000 geometries were sampled for each ion and ionic cluster. Low-lying energy conformers identified by the BH algorithm selected and reoptimized at the density functional level of theory using the B3LYP functional[80] and the 6-311 + G(d,p) basis set.[79] The Grimme D3 correction was applied to account for dispersion forces.[130] Thermochemical calculations as implemented in the Gaussian 16 suite were then conducted to rationalize the observed gas-phase DMS behavior.[149] Excited state calculations were conducted using the ORCA program.[101,102] The vertical gradient Franck-Condon (VGFC) approximation was used to simulate the vibronic absorption spectrum of each protonated isomer at the B3LYP/6-311G level of theory.[103,104] Natural transition orbital (NTO) calculations were performed to visualize the electronic excitations.[150]

4.3 Results and discussion

4.3.1 Differential mobility spectrometry Analysis

The dispersion plots recorded for nortriptyline and protriptyline in a pure N_2 environment are plotted in Figure 4-2. For both analytes, a single ionogram peak was observed across all SV for all temperature and modifier conditions investigated. This suggests that only a single prototropic isomer is produced for each analyte during the ESI process. Separation of the two analytes was achieved in both the pure N_2 and the solvated conditions. A slight difference in DMS trajectories is observed for nortriptyline and protriptyline in pure N_2 conditions at T = 150 °C (see Figure 4-2A).

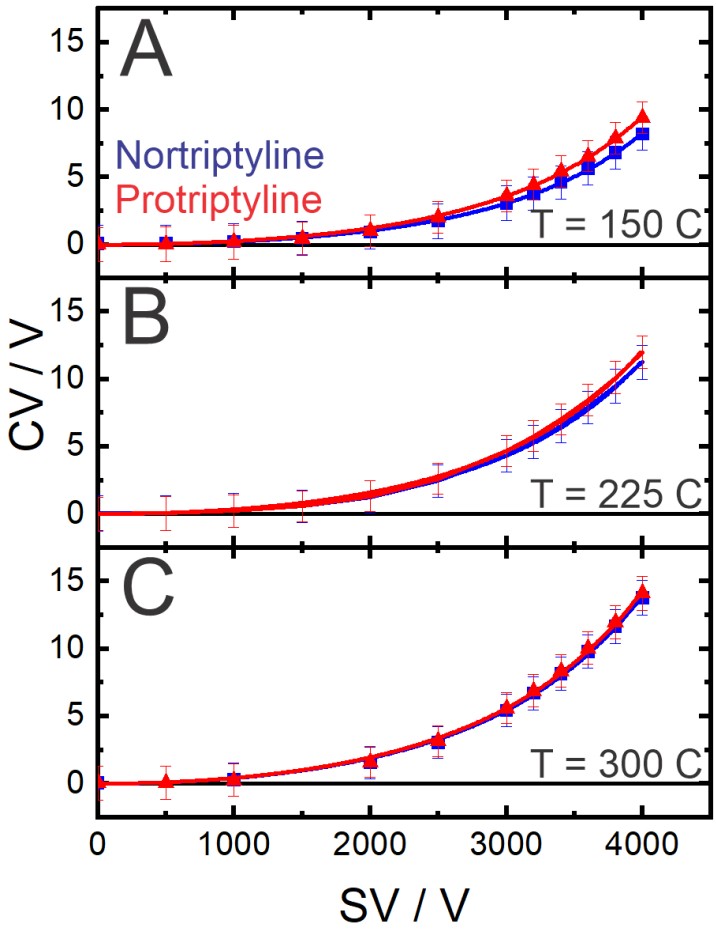

Figure 4-2. Dispersion plots of nortriptyline (*blue*) and protriptyline (*red*) in a pure N_2 environment at temperatures of (**A**) T = 150 °C, (**B**) T = 225 °C, and (**C**) T = 300 °C.

As the temperature of the cell increases, the DMS trajectories converge. A recent study by Ieritano et al. demonstrated that the DMS trajectory of ions in the pure N_2 conditions can be correlated to their collision cross sections (CCSs) using machine learning (ML).[81] The DMS trajectories of nortriptyline and protriptyline in pure N_2 were inputted into the ML model to determine the isomers' CCS values. Nortriptyline (164.5 $Å^2$) and protriptyline (162.8 $Å^2$) present small differences in CCS values, that could explain the slight separation observed in N_2.[151]

Optimized structures of the isomers in the gas phase, as shown in Appendix B Figure B- 6, demonstrate that weak intramolecular interactions may play a role into the slight

separation observed at lower temperature conditions. Optimized structures show cation-π interactions between the charged amine and the π system of one of the delocalized rings (see Appendix B Figure B- 6). The Boltzmann-distributed CCS values of nortriptyline and protriptyline were calculated to be 160.4 $Å^2$ and 161.5$Å^2$, respectively.[81,152] While in agreement with CCS values determined experimentally, given the minimal differences in structure, it is believed that the slight variation in DMS behaviour under a pure N_2 environment could be a result of minimal and negligible interaction with the neutral gas molecules.

Seeding MeCN into the carrier gas enhanced the DMS separation of the two isomers (see Figure 4-3). The CV shifts observed with increasing SV values are consistent with Type A behavior for both isomers, indicating strong clustering with the modifier. Differences in optimal CV values indicate differences in the clustering behavior. Computational studies of each isomer with N = 0 – 3 MeCN solvent molecules were performed. In all studies, the charge site in both nortriptyline and protriptyline remained exposed, allowing for the same extent of clustering to occur. Thus, differences in DMS behavior must then be attributed to differences in the ion-solvent interaction strengths of each isomer. Calculated binding energies were determined to be 50 $kJ\,mol^{-1}$ for the singly-solvated protriptyline–MeCN cluster and 41 $kJ\,mol^{-1}$ for nortriptyline–MeCN cluster, showing significant differences in intermolecular interaction strength. Calculated binding energies for the isomer with N = 0 – 3 MeCN molecules are shown in the Appendix B Table B- 1. Differences in binding energies are associated with the rate of declustering and clustering taking place in the DMS and may thus explain the significant difference in differential mobility.[58,60]

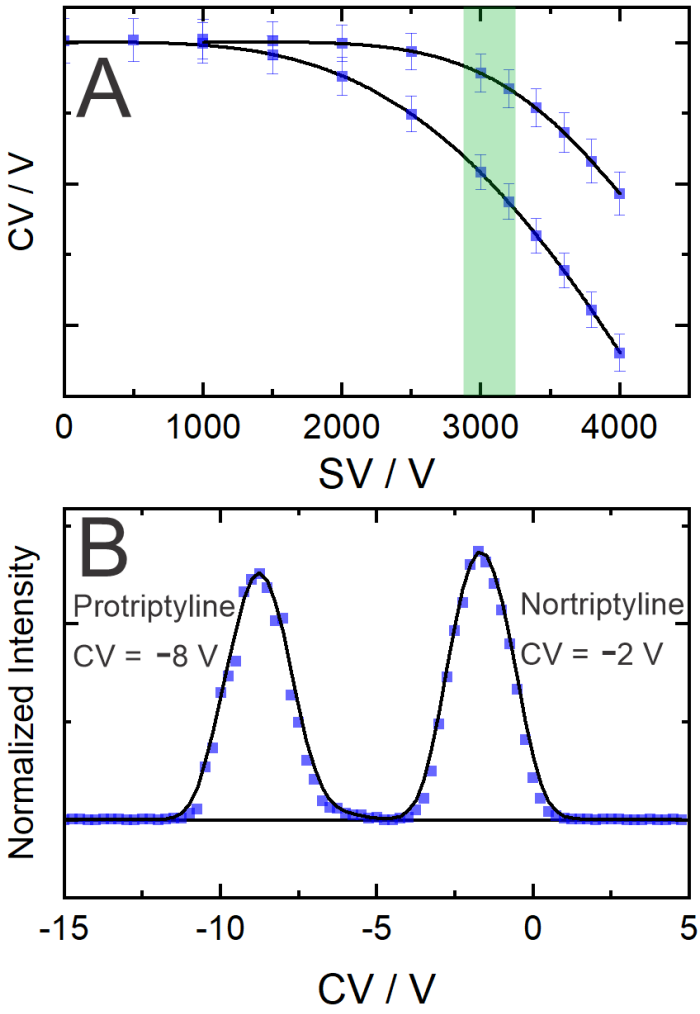

Figure 4-3. (**A**) Dispersion plots of individual nortriptyline and protriptyline standards in N_2 seeded with 1.5% (*v/v*) MeCN at T = 150 °C. (**B**) An ionogram of a 50:50 sample mixture of nortriptyline and protriptyline separated at SV = 3000 V in the MeCN-modified environment.

The two isomers are successfully isolated in a sample mixture, by optimizing conditions in the MeCN-modified environment in the DMS (see Figure 4-3B). DMS offers rapid separation of isomers within seconds and the investigation of ion interactions in the gas phase, demonstrating its robustness and versatility in the study of gas-phase ions. When investigating the isomers using tandem MS, nortriptyline and protriptyline produced the same fragments, albeit at different relative abundances (see Appendix B Figure B- 1). The assignment of dominant product ions was adapted from previous studies.[153,154] It is evident

that MS^n methods alone cannot reliably distinguish the two isomers, owing to the production of the same fragment ions in both cases. UVPD analysis was conducted to overcome issues of identifying and characterizing nortriptyline and protriptyline.

4.3.2 UVPD Analysis

UVPD action spectra were acquired for protonated nortriptyline and protonated protriptyline in pure N_2 DMS conditions and under an MeCN-modified environment. In both gas-phase conditions, the action spectra indicate the presence of a single prototropic isomer of nortriptyline and protriptyline.[146,155] A comparison of the UVPD action spectra acquired for nortriptyline and protriptyline is shown in Figure 4-4. The two isomers exhibit different spectra in the 250 – 350 nm region. The spectral differences provide a method of separating and identifying the triptyline isomers via single wavelength UVPD (see Figure 4-4A); at approximately 300 – 320 nm, the protriptyline isomer can be selectively irradiated, whereas irradiation at 250 nm induces photofragmentation of nortriptyline.

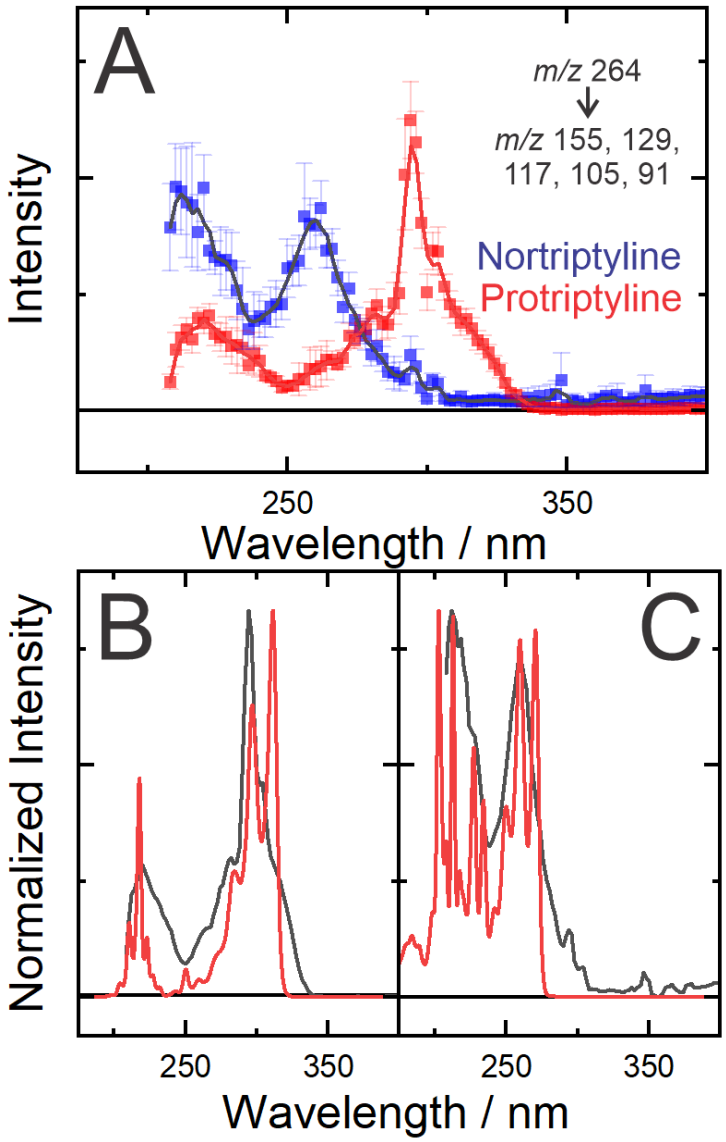

Figure 4-4. The UVPD spectrum of isolated nortriptyline (CV = −2 V) and protriptyline (CV = −10 V) at SV = 3000 V in a MeCN-modified environment generated by monitoring all major fragmentation pathways. A comparison of the calculated VGFC absorption spectra and the experimental UVPD spectra for (**B**) protriptyline and (**C**) nortriptyline.

Panels B and C in Figure 4-4 show that the UVPD action spectra of nortriptyline and protriptyline were well-reproduced by the computed vibronic absorption spectra. The computed vibronic spectra using the VGFC approach not only represented the transition energies well, but successfully aligned with the relative intensities of the peaks.

Additionally, the fragmentation patterns generated by photodissociation of the ions matched relatively well with those found using CID (see Appendix B Figure B- 1).

Detailed investigations into the excited state transitions leading to the spectral bands in each isomers were conducted through the use of natural transition orbitals. The individual contribution, dictated by the calculated oscillator strength, of each electronic transition is found in Appendix B Table B- 2 and Table B- 3. It is noted that the electronic oscillator strengths do not align exactly with those observed experimentally. Instead, the greatest accuracy in relative absorbance is best described by the vibronic contributions, as illustrated in Appendix B Figure B- 4 and Figure B- 5. Looking at the vibronic contributions, the lower energy band for both isomers arise from their $S_0 \rightarrow S_1$ transitions, and fine-spectral features are associated with vibrational structure as determined by Franck Condon overlap of the ground and excited states. Inspection of the transition orbitals of the first band feature (see Figure 4-5) reveals differences in the excitations taking place for each isomer.

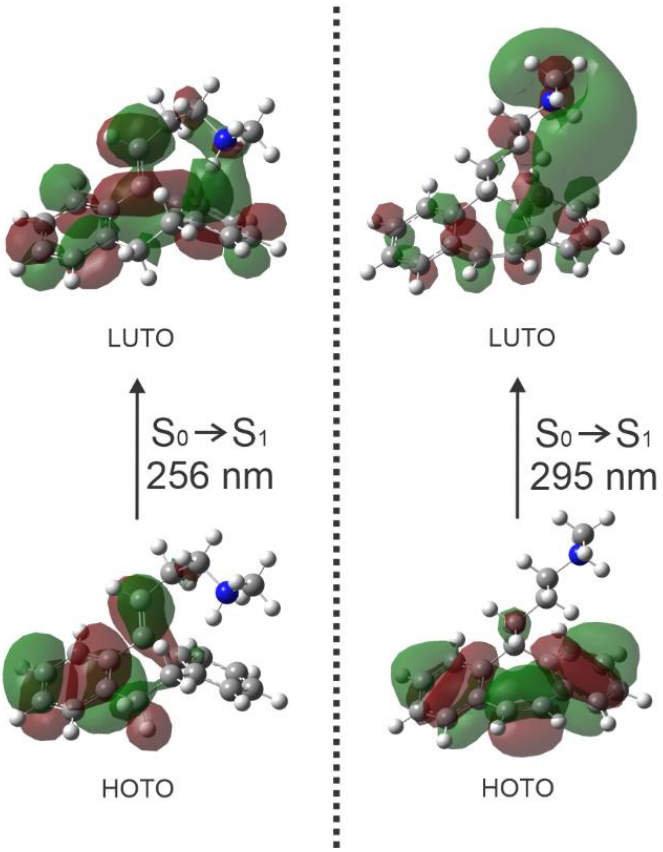

Figure 4-5. The Transition orbitals of nortriptyline (*left*) and protriptyline (*right*) associated with the $S_0 \rightarrow S_1$ transitions resulting in absorption at ≈ 250 nm and ≈ 300 nm, respectively.

The $S_0 \rightarrow S_1$ transitions of both isomers are associated with a π→π* excitation and charge transfer from the aromatic π system to the amide group. Transition orbitals calculated for the $S_0 \rightarrow S_1$ transition for each isomer confirms the extended π-system found on protriptyline when compared to that of nortriptyline. Thus, a red-shift in the absorption of the $S_0 \rightarrow S_1$ transition for protriptyline is attributed to the extended π-system observed. The spectral feature observed in the 200 – 250 nm region is predominantly associated with the $S_0 \rightarrow S_8$ and $S_0 \rightarrow S_{11}$ transitions for nortriptyline and the $S_0 \rightarrow S_{10}$ transition for protriptyline (see Figure 4-5 and Appendix B Figure B5). Again, transitions observed for this spectral band include a π→ π* transition with transfer of electron density from the conjugated π-system to the amide group.

Upon inspection of the mass spectrum generated from photodissociation, the fragmentation efficiencies of protriptyline and nortriptyline differed significantly, as seen in Figure 4-6. Protriptyline yielded a greater photodissociation efficiency, yielding fragment intensities close to 60% of the parent mass. On the other hand, nortriptyline yielded fragment intensities of less than 15%. Differences in fragmentation efficiencies, that are not as prominently seen using CID (see Appendix B Figure B- 1).

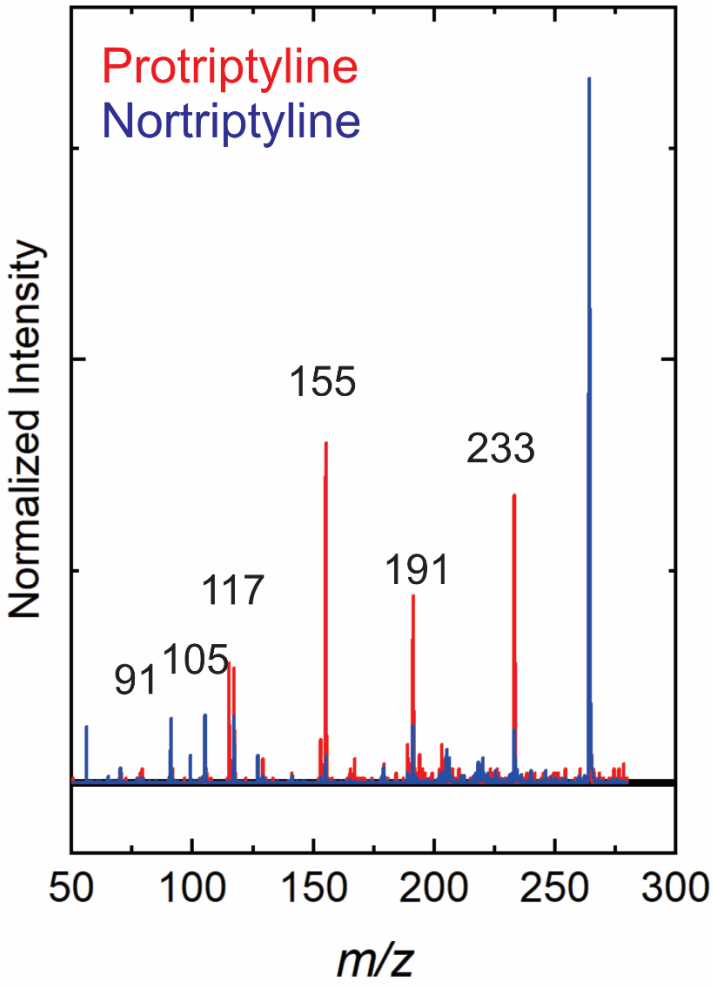

Figure 4-6. The normalized fragmentation efficiencies of nortriptyline (blue) and protriptyline (red) at the heigh of absorption at similar laser powers.

The observed photodissociation efficiencies suggest different excited state dynamic processes experienced by the isomers. The starkly contrasting photodissociation efficiencies can be used in the identification and quantification of the two isomers using UVPD, when mass spectrometry is employed alone. Protriptyline undergoes photodissociation upon excitation at 300 nm whereas nortriptyline does not, selective fragmentation for quantification purposes is possible. In cases where both isomers are present in a complex mixture, one can measure the relative fragmentation at 300 nm to determine the relative composition of protriptyline in the sample. Although the photodissociation efficiency of protriptyline exceeds that of nortriptyline, the selective fragmentation of certain fragment ions at 250 nm offers quantitation of nortriptyline. Excitation at 250 nm will predominantly yield *m/z* 91 and 105 fragments from nortriptyline, as the fragmentation efficiency to produce these ions is significantly greater in nortriptyline than in protriptyline, see Appendix B Figure B- 2.

4.4 Conclusions

Positional isomers, nortriptyline and protriptyline, were investigated in a DMS-MS instrument coupled with UVPD. The isomers presented different DMS and UVPD behaviors owing to the position of a single double bond. The extended π-system of protriptyline led to a smaller CCS value due to enhanced cation-π interactions compared to nortriptyline. The effect of the weak intramolecular interactions was observed under low DMS temperatures. The differences in weak intramolecular interactions were overcome at high temperature conditions, leading to near identical differential mobility for the two isomers under pure N_2 conditions. Enhanced separation was observed in the MeCN-modified environment, resulting from stronger binding interactions between protriptyline and the solvent vapor.

Customizing the DMS-MS instrument to enable UVPD analysis provided a method to conclusively distinguish protriptyline and nortriptyline, where tandem MS failed. Of course, distinguishing the two analytes with UVPD requires a knowledge of their spectra for comparison purposes, which means practitioners must have access to a spectral

database or to fast vibronic structure calculations for this method to be practical in an analytical laboratory setting. Moreover, a light source of appropriate wavelength and power is requisite. This latter condition may become more affordable as LED technology continues to progress.[156] The DMS-MS setup coupled with UVPD provides an analytical method for sufficient identification and separation of the TCA isomers, nortriptyline and protriptyline. The setup can be further expanded to other isomeric cases for more thorough investigations of the electronic and geometric structures of ions.

Chapter 5: The Investigation of Rivaroxaban Prototropic Isomers using DMS coupled with UVPD

As seen in the previous chapter, the incorporation of DMS and UVPD to complement MS analysis of isomers provides a means for in-depth characterization of isomers. The application of the setup can be further expanded to the analysis of conformers preserved during the ESI process, which may aid in determining solution-phase conformations of analytes. In this chapter, the coupling of DMS-MS with ultraviolet photodissociation is used to characterize the different conformers of an anticoagulant drug molecule, rivaroxaban. It was determined that the different gas-phase environments introduced into the DMS cell preserved and separated ESI-formed prototropic isomers of Rivaroxaban. Although Tandem MS was unable to distinguish the conformers of protonated Rivaroxaban produced by ESI, UVPD could be used to distinguish these species based on differences in their electronic structures.

The work described in this chapter was published in 2021 following peer-review in the Journal of Physical Chemistry A. The article can be found in *J. Phys. Chem. A 2021, 125, 37, 8187–8195.*

5.1 Introduction

Prototropic isomers (*i.e.*, molecular isomers exhibiting different protonated sites) of biologically relevant molecules are important in some biological processes. For example, the presence of tautomers in DNA is known to result in mutations affecting helix formation.[157] On the other hand, UV induced proton transfer has been shown to limit the accumulation of radicals in DNA, preventing damage.[158] Other examples include the selective binding of carbamylcholine and nicotine to tautomeric ligand sites in human receptors.[159] Research has shown that the molecular environment (e.g., solution conditions) can significantly impact the relative population of the tautomeric species.[160,161] Researchers have taken advantage of this behavior to preferentially produce and study specific prototropic isomers via electrospray ionization (ESI) mass spectrometry.[38]

Several investigations[39,162–165] have demonstrated that ESI can be used to form an ensemble of prototropic species that includes kinetically-trapped high-energy isomers.[161,166] In some cases, one can target a particular tautomer by selecting the appropriate ESI solvent.[160,166] Factors affecting the population of prototropic species during the ionization process include the ionic strength, pH, and gas-phase acidity/basicity of the solvent.[38,167] For example, ESI solvent effects are observed in studies of para-aminobenzoic acid (PABA) where employing protic versus aprotic ESI solvents results in preferential protonation of the carboxylic acid or amino moieties, respectively.[28,168] Although the prototropic isomers of protonated PABA can be identified by their fragmentation patterns following collision induced dissociation (CID), it is often the case that ambiguities with respect to structural assignment arise for ensembles containing multiple isomers. In these situations, it is beneficial to employ orthogonal characterization techniques such as ion mobility spectrometry to separate isomeric species in advance of their dissociation.[28,166]

In 2020, Coughlan *et al.* modified a commercially available DMS-MS system to enable ultraviolet photodissociation (UVPD) spectroscopy of DMS-separated positional isomers.[143] Similar UVPD-coupled ion mobility studies have also successfully separated isomers of relative small ions.[90,92,169] These IMS studies lack the clustering process offered in DMS. UVPD spectroscopy provides an orthogonal method to complement traditional

mass spectrometric characterization techniques such as CID, electron capture dissociation (ECD), and hydrogen/deuterium exchange (HDX). HDX is a technique that relies on differences in the rate of exchange of labile protons to distinguish conformers and tautomeric species; it is formidable in the analysis of protein structures and intramolecular hydrogen bonding networks in large molecules but cannot conclusively identify geometric structure.[71] On the other hand, techniques such as ECD and electron induced dissociation (EID) are more widely used for isomer and conformer identification. ECD and EID limit the proton scrambling typically seen in CID. ECD also introduces little vibrational energy, maintaining any non-covalent intramolecular interactions.[91,170] Thus, tautomers and protein structures are better preserved. Issues typically encountered in ECD is the preferential dissociation of unfolded protein conformers due to their higher charge states, which is overcome by EID.[170] Yet, extensive fragmentation and selective dissociation is better achieved using UVPD.[170] Single wavelength UVPD can be used to interrogate target ions and produce fragmentation patterns that may be different from those observed by tandem MS.[89] When a tunable laser is available, UVPD fragmentation products can be monitored as a function of wavelength to generate an action spectrum that may be employed to conclusively identify isomeric species.[83,90]

Rivaroxaban, also known by the brand name Xarelto, is an anticoagulant medication used to prevent and treat blood clots in humans.[171] Rivaroxaban is a good candidate for producing multiple tautomers owing to the presence of several basic sites (Figure 5-1). The flexible backbone of the molecule additionally allows for multiple conformational arrangements, adding to the geometric complexity of the molecule. As a result, several of the potential protonation sites of Rivaroxaban can participate in proton sharing, further increasing the number of tautomers potentially formed via ESI. Here, we employ UVPD to investigate DMS-selected prototropic isomers of Rivaroxaban.

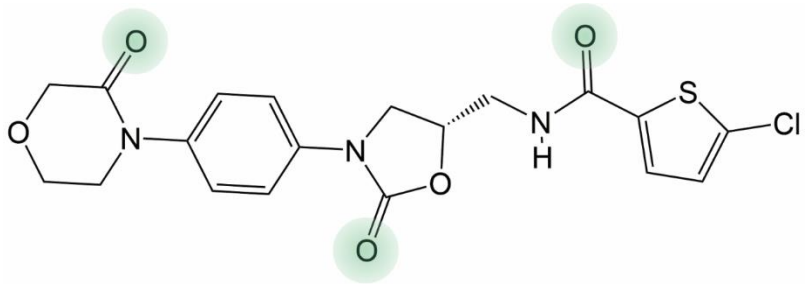

Figure 5-1. The molecular structure of neutral Rivaroxaban (aka Xarelto). The computed sites of highest gas-phase basicity are highlighted in green (*vide infra*).

5.2 Methods

5.2.1 Experimental Methods

The detailed instrument conditions employed for the experiments described in this manuscript are provided in Appendix C Table C- 1. The experimental apparatus has been described elsewhere.[24,63] Samples of Rivaroxaban, (S)-5-Chloro-N-((2-oxo-3-(4-(3-oxomorpholino)phenyl)oxazolidin-5-yl)methyl)thiophene-2-carboxamide, were acquired from Rivaroxaban tablets (10 mg Rivaroxaban) that were ground and diluted to 60 ng/mL (Rivaroxaban concentration) in a 1:1 methanol:acetonitrile + 5mM ammonium acetate solution. The diluted sample was electrosprayed with a Turbo V ion source (SCIEX) operating in positive mode. Ions were transferred into a differential mobility spectrometer (SelexION, SCIEX) and were studied under a pure N_2 environment, along with an N_2 environment seeded with 1.5% (*v/v*) acetonitrile (MeCN) vapor to investigate clustering behavior and the effect on isomer relative populations.

Prior to UVPD spectroscopic characterization, mobility- and mass-selected [Rivaroxaban + H]$^+$ (*m/z* 436.1) was accumulated in Q3 of the modified QTRAP 5500 system for 500 ms.[143] A Nd:YAG-pumped tunable optical parameter oscillator (OPO, Continuum) operating in the 208 – 400 nm region was coupled into Q3 of the hybrid DMS-MS instrument. Trapped ions were irradiated by the output of the OPO for an acquisition time of 30 s (operating at 10 Hz, average energy of ~10 mJ per pulse), leading to dissociation upon resonant absorption. Resultant fragment ions were mass analyzed using mass-selective axial ejection.[172] UVPD spectra were generated by plotting the

fragmentation efficiency of the ion as a function of the laser wavelength as per equation 5-1:

$$I(\lambda) = \frac{1}{E_p(\lambda)} - log\left[\frac{\sum I_{parent,\lambda}}{\sum I_{fragment,\lambda} + \sum I_{parent,\lambda}}\right], \qquad [\quad 5\text{-}1 \quad]$$

where the fragmentation efficiency is normalized to the pulse energy, $E_p(\lambda)$. The resultant action spectrum is related to the absorption spectrum of an ion, as fragmentation efficiency is dependent on both the absorbance of the ion at a specific wavelength and the rate of decay of the excited molecule. However, differences between the two types of spectra are expected, as not all absorption processes lead to fragmentations. A detailed explanation of UVPD is provided elsewhere.[87,173]

5.2.2 Theoretical Methods

Tautomers of protonated Rivaroxaban were manually generated and geometrically optimized at the DFT/B3LYP 6-311++g(d,p) level of theory. Although protonation sites on all heteroatoms were initially investigated, three sites (carbonyl oxygen centers) were found to be the most energetically favorable sites and so were carried forward for more in-depth studies.

To explore the potential energy surface of each tautomer, a custom basin hopping (BH) algorithm was employed.[72,127,174] Dihedral angles were randomly distorted by an angle $-15° < \theta < 15°$, and molecular energies were calculated using the UFF forcefield.[75] In total, ca. 20,000 structures were sampled by the BH algorithm for each prototropic isomer. Unique conformers, as determined based on energetic and geometric similarities,[127] were further optimized using the B3LYP functional and 6-311++g(d,p) basis set as implemented in Gaussian 16 and including Grimme dispersion corrections (D3).[149] Implicit solvation studies were conducted to investigate ion behavior in MeCN-modified environments. QST3 calculations were employed to explore the transition state structures between tautomers and assess the activation energy for interconversion.[149]

To calculate the six lowest energy electronic transitions of the three most stable conformers, the ORCA suite was employed utilizing the CAM-B3LYP/6-311g(d,p) model chemistry.[101,102] The vibronic band profiles were calculated using the vertical gradient Franck Condon (VG|FC) approximation.[80,103,175,176] Natural transition orbital (NTO) analyses in the ORCA program were conducted to visualize the electronic excitations using the localized transition density matrix.[150]

5.3 Results and Discussion

5.3.1 Pure N_2 DMS Environment

The dispersion plots for protonated Rivaroxaban in a pure nitrogen environment at three temperatures (T = 150, 225, 300 °C) are shown in Figure 5-2A. Type C behavior is observed at all temperatures owing to the weak ion-neutral interactions between protonated Rivaroxaban and N_2. A second feature is observed in the ionogram as the DMS cell temperature is increased. Observation of multiple DMS ionogram peaks is indicative of either separation of isomers and conformers or the presence of larger clusters that fragment to produce the target species prior to mass spectrometric analysis.[67] As the temperature of the DMS cell increases, two effects are observed: (1) a shift in CV to more positive voltages and (2) variation in the relative intensities of the two ionogram features. The positive shift in CV occurs with increasing temperature owing to a reduction of Gibbs energies of intermolecular interactions between the analyte molecules and the collision gas.[177] With respect to peak intensities, one finds that the feature at CV ≈ 11 V (peak I_a) depletes with increasing temperature (see Figure 5-2). This observation suggests that the ion population in peak I_a is associated with a weakly-bound Rivaroxaban-containing complex; when fragmentation of the adduct occurs at higher temperatures in the DMS cell, those species are no longer transmitted. An increase in the intensity of the CV ≈ 15 V (peak I_b) feature is observed with increasing temperature. We hypothesize that this increase in intensity stems from a higher rate of ion-solvent cluster evaporation at the DMS entry point, and therefore increased production of bare ions, driven by the elevated gas temperatures.

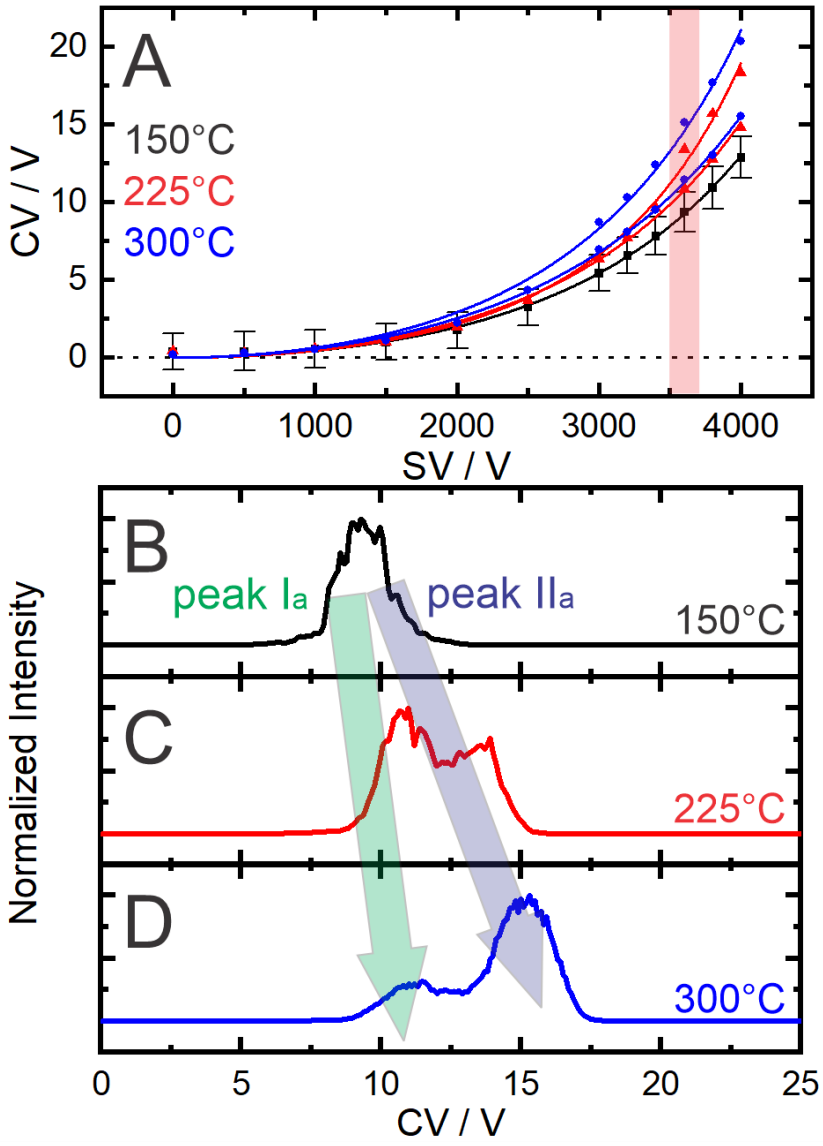

Figure 5-2. (A) Dispersion plots for Rivaroxaban in a pure N2 environment at three different DMS temperatures (T = 150, 225, 300 °C). Representative error bars shown for the dispersion curve at T = 150 °C plot the full width half maximum of the Gaussian peaks. The ionograms recorded at SV = 3600 V for the region highlighted with the vertical red bar are shown in panels (B) T = 150 °C, (C) T = 225 °C, and (D) T = 300 °C.

To determine which ions were being transmitted under the DMS conditions corresponding to the ionogram peaks, the precursor ion scans were taken at fixed SV/CV values. The clusters eluting from the DMS cell were preserved by setting the declustering potential to DP = 0 V,[67] and protonated Rivaroxaban was monitored via the *m/z* 436 → 145 MRM transition. The results of these scans for SV = 3600 V and T = 300 °C are provided

in Appendix C Figure C- 1. The precursor ion scan for peak II_a exhibits a single *m/z* peak for the bare protonated Rivaroxaban ion, $[M + H]^+$ (*m/z* 436). Calculating the alpha curve across the three temperatures (see Appendix C Figure C- 2)[178] confirms that the ion population behavior is consistent with that of a bare ion. In contrast to peak II_a, peak I_a exhibits an additional peak at *m/z* 453; this $[M + H + 17]^+$ feature corresponds to an adduct of protonated Rivaroxaban with ammonia.

The two ion populations observed in the N_2 environment were studied with CID and UVPD to determine the associated isomer structures. The UVPD action spectra and CID spectra acquired for each mobility- and mass-selected ion population are provided in Figure C- 3. Both ion populations showed the same CID fragmentation products consistent with previous work on Rivaroxaban (see Appendix C Table C- 2 and Figure C- 4 for product ion assignment).[179] These same major product channels were also observed via UVPD. Moreover, breakdown curves (see Appendix C Figure C- 5) and UVPD action spectra observed for both ion populations were similar, indicating that both populations were associated with the same geometric isomer. In comparing the UVPD and CID results, we find that the product ions exhibited different abundances (see Appendix C Figure C- 3); the *m/z* 145 fragment was the most abundant product formed via CID, whereas UVPD predominantly produced the *m/z* 231 species. Differences in product ion abundances for CID compared to UVPD are not unexpected given that CID occurs on the ground state electronic potential energy surface (PES) whereas UVPD occurs on (or via) an excited state PES.[90] In examining the UVPD spectra as observed in each of the individual product channels (see Appendix C Figure C- 6), we find that the *m/z* 231, 318, and 392 products exhibit similar UVPD spectra, but that the spectrum for the *m/z* 145 fragment is somewhat different in the short-wavelength region. This suggests that the *m/z* 145 product may be produced via a different photodissociative pathway than the other fragments.

5.3.2 Acetonitrile-Modified Environment

The DMS behavior of protonated Rivaroxaban was also investigated in an acetonitrile (MeCN)-modified environment to explore the impact of solvent vapor on separation and

ion populations. The dispersion plots recorded for the MeCN-modified conditions are shown in Figure 5-3A. Two ion populations are observed, one that exhibits Type A behavior and another that exhibits Type B behaviour at T= 150 °C. As was observed in the N_2 environment, the ionogram peak intensities change with carrier gas temperature; with increasing temperature, the Type B feature increases in intensity, and the intensity of the Type A feature diminishes. This result suggests that the Type A ion population is associated with fragmentation of a larger Rivaroxaban-containing cluster. The temperature dependence of the Type B feature is more interesting. As the gas temperature is increased to T = 300 °C, the dispersion curve evolves from Type B to Type C to the exotic type D behavior wherein at high SV values the optimal CV reaches a maximum then begins to decrease.[62,68] Type D behavior is generally attributed to strongly-bound ion-solvent clusters, in this case $[M + H + MeCN]^+$, which undergo field-induced dissociation at high SV values and adopt Type A behavior as the bare ion.

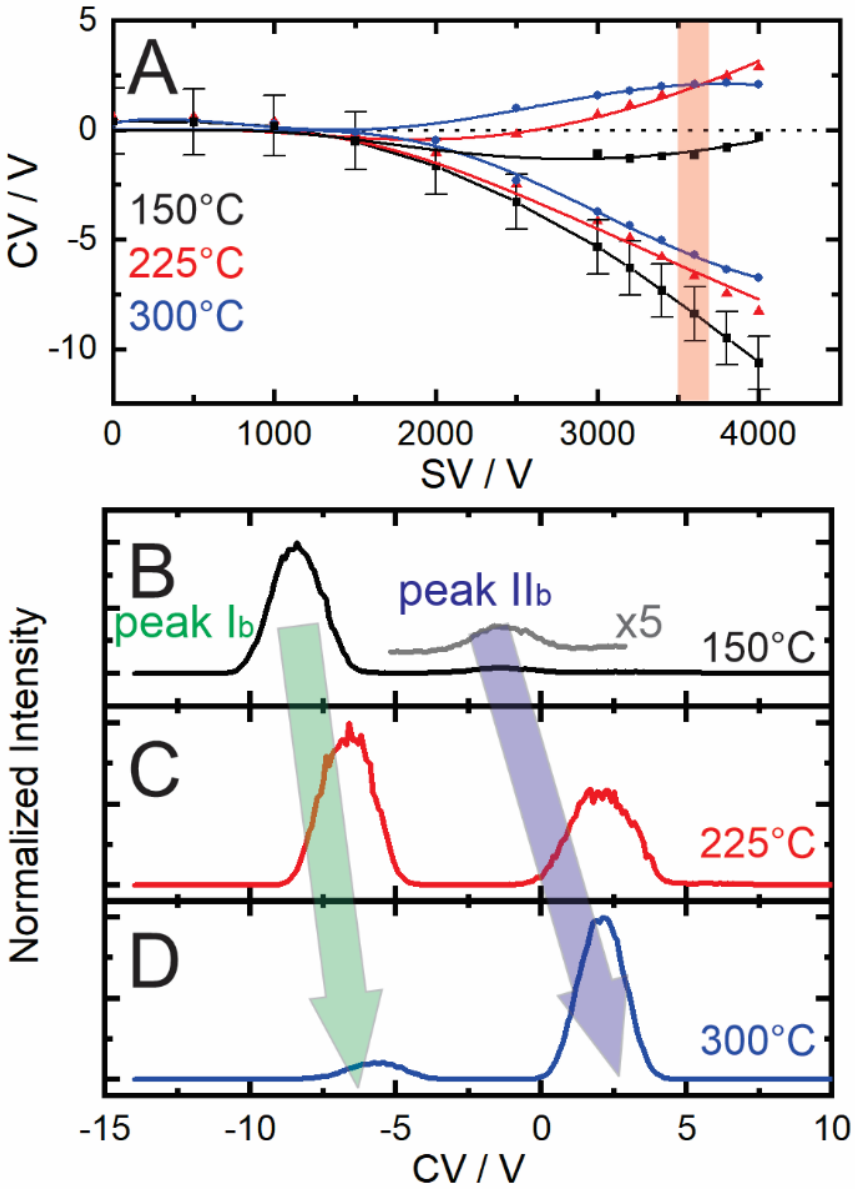

Figure 5-3. (A) Dispersion plots of Rivaroxaban observed in a MeCN-modified environment at three different DMS temperatures (T = 150, 225, 300 °C). Representative error bars shown for the dispersion curve at T = 150 °C plot the full width half maximum of the Gaussian curve fit to the ionogram plot. The ionograms for the region highlighted with the vertical green bar are shown in panels (B) T = 150 °C, (C) T = 225 °C, and (D) T = 300 °C.

Precursor ion scans of the two ionogram peaks show that the feature at CV ≈ −8 V (Peak I_b; Figure 5-3B-D) corresponds to the ammonia adduct, $[M + H + 17]^+$ (see Appendix C Figure C- 1). In contrast, precursor ion scans of the feature at CV ≈ −2 V (Peak II_b; Figure 5-3B-D) did not show significant *m/z* peaks larger than that of the parent.

However, closer inspection of the minor peaks in the precursor ion scan (Appendix C Figure C- 1) shows a feature at *m/z* 477 corresponding to $[M + H + 41]^+$ (*i.e.*, MeCN adduct) and another at *m/z* 494 corresponding to $[M + H + 58]^+$ (*i.e.*, ammonia + MeCN cluster), confirming the presence of a protonated Rivaroxaban and acetonitrile cluster. Consequently, we expect that the ion-solvent clusters associated with Peak II_b must dissociate to yield the bare protonated parent between the DMS cell and the first quadrupole mass filter. CID of both ion populations showed the same product ions as were observed for the experiments conducted in the pure N_2 environment (see Figure 5-4C and D), however, the slopes of breakdown curves for the two ion populations were somewhat different (see Figure C- 5). Interestingly, the UVPD action spectra recorded for the two ion populations are significantly different (see Figure 5-4A and B). The UVPD spectrum observed when gating on the species eluting at Peak I_b is essentially the same as was observed for both ion populations separated in the N_2 environment. In contrast, the UVPD spectrum observed for the Peak II_b ion population exhibits substantially more intensity and band structure at short wavelength. The UVPD spectra observed via each individual product channel are plotted in Appendix C Figure C- 7.

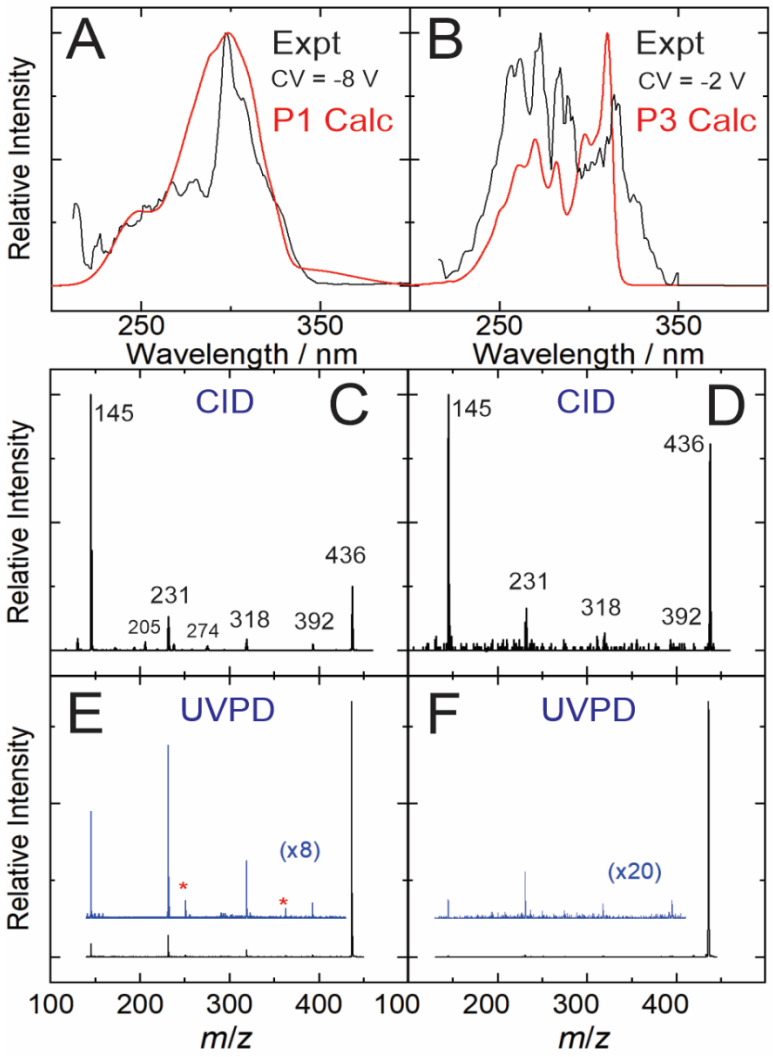

Figure 5-4. The UVPD action spectra of the Rivaroxaban ion populations isolated at (A) SV = 3600 V and CV = –8 V and (B) SV = 3600 V and CV = –2 V in the MeCN-modified environment. Overlayed in red are the computed vibronic spectra of tautomers P1 and P3 (see Figure 5). The CID mass spectra observed when gating on the ion population at (C) SV = 3600 V and CV = –8 V and (D) SV = 3600 V and CV = –2 V in the MeCN-modified environment. The UVPD mass spectra observed when gating on the ion population at (E) SV = 3600 V and CV = –8 V and (F) SV = 3600 V and CV = –2 V in the MeCN-modified environment. Peaks marked with a red asterisk are assigned to background ions.

Both ion populations observed in the MeCN-modified environment yield the same major product channels (albeit with different relative intensities) as the ion populations observed in N_2. However, close examination of Figure 5-4C and Figure 5-4D, as well as Figure 5-4E and Figure 5-4F, reveals differences in fragmentation efficiencies for the two ion populations. Via both CID and UVPD, the ion population of Peak I_b exhibits a

significantly higher fragmentation efficiency. Additional minor product ions are observed at *m/z* 205, 237, and 274 in Figure 5-4C (Appendix C Figure C- 4 for assignment). These ions are not observed in Figure 5-3D owing to the lower signal-to-noise associated with peak II_b. When considered collectively with the measured UVPD action spectra, we find the ion population associated with peak II_b is of a different tautomeric form than that observed for the other three ionogram peaks. In other words, UVPD clearly distinguishes geometric isomers that are indistinguishable by CID. It is not clear why the ions of peak II_b in the MeCN-modified environment should adopt a different geometry than those associated with the other ion populations studied. One possibility is that the ion is preferentially solvated by MeCN in the modified environment.[94] Ion-solvent clustering would serve to both reduce the effective temperature of the analyte and, because MeCN is aprotic, prevent tautomer interconversion via proton shuttling.[180] To rationalize experimental observations and identify which tautomers are responsible for the observed UVPD action spectra, a computational study was conducted.

5.3.3 Computed Structures and Vibronic Spectra

The three most energetically favorable tautomers of protonated Rivaroxaban are shown in Figure 5-5. Several additional higher energy species were found computationally but were discounted based on their relative energies. For the low-energy species shown in Figure 5-5, protonation occurs at the carbonyl oxygen atoms. In two cases, molecular energy is further reduced by adopting conformations wherein the charge-carrying proton is shared between two basic sites.

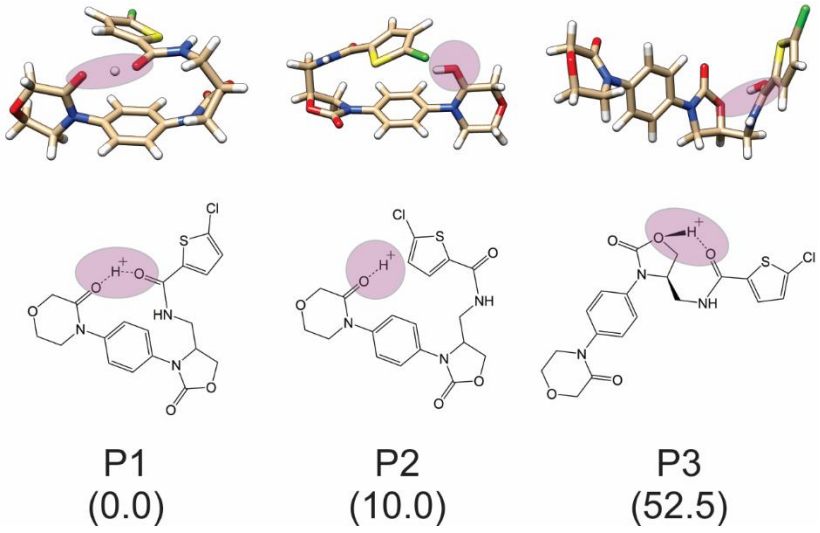

Figure 5-5. The optimized geometries of the three most energetically favorable protonated Rivaroxaban tautomers. Relative standard Gibbs energies (kJ mol-1) of the gas-phase species at standard temperature and pressure are given in parentheses.

The calculated relative energies and predicted Boltzmann populations of the three lowest energy tautomers are given in Table 1. Based on the relative energies, one would expect tautomer 1 (P1) to be the dominant contributor to the ensemble population. Based on this, we hypothesized that the dominant species observed in three of the four ion populations studied experimentally should be P1. The fact that a different tautomer is observed at peak II_b in the MeCN-modified environment is unexpected given the gas-phase ion calculations; assuming a Boltzmann distribution, one would expect that P2 should account for 2% of the population and that the P3 population should be negligible. To test whether the gas-phase ion populations were instead reflective of the solvation environment, relative tautomer energies were recalculated using MeCN and MeOH polarizable continuum models (PCMs). Doing so substantially lowered the energies of P2 and P3 relative to the global minimum. In the case of a MeOH solution environment, the Boltzmann populations of P1 and P2 are essentially equal, whereas for MeCN solution conditions, P2 becomes the dominant species in the ensemble. As was the case in the gas phase, the Boltzmann population of P3 is negligible in both solution phase environments,

Table 1. Calculated relative Gibbs energies (kJ mol^{-1}) and relative populations of protonated Rivaroxaban tautomers at P = 1 atm and T = 25 °C. Polarizable continuum models (PCMs) for MeOH and MeCN were employed to model condensed-phase conditions.

Condition	Tautomer		
	P1	P2	P3
Gas Phase			
Relative Energy	0.0	10.0	52.5
Population (%)	98	2	6×10^{-8}
MeCN PCM			
Relative Energy	12.1	0.0	19.7
Population (%)	1	99	3×10^{-2}
MeOH PCM			
Relative Energy	0.8	0.0	25.2
Population (%)	42	58	2×10^{-3}

To resolve the ambiguity as to which species are the spectral carriers, vertical gradient Franck-Condon simulations of the tautomer vibronic spectra were undertaken. The calculated spectrum of P1 agrees well with the experimental UVPD action spectra recorded in the pure N_2 environment and when gating on the CV ≈ –8 V ionogram peak in the MeCN-modified environment. These observations support our hypothesis that P1 is the global minimum structure and is typically the spectral carrier in our experiments. Interestingly, the computed spectrum of P3 best matched the experimental spectrum of the CV ≈ –2 V population in the MeCN-modified environment. The computed spectrum of P2 did not agree with the experimental spectra (see Appendix C Figure C- 8). Given the structural similarity between P1 and P2 (see Figure 5-5), we propose that P2 can easily convert to the more energetically stable P1 structure via dihedral rotation of the bond between the amide and azole moieties. Transition state calculations support this proposition (see Appendix C Figure C- 9 for the optimized transition state geometry); the barrier for converting P2 to P1 is82stimateed to be ≈13 kJ mol^{-1}. Given this relatively labile interconversion and the agreement between measured and calculated spectra, we conclude that tautomer associated with Peak II_b of the MeCN-modified environment is P3.

More detailed consideration of the computational results reveals which vibronic transitions are observed experimentally. The seven lowest energy electronic transitions were calculated for each of P1, P2 and P3. These spectra are available in the supporting

information Appendix C Figure C- 10. The P1 spectrum is dominated by the $S_0 \rightarrow S_2$ band at $\lambda \approx 300$ nm. The small shoulder to the short wavelength side of the $S_0 \rightarrow S_2$ band corresponds to the $S_0 \rightarrow S_6$ band. In the case of P3, the $S_0 \rightarrow S_3$ and $S_0 \rightarrow S_5$ band systems dominate the computed spectrum. Differences between the observed and calculated spectra can be attributed to the accuracy of the calculations and the fact that the intensities of UVPD action spectra depend on the absorption cross section of the transition and the efficiency of coupling to a dissociative channel, the latter of which is not computed in VG|FC calculations.

Figure 5-6 plots the natural transition orbitals (NTOs) associated with the most intense vibronic transitions as calculated by VG|FC (see Appendix C Figure C- 10 for relative intensities of the individual electronic transitions). NTO analysis of electronic transitions allows for the visualization of the molecular orbitals (MOs) participating in the excitation processes.[150] The $S_0 \rightarrow S_2$ transition of P1 is a $\pi \rightarrow \pi^*$ transition predominantly associated with the thiophene and amide moieties. Note, however, that calculations indicate a small degree of charge transfer from the phenyl ring to the thiophene-centered π^* orbital. A similar thiophene-centered $\pi \rightarrow \pi^*$ excitation is associated with the $S_0 \rightarrow S_3$ transition of P3, but in this case calculations do not show a charge-transfer component. In contrast, the $S_0 \rightarrow S_5$ transition of P3 is associated with a $\pi \rightarrow \pi^*$ excitation that promotes electron density from the phenyl and azole moieties to the thiophene and amide moieties. This excitation effectively creates a tethered excited charge-transfer complex (ECT).[181] The significant differences in excited state character between P1 and P3 might result in the observed differences with regard to fragmentation efficiency. To explore this possibility, a more detailed computational investigation of the excited state dynamics of protonated Rivaroxaban is warranted.

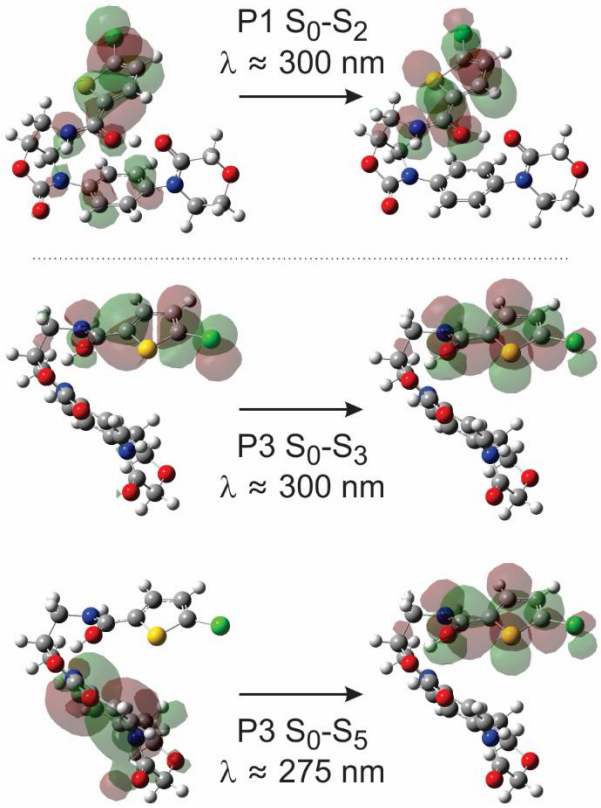

Figure 5-6. The natural transition orbitals (NTOs) associated with the (top) $S_0 \rightarrow S_2$ transition of P1, (middle) the $S_0 \rightarrow S_3$ transition of P3, and (bottom) $S_0 \rightarrow S_5$ transition of P3.

5.4. Conclusions

Differential mobility spectrometry of protonated Rivaroxaban yields two ion populations in a pure N_2 environment. Mass spectrometric analysis shows that one of the ion populations is associated with transmission of the bare parent ion and the other with fragmentation of Rivaroxaban-ammonium adducts prior to mass-selection. Collision-induced dissociation, analyte breakdown curves, and UVPD action spectroscopy all indicate that the protonated Rivaroxaban moiety that is liberated from the ammonium adduct adopts the same global minimum geometry as members of the bare ion ensemble. Vertical gradient Franck Condon simulations and natural transition orbital calculations show that the $S_0 \rightarrow S_2$ transition of P1, which dominates the UV spectrum of that prototropic isomer, is associated with a $\pi \rightarrow \pi^*$ transition localized on the thiophene and amide groups.

When conducting similar experiments in a MeCN-modified environment, the DMS ionogram of protonated Rivaroxaban also yields two peaks. In this case, one of the ion populations is associated with fragmentation of Rivaroxaban-ammonium adducts and the other with fragmentation of Rivaroxaban-MeCN clusters prior to mass-selection. When fixing the DMS settings to select these ion populations, the same product ions are detected as were observed for the pure N_2 environment. However, the protonated Rivaroxaban moieties that are liberated from the MeCN-containing ion-solvent clusters exhibit slight differences in their fragmentation efficiencies and breakdown curves when compared to the other ensembles. Moreover, UVPD action spectroscopy yields a significantly different electronic spectrum for this population of ions. Based on computational results, we expect that dissociation of the MeCN-containing ion-solvent clusters yields the P3 tautomer of protonated Rivaroxaban. We speculate that that P3 is kinetically trapped during the ESI process and is stabilized in the MeCN-modified environment, possibly by preferential solvation and the cooling effect imparted by dynamic ion-solvent clustering. Vertical gradient Franck Condon simulations and natural transition orbital calculations for P3 show that the $S_0 \rightarrow S_3$ and $S_0 \rightarrow S_5$ transitions are responsible for the observed UV spectrum. The differences in electronic excitation and subsequent excited state dynamics between P1 and P3 might account for the observed differences in fragmentation efficiency. A detailed computational study of the excited state molecular dynamics would be a valuable contribution towards understanding the observed photophysical behavior of protonated Rivaroxaban.

The stabilization of higher energy isomers in the MeCN-modified environment may have some bearing on LC-MS workflows wherein MeCN/H_2O gradients are commonly employed. In cases of targeted analysis, quantification relies on multiple reaction monitoring via known fragmentation transitions. Should it be the case that elution occurs during an MeCN-rich retention time, and that a higher energy isomer be kinetically trapped and stabilized by the MeCN vapor, it is possible that MRM transitions could be artificially diminished or enhanced, thus leading to incorrect quantitation results. Whether the results

of this study can be extended more generally to other pharmaceuticals (or other analytes) is currently an open question.

Chapter 6: Conclusions and Future Outlook

Differential mobility spectrometry coupled with UVPD was employed to analyze several isomer pairs in the gas phase. DMS and UVPD analysis allowed for the rapid separation of isomers while also providing valuable information on the physicochemical properties of the analytes. The incorporation of DMS and UVPD prior to MS offered thorough investigations of the functional, geometric, and electronic properties of ions. While the clustering behaviour provided information on the functional and geometric differences between ions, the vibronic structure of ions was probed using UVPD. The action spectra acquired led to a fingerprinting technique for identifying isomers and their determining their structures in the gas phase. Although MS is commonly selected as the preferred technique for rapidly identifying ions in samples, DMS and UVPD analyses offered significant improvements to the method to tackle indistinguishable isomers.

The studies presented in this thesis highlighted the ability to exploit subtle differences in structure to promote drastically different behavior in the DMS. DMS utilizes significantly different instrumentation and methodology compared to other IMS techniques. While most IMS instruments rely on the separation of isomers based on their CCS, this is not the case for DMS, due the incorporation of an alternating high and low electric field. The setup of the DMS may at times present a hindrance when separating isomers based on their CCSs alone, as the differential mobility of an ion may not directly correlate with the ion CCS. However, the versatility in conditions that can be altered for

separation, such as the inclusion of solvent modifiers or gas mixtures, allows ions to be separated by alternative means.

The studies presented delved into the effects of ESI parameters on the separation of analytes using DMS. In Chapters 3 and 5, ESI-formed ion-solvent adducts lead to the formation of several DMS-separated ion species. The separation of differently clustered species of the same analyte interferes with the process of separating isomers. However, the careful selection of ESI solvent composition and other ESI parameters can aid in the preservation and observation of conformers, as was seen in Chapter 5. It is thus concluded that both ESI and DMS parameters must be optimized in tandem with one another to promote the desired effects.

The incorporation of UVPD analyses in Chapters 4 and 5 highlighted the benefits of the hybrid DMS-MS-UVPD setup. With isomers separated in DMS and selected by MS, UVPD provided conclusive identification of isomers. This benefit was especially noted in the separation of prototropic isomers of Rivaroxaban. UVPD analysis was not only able to identify the location of the protonation site, but it was also complemented with computational studies that allowed identification of the structures of each of the separated populations.

When adopting lessons learned in this thesis to other analytes, it is important to also consider the limitations of the setup discussed. Given the coarse nature of the DMS, with the inclusion of the high electric field, field-induced heating must be considered. This is especially important in the case of relatively small ions that are prone to fragmentation upon exposure to high electric fields. Additionally, conformer studies using the DMS must consider any field-induced unfolding to ensure accurate measurements of gas-phase conformations. Thus, method optimizations are required for isomer studies of ions prone to changes upon introduction of a high field. While the addition of solvent modifier could help mitigate these shortcomings, it may be of interest to consider the introduction of gas mixtures. Additionally, while DMS has been proven successful in the separation of isomer

species, it could be of interest to introduce liquid chromatography prior to DMS for better analysis of complex mixtures, such as biological samples.

The exploration of selective dissociation of UVPD could be of interest for the rapid identification of isomers, when developing rapid separation and identification techniques. It would be of interest to explore anionic isomers, as they present opportunities to investigate electron detachment. Action spectroscopy of this type could provide further information on the behaviour of anions, making the instrumental setup a powerful tool in the characterization of ions.

Overall, the investigation of biologically relevant isomers using DMS-MS coupled with UVPD has proven successful. The instrumental setup offers various ways of separating and identifying isomers and offers even more opportunities for modification to improve its application and performance. Incorporating DMS and UVPD into mass spectrometry greatly improves the characterization and separation capacity of this rapid gas-phase analytical tool.

References

(1) K. Trivedi, D.; A. Hollywood, K.; Goodacre, R. Metabolomics for the Masses: The Future of Metabolomics in a Personalized World. *Eur. J. Mol. Clin. Med.* 2017, *3* (6), 294. https://doi.org/10.1016/j.nhtm.2017.06.001.

(2) Monika; Verma, A.; Tiwari, M. K.; Show, B.; Saha, S. Modulation of Weak Interactions in Structural Isomers: Positional Isomeric Effects on Crystal Packing and Physical Properties and Solid-State Thin-Film Fabrication. *ACS Omega* 2020, *5* (1), 448–459. https://doi.org/10.1021/acsomega.9b02962.

(3) Chhabra, N.; Aseri, M.; Padmanabhan, D. A Review of Drug Isomerism and Its Significance. *Int. J. Appl. Basic Med. Res.* 2013, *3* (1), 16. https://doi.org/10.4103/2229-516X.112233.

(4) Morales, P.; Reggio, P. H.; Jagerovic, N. An Overview on Medicinal Chemistry of Synthetic and Natural Derivatives of Cannabidiol. *Front. Pharmacol.* 2017, *8*, 422. https://doi.org/10.3389/fphar.2017.00422.

(5) Sun, P. D.; Foster, C. E.; Boyington, J. C. Overview of Protein Structural and Functional Folds. *Curr. Protoc. Protein Sci.* 2004, *35* (1). https://doi.org/10.1002/0471140864.ps1701s35.

(6) Makola, M. M.; Dubery, I. A.; Koorsen, G.; Steenkamp, P. A.; Kabanda, M. M.; du Preez, L. L.; Madala, N. E. The Effect of Geometrical Isomerism of 3,5-Dicaffeoylquinic Acid on Its Binding Affinity to HIV-Integrase Enzyme: A Molecular Docking Study. *Evid. Based Complement. Alternat. Med.* 2016, *2016*, 1–9. https://doi.org/10.1155/2016/4138263.

(7) Das, J.; Rao, C. V. L.; Sastry, T. V. R. S.; Roshaiah, M.; Sankar, P. G.; Khadeer, A.; Kumar, M. S.; Mallik, A.; Selvakumar, N.; Iqbal, J.; Trehan, S. Effects of Positional and Geometrical Isomerism on the Biological Activity of Some Novel Oxazolidinones. *Bioorg. Med. Chem. Lett.* 2005, *15* (2), 337–343. https://doi.org/10.1016/j.bmcl.2004.10.073.

(8) Srivastava, R. The Role of Proton Transfer on Mutations. *Front. Chem.* 2019, *7*, 536. https://doi.org/10.3389/fchem.2019.00536.

(9) Fedeles, B. I.; Li, D.; Singh, V. Structural Insights Into Tautomeric Dynamics in Nucleic Acids and in Antiviral Nucleoside Analogs. *Front. Mol. Biosci.* 2022, *8*, 823253. https://doi.org/10.3389/fmolb.2021.823253.

(10) Gowda, G. N.; Zhang, S.; Gu, H.; Asiago, V.; Shanaiah, N.; Raftery, D. Metabolomics-Based Methods for Early Disease Diagnostics. *Expert Rev. Mol. Diagn.* 2008, *8* (5), 617–633. https://doi.org/10.1586/14737159.8.5.617.

(11) Chew, H.; Solomon, V. A.; Fonteh, A. N. Involvement of Lipids in Alzheimer's Disease Pathology and Potential Therapies. *Front. Physiol.* 2020, *11*, 598. https://doi.org/10.3389/fphys.2020.00598.

(12) Harris, W. S.; Mozaffarian, D.; Rimm, E.; Kris-Etherton, P.; Rudel, L. L.; Appel, L. J.; Engler, M. M.; Engler, M. B.; Sacks, F. Omega-6 Fatty Acids and Risk for Cardiovascular Disease: A Science Advisory From the American Heart Association Nutrition Subcommittee of the Council on Nutrition, Physical Activity, and Metabolism; Council on Cardiovascular Nursing; and Council on Epidemiology and Prevention. *Circulation* 2009, *119* (6), 902–907. https://doi.org/10.1161/CIRCULATIONAHA.108.191627.
(13) Glish, G. L.; Vachet, R. W. The Basics of Mass Spectrometry in the Twenty-First Century. *Nat. Rev. Drug Discov.* 2003, *2* (2), 140–150. https://doi.org/10.1038/nrd1011.
(14) Miller, P. E.; Denton, M. B. The Quadrupole Mass Filter: Basic Operating Concepts. *J. Chem. Educ.* 1986, *63* (7), 617. https://doi.org/10.1021/ed063p617.
(15) Boesl, U. Time-of-Flight Mass Spectrometry: Introduction to the Basics: TIME-OF-FLIGHT MASS SPECTROMETRY. *Mass Spectrom. Rev.* 2017, *36* (1), 86–109. https://doi.org/10.1002/mas.21520.
(16) Zubarev, R. A.; Makarov, A. Orbitrap Mass Spectrometry. *Anal. Chem.* 2013, *85* (11), 5288–5296. https://doi.org/10.1021/ac4001223.
(17) Crotti, S.; Menicatti, M.; Pallecchi, M.; Bartolucci, G. Tandem Mass Spectrometry Approaches for Recognition of Isomeric Compounds Mixtures. *Mass Spectrom. Rev.* 2021. https://doi.org/10.1002/mas.21757.
(18) Harvey, S. R.; Seffernick, J. T.; Quintyn, R. S.; Song, Y.; Ju, Y.; Yan, J.; Sahasrabuddhe, A. N.; Norris, A.; Zhou, M.; Behrman, E. J.; Lindert, S.; Wysocki, V. H. Relative Interfacial Cleavage Energetics of Protein Complexes Revealed by Surface Collisions. *Proc. Natl. Acad. Sci.* 2019, *116* (17), 8143–8148. https://doi.org/10.1073/pnas.1817632116.
(19) Stiving, A. Q.; VanAernum, Z. L.; Busch, F.; Harvey, S. R.; Sarni, S. H.; Wysocki, V. H. Surface-Induced Dissociation: An Effective Method for Characterization of Protein Quaternary Structure. *Anal. Chem.* 2019, *91* (1), 190–209. https://doi.org/10.1021/acs.analchem.8b05071.
(20) Asakawa, D.; De Pauw, E. Difference of Electron Capture and Transfer Dissociation Mass Spectrometry on Ni^{2+} -, Cu^{2+} -, and Zn^{2+} -Polyhistidine Complexes in the Absence of Remote Protons. *J. Am. Soc. Mass Spectrom.* 2016, *27* (7), 1165–1175. https://doi.org/10.1007/s13361-016-1395-z.
(21) Pitt, J. J. Principles and Applications of Liquid Chromatography- Mass Spectrometry in Clinical Biochemistry. *Liq. Chromatogr.* 16.
(22) Zhang, T.; Watson, D. G. A Short Review of Applications of Liquid Chromatography Mass Spectrometry Based Metabolomics Techniques to the Analysis of Human Urine. *The Analyst* 2015, *140* (9), 2907–2915. https://doi.org/10.1039/C4AN02294G.
(23) Zoccali, M.; Tranchida, P. Q.; Mondello, L. Fast Gas Chromatography-Mass Spectrometry: A Review of the Last Decade. *TrAC Trends Anal. Chem.* 2019, *118*, 444–452. https://doi.org/10.1016/j.trac.2019.06.006.
(24) Schneider, B. B.; Covey, T. R.; Coy, S. L.; Krylov, E. V.; Nazarov, E. G. Planar Differential Mobility Spectrometer as a Pre-Filter for Atmospheric Pressure Ionization Mass

Spectrometry. *Int. J. Mass Spectrom.* 2010, *298* (1–3), 45–54. https://doi.org/10.1016/j.ijms.2010.01.006.
(25) Campbell, J. L.; Le Blanc, J. Y.; Kibbey, R. G. Differential Mobility Spectrometry: A Valuable Technology for Analyzing Challenging Biological Samples. *Bioanalysis* 2015, *7* (7), 853–856. https://doi.org/10.4155/bio.15.14.
(26) Hopkins, W. S. Dynamic Clustering and Ion Microsolvation. In *Comprehensive Analytical Chemistry*; Elsevier, 2019; Vol. 83, pp 83–122. https://doi.org/10.1016/bs.coac.2018.10.002.
(27) Liu, C.; Le Blanc, J. C. Y.; Schneider, B. B.; Shields, J.; Federico, J. J.; Zhang, H.; Stroh, J. G.; Kauffman, G. W.; Kung, D. W.; Ieritano, C.; Shepherdson, E.; Verbuyst, M.; Melo, L.; Hasan, M.; Naser, D.; Janiszewski, J. S.; Hopkins, W. S.; Campbell, J. L. Assessing Physicochemical Properties of Drug Molecules via Microsolvation Measurements with Differential Mobility Spectrometry. *ACS Cent. Sci.* 2017, *3* (2), 101–109. https://doi.org/10.1021/acscentsci.6b00297.
(28) Campbell, J. L.; Le Blanc, J. C. Y.; Schneider, B. B. Probing Electrospray Ionization Dynamics Using Differential Mobility Spectrometry: The Curious Case of 4-Aminobenzoic Acid. *Anal. Chem.* 2012, *84* (18), 7857–7864. https://doi.org/10.1021/ac301529w.
(29) Ieritano, C.; Rickert, D.; Featherstone, J.; Honek, J. F.; Campbell, J. L.; Blanc, J. C. Y. L.; Schneider, B. B.; Hopkins, W. S. The Charge-State and Structural Stability of Peptides Conferred by Microsolvating Environments in Differential Mobility Spectrometry. *J. Am. Soc. Mass Spectrom.* 2021, *32* (4), 956–968. https://doi.org/10.1021/jasms.0c00469.
(30) Medhe, S. Ionization Techniques in Mass Spectrometry: A Review. *Mass Spectrom. Purif. Tech.* 2018, *04* (01). https://doi.org/10.4172/2469-9861.1000126.
(31) Awad, H.; Khamis, M. M.; El-Aneed, A. Mass Spectrometry, Review of the Basics: Ionization. *Appl. Spectrosc. Rev.* 2015, *50* (2), 158–175. https://doi.org/10.1080/05704928.2014.954046.
(32) Vikse, K. L.; Scott McIndoe, J. Ionization Methods for the Mass Spectrometry of Organometallic Compounds. *J. Mass Spectrom.* 2018, *53* (10), 1026–1034. https://doi.org/10.1002/jms.4286.
(33) Ryan, D. J.; Spraggins, J. M.; Caprioli, R. M. Protein Identification Strategies in MALDI Imaging Mass Spectrometry: A Brief Review. *Curr. Opin. Chem. Biol.* 2019, *48*, 64–72. https://doi.org/10.1016/j.cbpa.2018.10.023.
(34) Ho, C.; Lam, C.; Chan, M.; Cheung, R.; Law, L.; Lit, L.; Ng, K.; Suen, M.; Tai, H. Electrospray Ionisation Mass Spectrometry: Principles and Clinical Applications. 10.
(35) Rayleigh, Lord. XX. *On the Equilibrium of Liquid Conducting Masses Charged with Electricity*. *Lond. Edinb. Dublin Philos. Mag. J. Sci.* 1882, *14* (87), 184–186. https://doi.org/10.1080/14786448208628425.

(36) Konermann, L.; Ahadi, E.; Rodriguez, A. D.; Vahidi, S. Unraveling the Mechanism of Electrospray Ionization. *Anal. Chem.* 2013, *85* (1), 2–9. https://doi.org/10.1021/ac302789c.
(37) Konermann, L.; Metwally, H.; Duez, Q.; Peters, I. Charging and Supercharging of Proteins for Mass Spectrometry: Recent Insights into the Mechanisms of Electrospray Ionization. *The Analyst* 2019, *144* (21), 6157–6171. https://doi.org/10.1039/C9AN01201J.
(38) Attygalle, A. B.; Xia, H.; Pavlov, J. Influence of Ionization Source Conditions on the Gas-Phase Protomer Distribution of Anilinium and Related Cations. *J. Am. Soc. Mass Spectrom.* 2017, *28* (8), 1575–1586. https://doi.org/10.1007/s13361-017-1640-0.
(39) Xia, H.; Attygalle, A. B. Transformation of the Gas-Phase Favored *O* -Protomer of *p* -Aminobenzoic Acid to Its Unfavored *N* -Protomer by Ion Activation in the Presence of Water Vapor: An Ion-Mobility Mass Spectrometry Study. *J. Mass Spectrom.* 2018, *53* (4), 353–360. https://doi.org/10.1002/jms.4066.
(40) Walker, S. W. C.; Mark, A.; Verbuyst, B.; Bogdanov, B.; Campbell, J. L.; Hopkins, W. S. Characterizing the Tautomers of Protonated Aniline Using Differential Mobility Spectrometry and Mass Spectrometry. *J. Phys. Chem. A* 2018, *122* (15), 3858–3865. https://doi.org/10.1021/acs.jpca.7b10872.
(41) Kruve, A.; Kaupmees, K. Adduct Formation in ESI/MS by Mobile Phase Additives. *J. Am. Soc. Mass Spectrom.* 2017, *28* (5), 887–894. https://doi.org/10.1007/s13361-017-1626-y.
(42) Banerjee, S.; Mazumdar, S. Electrospray Ionization Mass Spectrometry: A Technique to Access the Information beyond the Molecular Weight of the Analyte. *Int. J. Anal. Chem.* 2012, *2012*, 1–40. https://doi.org/10.1155/2012/282574.
(43) Konermann, L.; Pan, J.; Wilson, D. J. Protein Folding Mechanisms Studied by Time-Resolved Electrospray Mass Spectrometry. *BioTechniques* 2006, *40* (2), 135–141. https://doi.org/10.2144/06402TE01.
(44) McCabe, J. W.; Shirzadeh, M.; Walker, T. E.; Lin, C.-W.; Jones, B. J.; Wysocki, V. H.; Barondeau, D. P.; Clemmer, D. E.; Laganowsky, A.; Russell, D. H. Variable-Temperature Electrospray Ionization for Temperature-Dependent Folding/Refolding Reactions of Proteins and Ligand Binding. *Anal. Chem.* 2021, *93* (18), 6924–6931. https://doi.org/10.1021/acs.analchem.1c00870.
(45) Woodall, D. W.; El-Baba, T. J.; Fuller, D. R.; Liu, W.; Brown, C. J.; Laganowsky, A.; Russell, D. H.; Clemmer, D. E. Variable-Temperature ESI-IMS-MS Analysis of Myohemerythrin Reveals Ligand Losses, Unfolding, and a Non-Native Disulfide Bond. *Anal. Chem.* 2019, *91* (10), 6808–6814. https://doi.org/10.1021/acs.analchem.9b00981.
(46) Dodds, J. N.; Baker, E. S. Ion Mobility Spectrometry: Fundamental Concepts, Instrumentation, Applications, and the Road Ahead. *J. Am. Soc. Mass Spectrom.* 2019, *30* (11), 2185–2195. https://doi.org/10.1007/s13361-019-02288-2.
(47) Mason, E. A.; McDaniel, E. W. *Transport Properties of Ions in Gases*; Wiley, 1988.

(48) Wyttenbach, T.; Bleiholder, C.; Bowers, M. T. Factors Contributing to the Collision Cross Section of Polyatomic Ions in the Kilodalton to Gigadalton Range: Application to Ion Mobility Measurements. *Anal. Chem.* 2013, *85* (4), 2191–2199. https://doi.org/10.1021/ac3029008.

(49) Prell, J. S. Modelling Collisional Cross Sections. In *Comprehensive Analytical Chemistry*; Elsevier, 2019; Vol. 83, pp 1–22.

(50) Ewing, S. A.; Donor, M. T.; Wilson, J. W.; Prell, J. S. Collidoscope: An Improved Tool for Computing Collisional Cross-Sections with the Trajectory Method. *J. Am. Soc. Mass Spectrom.* 2017, *28* (4), 587–596. https://doi.org/10.1007/s13361-017-1594-2.

(51) Gabelica, V.; Shvartsburg, A. A.; Afonso, C.; Barran, P.; Benesch, J. L. P.; Bleiholder, C.; Bowers, M. T.; Bilbao, A.; Bush, M. F.; Campbell, J. L.; Campuzano, I. D. G.; Causon, T.; Clowers, B. H.; Creaser, C. S.; De Pauw, E.; Far, J.; Fernandez-Lima, F.; Fjeldsted, J. C.; Giles, K.; Groessl, M.; Hogan, C. J.; Hann, S.; Kim, H. I.; Kurulugama, R. T.; May, J. C.; McLean, J. A.; Pagel, K.; Richardson, K.; Ridgeway, M. E.; Rosu, F.; Sobott, F.; Thalassinos, K.; Valentine, S. J.; Wyttenbach, T. Recommendations for Reporting Ion Mobility Mass Spectrometry Measurements. *Mass Spectrom. Rev.* 2019, *38* (3), 291–320. https://doi.org/10.1002/mas.21585.

(52) Zheng, X.; Aly, N. A.; Zhou, Y.; Dupuis, K. T.; Bilbao, A.; Paurus, V. L.; Orton, D. J.; Wilson, R.; Payne, S. H.; Smith, R. D.; Baker, E. S. A Structural Examination and Collision Cross Section Database for over 500 Metabolites and Xenobiotics Using Drift Tube Ion Mobility Spectrometry. *Chem Sci* 2017, *8* (11), 7724–7736. https://doi.org/10.1039/C7SC03464D.

(53) Shvartsburg, A. A.; Ibrahim, Y. M.; Smith, R. D. Differential Ion Mobility Separations in up to 100 % Helium Using Microchips. *J. Am. Soc. Mass Spectrom.* 2014, *25* (3), 480–489. https://doi.org/10.1007/s13361-013-0797-4.

(54) Liu, F. C.; Ridgeway, M. E.; Park, M. A.; Bleiholder, C. Tandem-Trapped Ion Mobility Spectrometry/Mass Spectrometry (*t* TIMS/MS): A Promising Analytical Method for Investigating Heterogenous Samples. *The Analyst* 2022, *147* (11), 2317–2337. https://doi.org/10.1039/D2AN00335J.

(55) Hernandez, D. R.; DeBord, J. D.; Ridgeway, M. E.; Kaplan, D. A.; Park, M. A.; Fernandez-Lima, F. Ion Dynamics in a Trapped Ion Mobility Spectrometer. *The Analyst* 2014, *139* (8), 1913–1921. https://doi.org/10.1039/C3AN02174B.

(56) Shvartsburg, A. A.; Smith, R. D. Fundamentals of Traveling Wave Ion Mobility Spectrometry. *Anal. Chem.* 2008, *80* (24), 9689–9699. https://doi.org/10.1021/ac8016295.

(57) Krylov, E. V.; Nazarov, E. G.; Miller, R. A. Differential Mobility Spectrometer: Model of Operation. *Int. J. Mass Spectrom.* 2007, *266* (1–3), 76–85. https://doi.org/10.1016/j.ijms.2007.07.003.

(58) Schneider, B. B.; Covey, T. R.; Coy, S. L.; Krylov, E. V.; Nazarov, E. G. Chemical Effects in the Separation Process of a Differential Mobility/Mass Spectrometer System. *Anal. Chem.* 2010, *82* (5), 1867–1880. https://doi.org/10.1021/ac902571u.

(59) Schneider, B. B.; Covey, T. R.; Coy, S. L.; Krylov, E. V.; Nazarov, E. G. Control of Chemical Effects in the Separation Process of a Differential Mobility Mass Spectrometer System. *Eur. J. Mass Spectrom.* **2010**, *16* (1), 57–71. https://doi.org/10.1255/ejms.1025.

(60) Ruskic, D.; Klont, F.; Hopfgartner, G. Clustering and Nonclustering Modifier Mixtures in Differential Mobility Spectrometry for Multidimensional Liquid Chromatography Ion Mobility–Mass Spectrometry Analysis. *Anal. Chem.* **2021**, *93* (17), 6638–6645. https://doi.org/10.1021/acs.analchem.0c04889.

(61) Nazarov, E. G.; Coy, S. L.; Krylov, E. V.; Miller, R. A.; Eiceman, G. A. Pressure Effects in Differential Mobility Spectrometry. *Anal. Chem.* **2006**, *78* (22), 7697–7706. https://doi.org/10.1021/ac061092z.

(62) Crouse, J.; Haack, A.; Benter, T.; Hopkins, W. S. Understanding Nontraditional Differential Mobility Behavior: A Case Study of the Tricarbastannatrane Cation, $N(CH_2CH_2CH_2)_3Sn^+$. *J. Am. Soc. Mass Spectrom.* **2020**, *31* (4), 796–802. https://doi.org/10.1021/jasms.9b00042.

(63) Liu, C.; Le Blanc, J. C. Y.; Shields, J.; Janiszewski, J. S.; Ieritano, C.; Ye, G. F.; Hawes, G. F.; Hopkins, W. S.; Campbell, J. L. Using Differential Mobility Spectrometry to Measure Ion Solvation: An Examination of the Roles of Solvents and Ionic Structures in Separating Quinoline-Based Drugs. *The Analyst* **2015**, *140* (20), 6897–6903. https://doi.org/10.1039/C5AN00842E.

(64) Allers, M.; Kirk, A. T.; von Roßbitzky, N.; Erdogdu, D.; Hillen, R.; Wissdorf, W.; Benter, T.; Zimmermann, S. Analyzing Positive Reactant Ions in High Kinetic Energy Ion Mobility Spectrometry (HiKE-IMS) by HiKE-IMS–MS. *J. Am. Soc. Mass Spectrom.* **2020**, *31* (4), 812–821. https://doi.org/10.1021/jasms.9b00087.

(65) Creese, A. J.; Cooper, H. J. Separation of Cis and Trans Isomers of Polyproline by FAIMS Mass Spectrometry. *J. Am. Soc. Mass Spectrom.* **2016**, *27* (12), 2071–2074. https://doi.org/10.1007/s13361-016-1482-1.

(66) Lane, C. S.; McManus, K.; Widdowson, P.; Flowers, S. A.; Powell, G.; Anderson, I.; Campbell, J. L. Separation of Sialylated Glycan Isomers by Differential Mobility Spectrometry. *Anal. Chem.* **2019**, *91* (15), 9916–9924. https://doi.org/10.1021/acs.analchem.9b01595.

(67) Anwar, A.; Psutka, J.; Walker, S. W. C.; Dieckmann, T.; Janizewski, J. S.; Larry Campbell, J.; Scott Hopkins, W. Separating and Probing Tautomers of Protonated Nucleobases Using Differential Mobility Spectrometry. *Int. J. Mass Spectrom.* **2018**, *429*, 174–181. https://doi.org/10.1016/j.ijms.2017.08.008.

(68) Walker, S. W. C.; Anwar, A.; Psutka, J. M.; Crouse, J.; Liu, C.; Le Blanc, J. C. Y.; Montgomery, J.; Goetz, G. H.; Janiszewski, J. S.; Campbell, J. L.; Hopkins, W. S. Determining Molecular Properties with Differential Mobility Spectrometry and Machine Learning. *Nat. Commun.* **2018**, *9* (1), 5096. https://doi.org/10.1038/s41467-018-07616-w.

(69) Coughlan, N. J. A.; Fu, W.; Guna, M.; Schneider, B. B.; Le Blanc, J. C. Y.; Campbell, J. L.; Hopkins, W. S. Electronic Spectroscopy of Differential Mobility-Selected Prototropic Isomers of Protonated *Para* -Aminobenzoic Acid. *Phys. Chem. Chem. Phys.* 2021, *23* (36), 20607–20614. https://doi.org/10.1039/D1CP02120F.

(70) Campbell, J. L.; Zhu, M.; Hopkins, W. S. Ion-Molecule Clustering in Differential Mobility Spectrometry: Lessons Learned from Tetraalkylammonium Cations and Their Isomers. *J. Am. Soc. Mass Spectrom.* 2014, *25* (9), 1583–1591. https://doi.org/10.1007/s13361-014-0939-3.

(71) Zhu, S.; Campbell, J. L.; Chernushevich, I.; Le Blanc, J. C. Y.; Wilson, D. J. Differential Mobility Spectrometry-Hydrogen Deuterium Exchange (DMS-HDX) as a Probe of Protein Conformation in Solution. *J. Am. Soc. Mass Spectrom.* 2016, *27* (6), 991–999. https://doi.org/10.1007/s13361-016-1364-6.

(72) Wales, D. J.; Doye, J. P. K. Global Optimization by Basin-Hopping and the Lowest Energy Structures of Lennard-Jones Clusters Containing up to 110 Atoms. *J. Phys. Chem. A* 1997, *101* (28), 5111–5116. https://doi.org/10.1021/jp970984n.

(73) Hashmi, I.; Shehu, A. HopDock: A Probabilistic Search Algorithm for Decoy Sampling in Protein-Protein Docking. *Proteome Sci.* 2013, *11* (Suppl 1), S6. https://doi.org/10.1186/1477-5956-11-S1-S6.

(74) Vanommeslaeghe, K.; Guvench, O.; MacKerell Jr, A. D. Molecular Mechanics. 2014, *20* (20), 3281–3292.

(75) Rappe, A. K.; Casewit, C. J.; Colwell, K. S.; Goddard, W. A.; Skiff, W. M. UFF, a Full Periodic Table Force Field for Molecular Mechanics and Molecular Dynamics Simulations. *J. Am. Chem. Soc.* 1992, *114* (25), 10024–10035. https://doi.org/10.1021/ja00051a040.

(76) Martin, M. G. Comparison of the AMBER, CHARMM, COMPASS, GROMOS, OPLS, TraPPE and UFF Force Fields for Prediction of Vapor–Liquid Coexistence Curves and Liquid Densities. *Fluid Phase Equilibria* 2006, *248* (1), 50–55. https://doi.org/10.1016/j.fluid.2006.07.014.

(77) Jones, R. O. Density Functional Theory: Its Origins, Rise to Prominence, and Future. *Rev. Mod. Phys.* 2015, *87* (3), 897–923. https://doi.org/10.1103/RevModPhys.87.897.

(78) Morgante, P.; Peverati, R. The Devil in the Details: A Tutorial Review on Some Undervalued Aspects of Density Functional Theory Calculations. *Int. J. Quantum Chem.* 2020, *120* (18). https://doi.org/10.1002/qua.26332.

(79) Mardirossian, N.; Head-Gordon, M. Thirty Years of Density Functional Theory in Computational Chemistry: An Overview and Extensive Assessment of 200 Density Functionals. *Mol. Phys.* 2017, *115* (19), 2315–2372. https://doi.org/10.1080/00268976.2017.1333644.

(80) Yanai, T.; Tew, D. P.; Handy, N. C. A New Hybrid Exchange–Correlation Functional Using the Coulomb-Attenuating Method (CAM-B3LYP). *Chem. Phys. Lett.* 2004, *393* (1–3), 51–57. https://doi.org/10.1016/j.cplett.2004.06.011.

(81) Ieritano, C.; Crouse, J.; Campbell, J. L.; Hopkins, W. S. A Parallelized Molecular Collision Cross Section Package with Optimized Accuracy and Efficiency. *The Analyst* 2019, *144* (5), 1660–1670. https://doi.org/10.1039/C8AN02150C.
(82) McQuarrie, D. A.; Simon, J. D. *Physical Chemistry A Molecular Approach*; University Science Books, 1997.
(83) Brodbelt, J. S. Photodissociation Mass Spectrometry: New Tools for Characterization of Biological Molecules. *Chem Soc Rev* 2014, *43* (8), 2757–2783. https://doi.org/10.1039/C3CS60444F.
(84) R. Julian, R. The Mechanism Behind Top-Down UVPD Experiments: Making Sense of Apparent Contradictions. *J. Am. Soc. Mass Spectrom.* 2017, *28* (9), 1823–1826. https://doi.org/10.1007/s13361-017-1721-0.
(85) Ly, T.; Julian, R. R. Ultraviolet Photodissociation: Developments towards Applications for Mass-Spectrometry-Based Proteomics. *Angew. Chem. Int. Ed.* 2009, *48* (39), 7130–7137. https://doi.org/10.1002/anie.200900613.
(86) Polfer, N. C. Infrared Multiple Photon Dissociation Spectroscopy of Trapped Ions. *Chem. Soc. Rev.* 2011, *40* (5), 2211. https://doi.org/10.1039/c0cs00171f.
(87) *Laser Photodissociation and Spectroscopy of Mass-Separated Biomolecular Ions*; Polfer, N. C., Dugourd, P., Eds.; Lecture Notes in Chemistry; Springer International Publishing: Cham, 2013; Vol. 83. https://doi.org/10.1007/978-3-319-01252-0.
(88) Sato, H. 4 Photodissociation in the Gas Phase. *Annu Rep Prog Chem Sect C Phys Chem* 2004, *100*, 73–98. https://doi.org/10.1039/B313672H.
(89) Williams, P. E.; Klein, D. R.; Greer, S. M.; Brodbelt, J. S. Pinpointing Double Bond and Sn-Positions in Glycerophospholipids via Hybrid 193 Nm Ultraviolet Photodissociation (UVPD) Mass Spectrometry. 2018, 23.
(90) Brodbelt, J. S.; Morrison, L. J.; Santos, I. Ultraviolet Photodissociation Mass Spectrometry for Analysis of Biological Molecules. *Chem. Rev.* 2020, *120* (7), 3328–3380. https://doi.org/10.1021/acs.chemrev.9b00440.
(91) Brodbelt, J. S. Ion Activation Methods for Peptides and Proteins. *Anal. Chem.* 2016, *88* (1), 30–51. https://doi.org/10.1021/acs.analchem.5b04563.
(92) Marlton, S. J. P.; McKinnon, B. I.; Ucur, B.; Maccarone, A. T.; Donald, W. A.; Blanksby, S. J.; Trevitt, A. J. Selecting and Identifying Gas-Phase Protonation Isomers of NicotineH $^{+}$ Using Combined Laser, Ion Mobility and Mass Spectrometry Techniques. *Faraday Discuss.* 2019, *217*, 453–475. https://doi.org/10.1039/C8FD00212F.
(93) Heldmaier, F. V.; Coughlan, N. J. A.; Haack, A.; Huard, R.; Guna, M.; Schneider, B. B.; Le Blanc, J. C. Y.; Campbell, J. L.; Nooijen, M.; Hopkins, W. S. UVPD Spectroscopy of Differential Mobility-Selected Prototropic Isomers of Protonated Adenine. *Phys. Chem. Chem. Phys.* 2021, *23* (35), 19892–19900. https://doi.org/10.1039/D1CP02688G.
(94) Coughlan, N. J. A.; Liu, C.; Lecours, M. J.; Campbell, J. L.; Hopkins, W. S. Preferential Ion Microsolvation in Mixed-Modifier Environments Observed Using Differential

Mobility Spectrometry. *J. Am. Soc. Mass Spectrom.* 2019, *30* (11), 2222–2227. https://doi.org/10.1007/s13361-019-02332-1.
(95) Dinu, L.; Groenenboom, G. C.; van der Zande, W. J. Competition between Photodetachment and Photodissociation in O2−. *J. Chem. Phys.* 2003, *119* (17), 8864–8872. https://doi.org/10.1063/1.1615517.
(96) Bloino, J.; Baiardi, A.; Biczysko, M. Aiming at an Accurate Prediction of Vibrational and Electronic Spectra for Medium-to-Large Molecules: An Overview. *Int. J. Quantum Chem.* 2016, *116* (21), 1543–1574. https://doi.org/10.1002/qua.25188.
(97) Sawaya, N. P. D.; Huh, J. Quantum Algorithm for Calculating Molecular Vibronic Spectra. *J. Phys. Chem. Lett.* 2019, *10* (13), 3586–3591. https://doi.org/10.1021/acs.jpclett.9b01117.
(98) Baiardi, A.; Bloino, J.; Barone, V. General Time Dependent Approach to Vibronic Spectroscopy Including Franck–Condon, Herzberg–Teller, and Duschinsky Effects. *J. Chem. Theory Comput.* 2013, *9* (9), 4097–4115. https://doi.org/10.1021/ct400450k.
(99) Barone, V.; Bloino, J.; Biczysko, M. Vibrationally-Resolved Electronic Spectra in GAUSSIAN 09. 20.
(100) Stuhlmann, F. O. B. Vibrational Investigation of Aromatics and their weakly bonded Clusters by Dispersed Fluorescence Spectroscopy and Franck-Condon Analysis. 216.
(101) Neese, F. The ORCA Program System. *WIREs Comput. Mol. Sci.* 2012, *2* (1), 73–78. https://doi.org/10.1002/wcms.81.
(102) Neese, F. Software Update: The ORCA Program System, Version 4.0. *WIREs Comput. Mol. Sci.* 2018, *8* (1). https://doi.org/10.1002/wcms.1327.
(103) Santoro, F.; Lami, A.; Improta, R.; Barone, V. Effective Method to Compute Vibrationally Resolved Optical Spectra of Large Molecules at Finite Temperature in the Gas Phase and in Solution. *J. Chem. Phys.* 2007, *126* (18), 184102. https://doi.org/10.1063/1.2721539.
(104) Avila Ferrer, F. J.; Santoro, F. Comparison of Vertical and Adiabatic Harmonic Approaches for the Calculation of the Vibrational Structure of Electronic Spectra. *Phys. Chem. Chem. Phys.* 2012, *14* (39), 13549. https://doi.org/10.1039/c2cp41169e.
(105) Biczysko, M.; Bloino, J.; Santoro, F.; Barone, V. Time-Independent Approaches to Simulate Electronic Spectra Lineshapes: From Small Molecules to Macrosystems. In *Computational Strategies for Spectroscopy*; Barone, V., Ed.; John Wiley & Sons, Inc.: Hoboken, NJ, USA, 2011; pp 361–443. https://doi.org/10.1002/9781118008720.ch8.
(106) Zara, Z.; Iqbal, J.; Ayub, K.; Irfan, M.; Mahmood, A.; Khera, R. A.; Eliasson, B. A Comparative Study of DFT Calculated and Experimental UV/Visible Spectra for Thirty Carboline and Carbazole Based Compounds. *J. Mol. Struct.* 2017, *1149*, 282–298. https://doi.org/10.1016/j.molstruc.2017.07.093.
(107) Halsey-Moore, C.; Jena, P.; McLeskey, J. T. Tuning Range-Separated DFT Functionals for Modeling the Peak Absorption of MEH-PPV Polymer in Various Solvents. *Comput. Theor. Chem.* 2019, *1162*, 112506. https://doi.org/10.1016/j.comptc.2019.112506.

(108) Pourseyed Lazarjani, M.; Torres, S.; Hooker, T.; Fowlie, C.; Young, O.; Seyfoddin, A. Methods for Quantification of Cannabinoids: A Narrative Review. *J. Cannabis Res.* 2020, *2* (1), 35. https://doi.org/10.1186/s42238-020-00040-2.

(109) Zou, S.; Kumar, U. Cannabinoid Receptors and the Endocannabinoid System: Signaling and Function in the Central Nervous System. *Int. J. Mol. Sci.* 2018, *19* (3), 833. https://doi.org/10.3390/ijms19030833.

(110) Atakan, Z. Cannabis, a Complex Plant: Different Compounds and Different Effects on Individuals. *Ther. Adv. Psychopharmacol.* 2012, *2* (6), 241–254. https://doi.org/10.1177/2045125312457586.

(111) Zuardi, A.; Crippa, J.; Hallak, J.; Pinto, J.; Chagas, M.; Rodrigues, G.; Dursun, S.; Tumas, V. Cannabidiol for the Treatment of Psychosis in Parkinson's Disease. *J. Psychopharmacol. (Oxf.)* 2009, *23* (8), 979–983. https://doi.org/10.1177/0269881108096519.

(112) Harvey, D. J. Mass Spectrometry of the Cannabinoids and Their Metabolites. *Mass Spectrom. Rev.* 1987, *6* (1), 135–229. https://doi.org/10.1002/mas.1280060104.

(113) Lindsay, C. M.; Abel, W. D.; Jones-Edwards, E. E.; Brown, P. D.; Bernard, K. K.; Taylor, T. T. Form and Content of Jamaican Cannabis Edibles. *J. Cannabis Res.* 2021, *3* (1), 29. https://doi.org/10.1186/s42238-021-00079-9.

(114) MacCallum, C. A.; Russo, E. B. Practical Considerations in Medical Cannabis Administration and Dosing. *Eur. J. Intern. Med.* 2018, *49*, 12–19. https://doi.org/10.1016/j.ejim.2018.01.004.

(115) Taura, F.; Sirikantaramas, S.; Shoyama, Y.; Yoshikai, K.; Shoyama, Y.; Morimoto, S. Cannabidiolic-Acid Synthase, the Chemotype-Determining Enzyme in the Fiber-Type *Cannabis Sativa*. *FEBS Lett.* 2007, *581* (16), 2929–2934. https://doi.org/10.1016/j.febslet.2007.05.043.

(116) Cardenia, V.; Gallina Toschi, T.; Scappini, S.; Rubino, R. C.; Rodriguez-Estrada, M. T. Development and Validation of a Fast Gas Chromatography/Mass Spectrometry Method for the Determination of Cannabinoids in Cannabis Sativa L. *J. Food Drug Anal.* 2018, *26* (4), 1283–1292. https://doi.org/10.1016/j.jfda.2018.06.001.

(117) Galand, N.; Ernouf, D.; Montigny, F.; Dollet, J.; Pothier, J. Separation and Identification of Cannabis Components by Different Planar Chromatography Techniques (TLC, AMD, OPLC). *J. Chromatogr. Sci.* 2004, *42* (3), 130–134. https://doi.org/10.1093/chromsci/42.3.130.

(118) Eckberg, M. N.; Arroyo-Mora, L. E.; Stoll, D. R.; DeCaprio, A. P. Separation and Identification of Isomeric and Structurally Related Synthetic Cannabinoids Using 2D Liquid Chromatography and High Resolution Mass Spectrometry. *J. Anal. Toxicol.* 2019, *43* (3), 170–178. https://doi.org/10.1093/jat/bky081.

(119) Protti, M.; Brighenti, V.; Battaglia, M. R.; Anceschi, L.; Pellati, F.; Mercolini, L. Cannabinoids from *Cannabis Sativa* L.: A New Tool Based on HPLC–DAD–MS/MS for a Rational Use in Medicinal Chemistry. *ACS Med. Chem. Lett.* 2019, *10* (4), 539–544. https://doi.org/10.1021/acsmedchemlett.8b00571.

(120) Hädener, M.; Kamrath, M. Z.; Weinmann, W.; Groessl, M. High-Resolution Ion Mobility Spectrometry for Rapid Cannabis Potency Testing. *Anal. Chem.* 2018, *90* (15), 8764–8768. https://doi.org/10.1021/acs.analchem.8b02180.

(121) dos Santos, N. A.; Souza, L. M.; Domingos, E.; França, H. S.; Lacerda, V.; Beatriz, A.; Vaz, B. G.; Rodrigues, R. R. T.; Carvalho, V. V.; Merlo, B. B.; Kuster, R. M.; Romão, W. Evaluating the Selectivity of Colorimetric Test (Fast Blue BB Salt) for the Cannabinoids Identification in Marijuana Street Samples by UV–Vis, TLC, ESI(+)FT-ICR MS and ESI(+)MS/MS. *Forensic Chem.* 2016, *1*, 13–21. https://doi.org/10.1016/j.forc.2016.07.001.

(122) França, H. S.; Acosta, A.; Jamal, A.; Romao, W.; Mulloor, J.; Almirall, J. R. Experimental and Ab Initio Investigation of the Products of Reaction from Δ9-Tetrahydrocannabinol (Δ9-THC) and the Fast Blue BB Spot Reagent in Presumptive Drug Tests for Cannabinoids. *Forensic Chem.* 2020, *17*, 100212. https://doi.org/10.1016/j.forc.2019.100212.

(123) Cumeras, R.; Figueras, E.; Davis, C. E.; Baumbach, J. I.; Gràcia, I. Review on Ion Mobility Spectrometry. Part 1: Current Instrumentation. *The Analyst* 2015, *140* (5), 1376–1390. https://doi.org/10.1039/C4AN01100G.

(124) Cumeras, R.; Figueras, E.; Davis, C. E.; Baumbach, J. I.; Gràcia, I. Review on Ion Mobility Spectrometry. Part 2: Hyphenated Methods and Effects of Experimental Parameters. *The Analyst* 2015, *140* (5), 1391–1410. https://doi.org/10.1039/C4AN01101E.

(125) Tose, L. V.; Santos, N. A.; Rodrigues, R. R. T.; Murgu, M.; Gomes, A. F.; Vasconcelos, G. A.; Souza, P. C. T.; Vaz, B. G.; Romão, W. Isomeric Separation of Cannabinoids by UPLC Combined with Ionic Mobility Mass Spectrometry (TWIM-MS)—Part I. *Int. J. Mass Spectrom.* 2017, *418*, 112–121. https://doi.org/10.1016/j.ijms.2016.10.018.

(126) Campbell, J. L.; Baba, T.; Liu, C.; Lane, C. S.; Le Blanc, J. C. Y.; Hager, J. W. Analyzing Glycopeptide Isomers by Combining Differential Mobility Spectrometry with Electron- and Collision-Based Tandem Mass Spectrometry. *J. Am. Soc. Mass Spectrom.* 2017, *28* (7), 1374–1381. https://doi.org/10.1007/s13361-017-1663-6.

(127) Zhou, C.; Ieritano, C.; Hopkins, W. S. Augmenting Basin-Hopping With Techniques From Unsupervised Machine Learning: Applications in Spectroscopy and Ion Mobility. *Front. Chem.* 2019, *7*, 519. https://doi.org/10.3389/fchem.2019.00519.

(128) Scott Hopkins, W.; Marta, R. A.; Steinmetz, V.; McMahon, T. B. Mode-Specific Fragmentation of Amino Acid-Containing Clusters. *Phys. Chem. Chem. Phys.* 2015, *17* (43), 28548–28555. https://doi.org/10.1039/C5CP03517A.

(129) Gaussian 16, Revision C.01, Frisch, M. J.; Trucks, G. W.; Schlegel, H. B.; Scuseria, G. E.; Robb, M. A.; Cheeseman, J. R.; Scalmani, G.; Barone, V.; Petersson, G. A.; Nakatsuji, H.; Li, X.; Caricato, M.; Marenich, A. V.; Bloino, J.; Janesko, B. G.; Gomperts, R.; Mennucci, B.; Hratchian, H. P.; Ortiz, J. V.; Izmaylov, A. F.; Sonnenberg, J. L.; Williams-Young, D.; Ding, F.; Lipparini, F.; Egidi, F.; Goings, J.; Peng, B.; Petrone, A.; Henderson, T.; Ranasinghe, D.; Zakrzewski, V. G.; Gao, J.; Rega, N.; Zheng, G.; Liang, W.; Hada, M.;

Ehara, M.; Toyota, K.; Fukuda, R.; Hasegawa, J.; Ishida, M.; Nakajima, T.; Honda, Y.; Kitao, O.; Nakai, H.; Vreven, T.; Throssell, K.; Montgomery, J. A., Jr.; Peralta, J. E.; Ogliaro, F.; Bearpark, M. J.; Heyd, J. J.; Brothers, E. N.; Kudin, K. N.; Staroverov, V. N.; Keith, T. A.; Kobayashi, R.; Normand, J.; Raghavachari, K.; Rendell, A. P.; Burant, J. C.; Iyengar, S. S.; Tomasi, J.; Cossi, M.; Millam, J. M.; Klene, M.; Adamo, C.; Cammi, R.; Ochterski, J. W.; Martin, R. L.; Morokuma, K.; Farkas, O.; Foresman, J. B.; Fox, D. J. Gaussian, Inc., (130) Grimme, S.; Antony, J.; Ehrlich, S.; Krieg, H. A Consistent and Accurate *Ab Initio* Parametrization of Density Functional Dispersion Correction (DFT-D) for the 94 Elements H-Pu. *J. Chem. Phys.* 2010, *132* (15), 154104. https://doi.org/10.1063/1.3382344.

(131) Lam, K. H. B.; Le Blanc, J. C. Y.; Campbell, J. L. Separating Isomers, Conformers, and Analogues of Cyclosporin Using Differential Mobility Spectroscopy, Mass Spectrometry, and Hydrogen–Deuterium Exchange. *Anal. Chem.* 2020, *92* (16), 11053–11061. https://doi.org/10.1021/acs.analchem.0c00191.

(132) Berman, P.; Futoran, K.; Lewitus, G. M.; Mukha, D.; Benami, M.; Shlomi, T.; Meiri, D. A New ESI-LC/MS Approach for Comprehensive Metabolic Profiling of Phytocannabinoids in Cannabis. *Sci. Rep.* 2018, *8* (1), 14280. https://doi.org/10.1038/s41598-018-32651-4.

(133) Meng, Q.; Buchanan, B.; Zuccolo, J.; Poulin, M.-M.; Gabriele, J.; Baranowski, D. C. A Reliable and Validated LC-MS/MS Method for the Simultaneous Quantification of 4 Cannabinoids in 40 Consumer Products. *PLOS ONE* 2018, *13* (5), e0196396. https://doi.org/10.1371/journal.pone.0196396.

(134) Romano, L. L.; Hazekamp, A. Cannabis Oil: Chemical Evaluation of an Upcoming Cannabis-Based Medicine. 2013, *7* (1), 12.

(135) Wei, B.; Wang, L.; Blount, B. C. Analysis of Cannabinoids and Their Metabolites in Human Urine. *Anal. Chem.* 2015, *87* (20), 10183–10187. https://doi.org/10.1021/acs.analchem.5b02603.

(136) Strano-Rossi, S.; Chiarotti, M. Solid-Phase Microextraction for Cannabinoids Analysis in Hair and Its Possible Application to Other Drugs*. *J. Anal. Toxicol.* 1999, *23* (1), 7–10. https://doi.org/10.1093/jat/23.1.7.

(137) Anzillotti, L.; Castrignanò, E.; Rossi, S. S.; Chiarotti, M. Cannabinoids Determination in Oral Fluid by SPME–GC/MS and UHPLC–MS/MS and Its Application on Suspected Drivers. *Sci. Justice* 2014, *54* (6), 421–426. https://doi.org/10.1016/j.scijus.2014.08.004.

(138) Reyes-Garcés, N.; Gionfriddo, E.; Gómez-Ríos, G. A.; Alam, Md. N.; Boyacı, E.; Bojko, B.; Singh, V.; Grandy, J.; Pawliszyn, J. Advances in Solid Phase Microextraction and Perspective on Future Directions. *Anal. Chem.* 2018, *90* (1), 302–360. https://doi.org/10.1021/acs.analchem.7b04502.

(139) Herrington, J. S.; Gómez-Ríos, G. A.; Myers, C.; Stidsen, G.; Bell, D. S. Hunting Molecules in Complex Matrices with SPME Arrows: A Review. *Separations* 2020, *7* (1), 12. https://doi.org/10.3390/separations7010012.

(140) Andrade-Eiroa, A.; Canle, M.; Leroy-Cancellieri, V.; Cerdà, V. Solid-Phase Extraction of Organic Compounds: A Critical Review. Part Ii. *TrAC Trends Anal. Chem.* 2016, *80*, 655–667. https://doi.org/10.1016/j.trac.2015.08.014.
(141) Gómez-Ríos, G. A.; Liu, C.; Tascon, M.; Reyes-Garcés, N.; Arnold, D. W.; Covey, T. R.; Pawliszyn, J. Open Port Probe Sampling Interface for the Direct Coupling of Biocompatible Solid-Phase Microextraction to Atmospheric Pressure Ionization Mass Spectrometry. *Anal. Chem.* 2017, *89* (7), 3805–3809. https://doi.org/10.1021/acs.analchem.6b04737.
(142) Wang, Y.; Alhajji, E.; Rieul, B.; Berthias, F.; Maître, P. Infrared Isomer-Specific Fragmentation for the Identification of Aminobutyric Acid Isomers Separated by Differential Mobility Spectrometry. *Int. J. Mass Spectrom.* 2019, *443*, 16–21. https://doi.org/10.1016/j.ijms.2019.05.014.
(143) Coughlan, N. J. A.; Carr, P. J. J.; Walker, S. C.; Zhou, C.; Guna, M.; Campbell, J. L.; Hopkins, W. S. Measuring Electronic Spectra of Differential Mobility-Selected Ions in the Gas Phase. *J. Am. Soc. Mass Spectrom.* 2020, *31* (2), 405–410. https://doi.org/10.1021/jasms.9b00039.
(144) Groessl, M.; Graf, S.; Knochenmuss, R. High Resolution Ion Mobility-Mass Spectrometry for Separation and Identification of Isomeric Lipids. *The Analyst* 2015, *140* (20), 6904–6911. https://doi.org/10.1039/C5AN00838G.
(145) Priest, R. G. A Comparative Trial of Protriptyline and Nortriptyline. *Curr. Med. Res. Opin.* 1976, *3* (10), 710–715. https://doi.org/10.1185/03007997609111965.
(146) Arce, R.; García, C.; Oyola, R.; Piñero, L.; Nieves, I.; Cruz, N. Photophysical and Photochemical Properties of Amitriptyline and Nortriptyline Hydrochloride: A 266 Nm Nanosecond Laser Flash and Theoretical Study. *J. Photochem. Photobiol. Chem.* 2003, *154* (2–3), 245–257. https://doi.org/10.1016/S1010-6030(02)00353-2.
(147) Moreno, M. A.; Ballesteros, M. P.; Frutos, P.; Lastres, J. L.; Castro, D. Comparison of UV Spectrophotometric and LC Methods for the Determination of Nortriptyline Hydrochloride in Polysorbate 80 Based Oil/Water (o/w) Microemulsions. *J. Pharm. Biomed. Anal.* 2000, *22* (2), 287–294. https://doi.org/10.1016/S0731-7085(99)00285-X.
(148) García, C.; Oyola, R.; Piñero, L.; Cruz, N.; Alejandro, F.; Arce, R.; Nieves, I. Photophysical, Electrochemical, and Theoretical Study of Protriptyline in Several Solvents. *J. Phys. Chem. B* 2002, *106* (38), 9794–9801. https://doi.org/10.1021/jp0257855.
(149) Frisch, M. J.; Trucks, G. W.; Schelegel, H. B.; Scuseria, G. E.; Robb, M. A.; Cheeseman, J. R.; Scalmani, G.; Barone, V.; Petersson, G. A.; Nakatsuji, H.; Li, X.; Caricato, M.; Marenich. *Gaussian 16, Rev. C.01*; Gaussian Inc.: Wallingford, CT, 2016.
(150) Martin, R. L. Natural Transition Orbitals. 4.
(151) Mollerup, C. B.; Mardal, M.; Dalsgaard, P. W.; Linnet, K.; Barron, L. P. Prediction of Collision Cross Section and Retention Time for Broad Scope Screening in Gradient Reversed-Phase Liquid Chromatography-Ion Mobility-High Resolution Accurate Mass

Spectrometry. *J. Chromatogr. A* 2018, *1542*, 82–88. https://doi.org/10.1016/j.chroma.2018.02.025.
(152) Ieritano, C.; Lee, A.; Crouse, J.; Bowman, Z.; Mashmoushi, N.; Crossley, P. M.; Friebe, B. P.; Campbell, J. L.; Hopkins, W. S. Determining Collision Cross Sections from Differential Ion Mobility Spectrometry. *Anal. Chem.* 2021, *93* (25), 8937–8944. https://doi.org/10.1021/acs.analchem.1c01420.
(153) Niessen, W. M. A. Interpretation of Tandem Mass Spectra of Antiepileptic Drugs Using Accurate-m/z Data and m/z-Shifts with Stable-Isotope Labeled Analogues. *Int. J. Mass Spectrom.* 2020, *456*, 116409. https://doi.org/10.1016/j.ijms.2020.116409.
(154) Niessen, W. M. A. Fragmentation of Toxicologically Relevant Drugs in Positive-Ion Liquid Chromatography-Tandem Mass Spectrometry: FRAGMENTATION OF TOXICOLOGICALLY RELEVANT DRUGS. *Mass Spectrom. Rev.* 2011, *30* (4), 626–663. https://doi.org/10.1002/mas.20332.
(155) Sagdinc, S. G.; Azkeskin, C.; Eşme, A. Theoretical and Spectroscopic Studies of a Tricyclic Antidepressant, Imipramine Hydrochloride. *J. Mol. Struct.* 2018, *1161*, 169–184. https://doi.org/10.1016/j.molstruc.2018.02.056.
(156) Landru, N.; Georges, T.; Beaurepaire, J.; Le Guen, B.; Le Bail, G. Demonstration of Miniaturized 20mW CW 280nm and 266nm Solid-State UV Laser Sources; Clarkson, W. A., Shori, R. K., Eds.; San Francisco, California, United States, 2015; p 93420R. https://doi.org/10.1117/12.2079558.
(157) Halder, A.; Vemuri, S.; Roy, R.; Katuri, J.; Bhattacharyya, D.; Mitra, A. Evidence for Hidden Involvement of N3-Protonated Guanine in RNA Structure and Function. *ACS Omega* 2019, *4* (1), 699–709. https://doi.org/10.1021/acsomega.8b02908.
(158) Zhang, Y.; de La Harpe, K.; Beckstead, A. A.; Improta, R.; Kohler, B. UV-Induced Proton Transfer between DNA Strands. *J. Am. Chem. Soc.* 2015, *137* (22), 7059–7062. https://doi.org/10.1021/jacs.5b03914.
(159) Celie, P. H. N.; van Rossum-Fikkert, S. E.; van Dijk, W. J.; Brejc, K.; Smit, A. B.; Sixma, T. K. Nicotine and Carbamylcholine Binding to Nicotinic Acetylcholine Receptors as Studied in AChBP Crystal Structures. *Neuron* 2004, *41* (6), 907–914. https://doi.org/10.1016/S0896-6273(04)00115-1.
(160) Tian, Z.; Kass, S. R. Gas-Phase versus Liquid-Phase Structures by Electrospray Ionization Mass Spectrometry. *Angew. Chem. Int. Ed.* 2009, *48* (7), 1321–1323. https://doi.org/10.1002/anie.200805392.
(161) Joyce, J. R.; Richards, D. S. Kinetic Control of Protonation in Electrospray Ionization. *J. Am. Soc. Mass Spectrom.* 2011, *22* (2), 360–368. https://doi.org/10.1007/s13361-010-0037-0.
(162) Almasian, M.; Grzetic, J.; van Maurik, J.; Steill, J. D.; Berden, G.; Ingemann, S.; Buma, W. J.; Oomens, J. Non-Equilibrium Isomer Distribution of the Gas-Phase Photoactive Yellow Protein Chromophore. *J. Phys. Chem. Lett.* 2012, *3* (16), 2259–2263. https://doi.org/10.1021/jz300780t.

(163) Noble, J. A.; Broquier, M.; Grégoire, G.; Soorkia, S.; Pino, G.; Marceca, E.; Dedonder-Lardeux, C.; Jouvet, C. Tautomerism and Electronic Spectroscopy of Protonated 1- and 2-Aminonaphthalene. *Phys. Chem. Chem. Phys.* **2018**, *20* (9), 6134–6145. https://doi.org/10.1039/C8CP00218E.

(164) Warnke, S.; Seo, J.; Boschmans, J.; Sobott, F.; Scrivens, J. H.; Bleiholder, C.; Bowers, M. T.; Gewinner, S.; Schöllkopf, W.; Pagel, K.; von Helden, G. Protomers of Benzocaine: Solvent and Permittivity Dependence. *J. Am. Chem. Soc.* **2015**, *137* (12), 4236–4242. https://doi.org/10.1021/jacs.5b01338.

(165) Patrick, A. L.; Cismesia, A. P.; Tesler, L. F.; Polfer, N. C. Effects of ESI Conditions on Kinetic Trapping of the Solution-Phase Protonation Isomer of p-Aminobenzoic Acid in the Gas Phase. *Int. J. Mass Spectrom.* **2017**, *418*, 148–155. https://doi.org/10.1016/j.ijms.2016.09.022.

(166) Xia, H.; Attygalle, A. B. Untrapping Kinetically Trapped Ions: The Role of Water Vapor and Ion-Source Activation Conditions on the Gas-Phase Protomer Ratio of Benzocaine Revealed by Ion-Mobility Mass Spectrometry. *J. Am. Soc. Mass Spectrom.* **2017**, *28* (12), 2580–2587. https://doi.org/10.1007/s13361-017-1806-9.

(167) Li, J.; Santambrogio, C.; Brocca, S.; Rossetti, G.; Carloni, P.; Grandori, R. Conformational Effects in Protein Electrospray-Ionization Mass Spectrometry: NATIVE PROTEIN ESI-MS. *Mass Spectrom. Rev.* **2016**, *35* (1), 111–122. https://doi.org/10.1002/mas.21465.

(168) Matthews, E. Experiment and Theory Confirm That UV Laser Photodissociation Spectroscopy Can Distinguish Protomers Formed via Electrospray. **2017**, 7.

(169) Bull, J. N.; Coughlan, N. J. A.; Bieske, E. J. Protomer-Specific Photochemistry Investigated Using Ion Mobility Mass Spectrometry. *J. Phys. Chem. A* **2017**, *121* (32), 6021–6027. https://doi.org/10.1021/acs.jpca.7b05800.

(170) Li, H.; Sheng, Y.; McGee, W.; Cammarata, M.; Holden, D.; Loo, J. A. Structural Characterization of Native Proteins and Protein Complexes by Electron Ionization Dissociation-Mass Spectrometry. *Anal. Chem.* **2017**, *89* (5), 2731–2738. https://doi.org/10.1021/acs.analchem.6b02377.

(171) Sarich, T. C.; Peters, G.; Berkowitz, S. D.; Misselwitz, F.; Nessel, C. C.; Burton, P.; Cook-Bruns, N.; Lensing, A. W. A.; Haskell, L.; Perzborn, E.; Kubitza, D.; Moore, K. T.; Jalota, S.; Weber, J.; Pan, G.; Sun, X.; Westermeier, T.; Nadel, A.; Oppenheimer, L.; DiBattiste, P. M. Rivaroxaban: A Novel Oral Anticoagulant for the Prevention and Treatment of Several Thrombosis-Mediated Conditions: Rivaroxaban: A Novel Oral Anticoagulant. *Ann. N. Y. Acad. Sci.* **2013**, *1291* (1), 42–55. https://doi.org/10.1111/nyas.12136.

(172) Londry, F. A.; Hager, J. W. Mass Selective Axial Ion Ejection from a Linear Quadrupole Ion Trap. *J. Am. Soc. Mass Spectrom.* **2003**, *14* (10), 1130–1147. https://doi.org/10.1016/S1044-0305(03)00446-X.

(173) Antoine, R.; Dugourd, P. Visible and Ultraviolet Spectroscopy of Gas Phase Protein Ions. *Phys. Chem. Chem. Phys.* **2011**, *13* (37), 16494. https://doi.org/10.1039/c1cp21531k.

(174) Lecours, M. J.; Chow, W. C. T.; Hopkins, W. S. Density Functional Theory Study of $Rh_n S^{0,\pm}$ and $Rh_{n+1}^{0,\pm}$ (n = 1–9). *J. Phys. Chem. A* **2014**, *118* (24), 4278–4287. https://doi.org/10.1021/jp412457m.

(175) Alia, J. D.; Flack, J. A. Unspecified Verticality of Franck–Condon Transitions, Absorption and Emission Spectra of Cyanine Dyes, and a Classically Inspired Approximation. *RSC Adv.* **2020**, *10* (70), 43153–43167. https://doi.org/10.1039/D0RA06774A.

(176) Götze, J. P.; Karasulu, B.; Thiel, W. Computing UV/Vis Spectra from the Adiabatic and Vertical Franck-Condon Schemes with the Use of Cartesian and Internal Coordinates. *J. Chem. Phys.* **2013**, *139* (23), 234108. https://doi.org/10.1063/1.4844055.

(177) Krylov, E. V.; Coy, S. L.; Nazarov, E. G. Temperature Effects in Differential Mobility Spectrometry. *Int. J. Mass Spectrom.* **2009**, *279* (2–3), 119–125. https://doi.org/10.1016/j.ijms.2008.10.025.

(178) Schneider, B. B.; Nazarov, E. G.; Londry, F.; Vouros, P.; Covey, T. R. Differential Mobility Spectrometry/Mass Spectrometry History, Theory, Design Optimization, Simulations, and Applications: DIFFERENTIAL MOBILITY SPECTROMETRY/MASS SPECTROMETRY. *Mass Spectrom. Rev.* **2016**, *35* (6), 687–737. https://doi.org/10.1002/mas.21453.

(179) Ramisetti, N. R.; Kuntamukkala, R. Development and Validation of a Stability Indicating LC-PDA-MS/MS Method for Separation, Identification and Characterization of Process Related and Stress Degradation Products of Rivaroxaban. *RSC Adv.* **2014**, *4* (44), 23155. https://doi.org/10.1039/c4ra00744a.

(180) van Dishoeck, E. F.; Visser, R. Molecular Photodissociation. *ArXiv11063917 Astro-Ph Physicsphysics* **2015**.

(181) Mori, T.; Inoue, Y. Charge-Transfer Excitation: Unconventional yet Practical Means for Controlling Stereoselectivity in Asymmetric Photoreactions. *Chem. Soc. Rev.* **2013**, *42* (20), 8122. https://doi.org/10.1039/c3cs60117j.

Appendices

Appendix A – The Separation of Cannabinoid Isomers using DMS-MS

A.1 Experimental and instrumental conditions

Table A- 1. Instrumental conditions used for the separation of cannabinoid isomers

Source/Gas Conditions			
Ion Source:	TurboSpray	**Temperature:**	34 °C
Curtain Gas:	20 psi	**Ion Source Gas 1:**	20 psi
Collision Gas:	High	**Ion Source Gas 2:**	0 psi
Polarity:	Negative Mode	**Ion Spray Voltage:**	−4500 V
Compound Conditions			
Declustering Potential:	−100.0 V	**Excitation Energy:**	0.100 V
Collision Energy:	−10.0 V	**CE Spread:**	0.00 V
Entrance Potential:	−10.0 V		
DMS Conditions			
DMS Temperature*:	150 °C for decarboxylated 225 °C for acids,	**CV Ramp:**	0.1 V
DMS Offset:	−3.0 V	**Resolving Gas:**	20
Modifier at 1.5% *(v/v*)*:	IPA		

*An equilibration time of 15 min is given when modifying the DMS temperature prior to any experiments being run, or when a modifier is newly introduced.

A.2 Mass spectrometric analyses of cannabinoid ions

The cannabinoid derivatives were analyzed in the negative mode to improve the total parent *m/z* ion signal, increasing sensitivity. Protonation of some of the isomers results in lower ionization efficiencies for some derivatives. Product ion scans of Δ^9-THC and CBC in the protonated and deprotonated cases are provided to showcase the relative ionization efficiencies of each parent ion *m/z* peak.

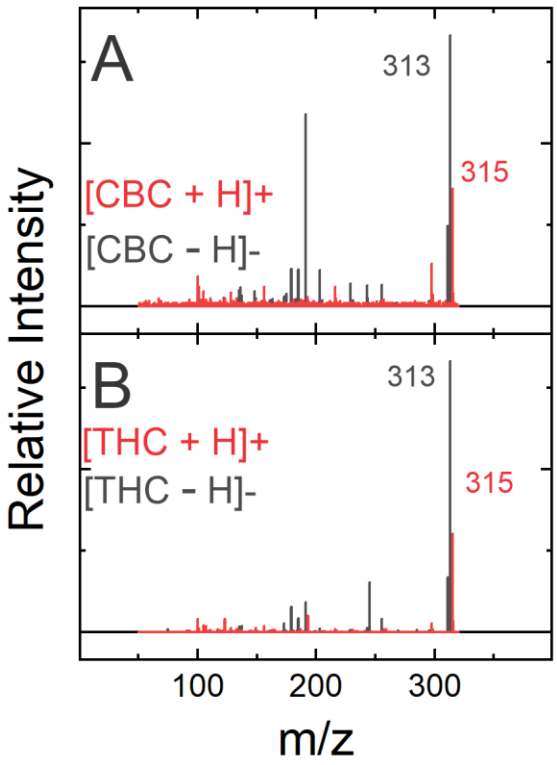

Figure A-1. Product ion scans of protonated and deprotonated (**A**) CBC and (**B**) Δ^9-THC.

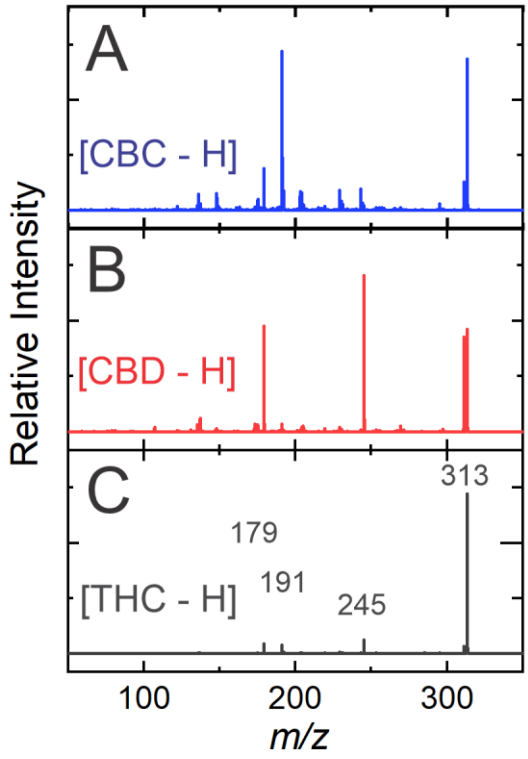

Figure A- 2. Enhanced product ion scans of (**A**) $[CBC - H]^-$, (**B**) $[CBD - H]^-$ and (**C**) $[\Delta^9\text{-}THC - H]^-$, using a collision energy of −30 V show similar product ions but variation in product ion relative intensities.

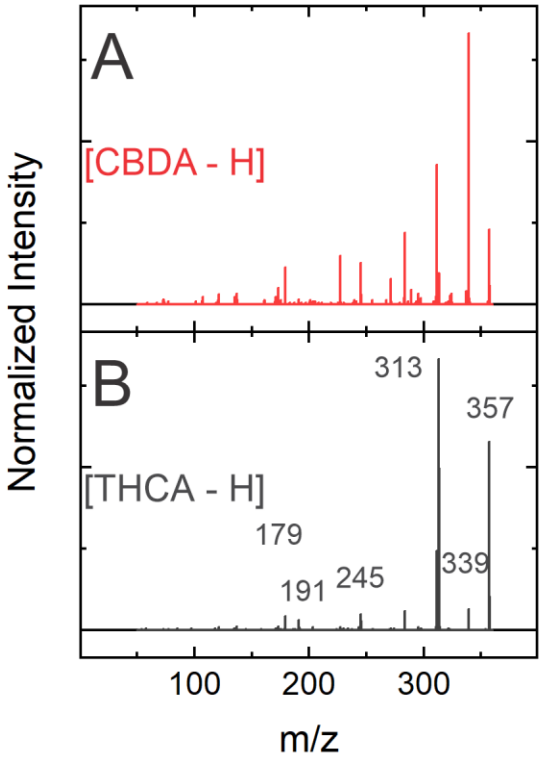

Figure A- 3. Enhanced product ion scans of (**A**) $[CBDA - H]^-$ and (**B**) $[THCA - H]^-$ using a collision energy of −30 V show similar product ions but variation in product ion relative intensities.

A.3 The Addition of Resolving Gas

The resolving gas (DR) is N_2 gas added at a determined flow rate to the end of the DMS cell to extend the ion residence time in the DMS cell, improving the resolution. The flow rate and ion residence time attributed to each DR value are tabulated below.

Table A- 2. Resolving gas conditions and corresponding flow rate and residence times.

DR value:	Flow rate (cm^3/ms):	Ion residence time (ms):
8	0.014966	9.463722
10	0.016833	10.05587
12	0.018617	10.69519
14	0.020283	11.37081
16	0.021883	12.10491
18	0.023367	12.87554
20	0.024900	13.78254
22	0.026333	14.75410

A.4 The Behavior of Cannabinoid Derivatives under Various Modifier Conditions

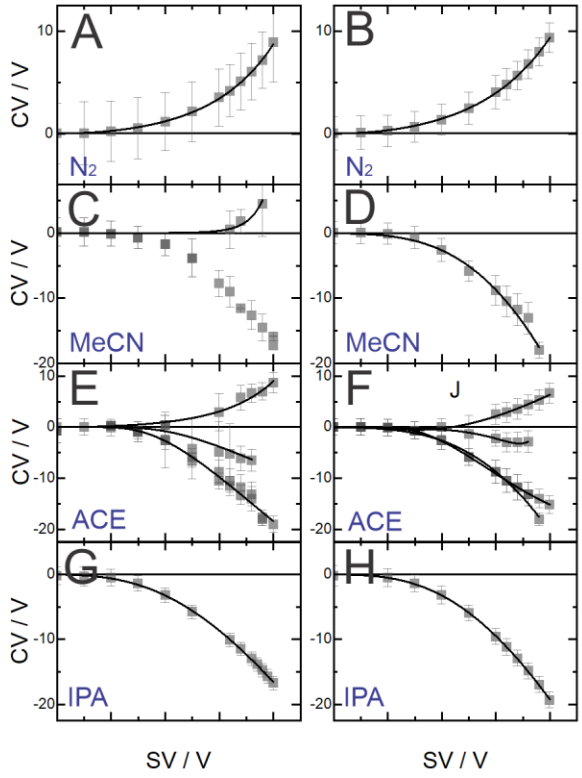

Figure A-4. The dispersion plots of CBD (*left*) and CBC (*right*) in (**A**) and (**B**) N_2 conditions, (**C**) and (**D**) MeCN-modified conditions, (**E**) and (**F**) acetone-modified conditions, and (**G**) and (**H**) IPA-modified conditions.

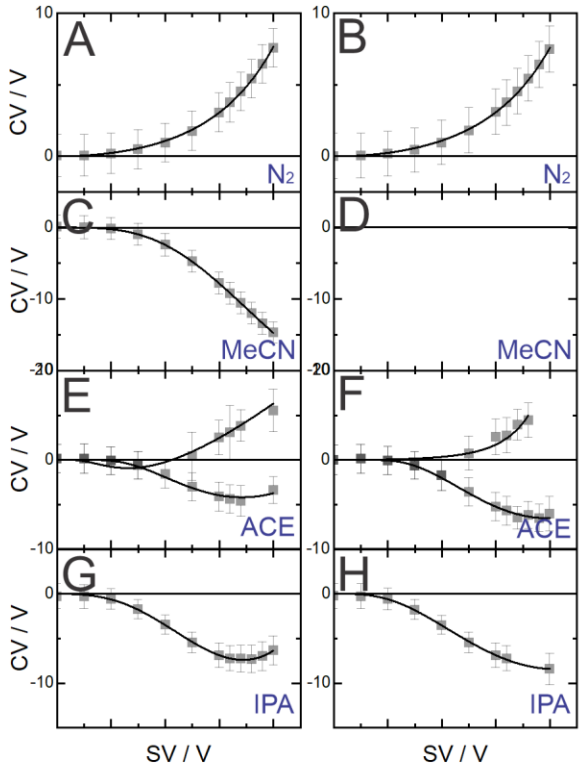

Figure A- 5. The dispersion plots of CBDA (*left*) and (−)-THCA (*right*) in (**A**) and (**B**) N_2 conditions, (**C**) and (**D**) MeCN-modified conditions, (E) and (F) acetone-modified conditions, and (**G**) and (**H**) IPA-modified conditions.

A.5 Preferential Solvation Studies Observed in Acetone Modifier Conditions

A.5.1 Sample Temperature Studies for Cannabinoid Isomers

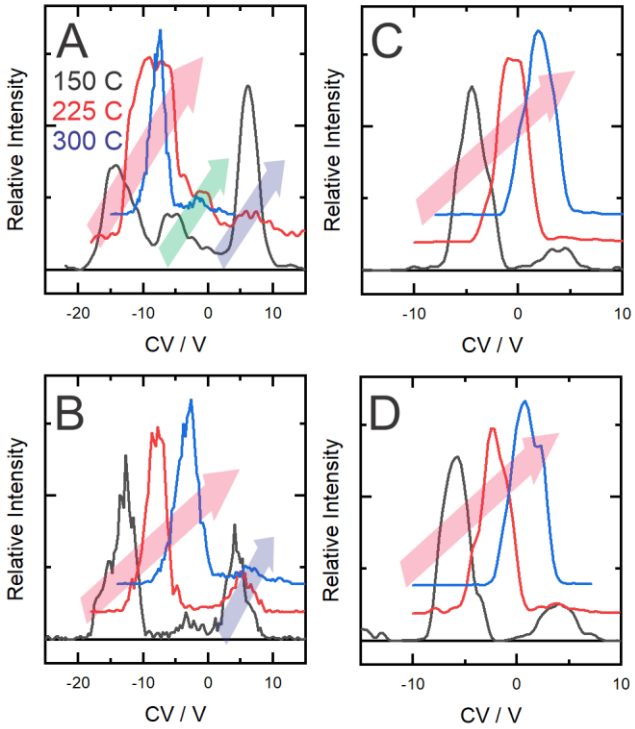

Figure A- 6. Temperature studies of (**A**) CBD, (**B**) CBC, (**C**) CBDA, and (**D**) THCA anions under N_2 seeded with 1.5% acetone vapor taken at SV = 3600 V.

A.5.2 Precursor Ion Studies of Cannabinoid DMS Peaks

Precursor ion scans were taken for each SV/CV pair noted in the previous figures for the decarboxylated anion species. Agreement with solvent studies were found, in which peak I consistently contained a *m/z* 429 peak, pertaining to the deprotonated analyte clustered with 2 acetone molecules. Peak II contained a *m/z* 373 peak, corresponding to the deprotonated analyte clustered with acetic acid. Peak III showed a *m/z* 627 peak, likely indicated a proton-bound dimer of the deprotonated analyte with its neutral counterpart. It is noted that even though solvent studies showed dependence of peak intensity of peaks III and IV on methanol and acetonitrile, respectively, precursor ion scans did not show peaks corresponding to these.

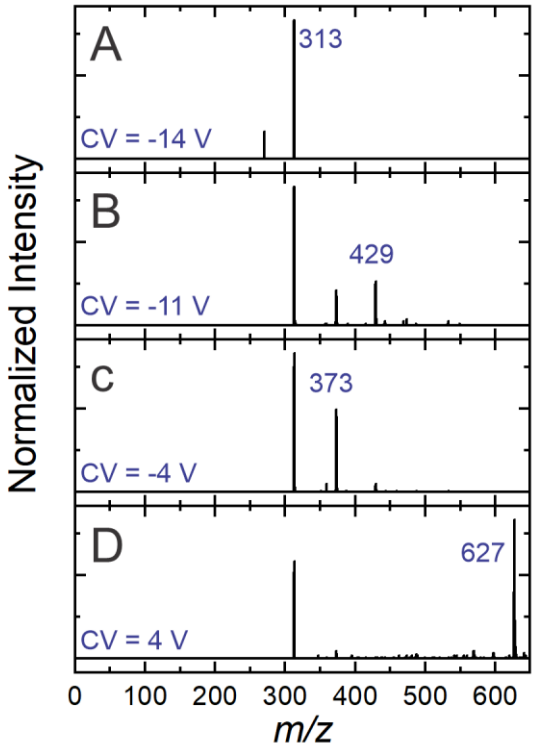

Figure A- 7. Precursor ion scans of peaks I-IV taken at DcP set to 0 V for $[THC - H]^-$ in an N_2 carrier gas environment seeded with 1.5% (*v/v*) acetone. Ions of interest are labelled.

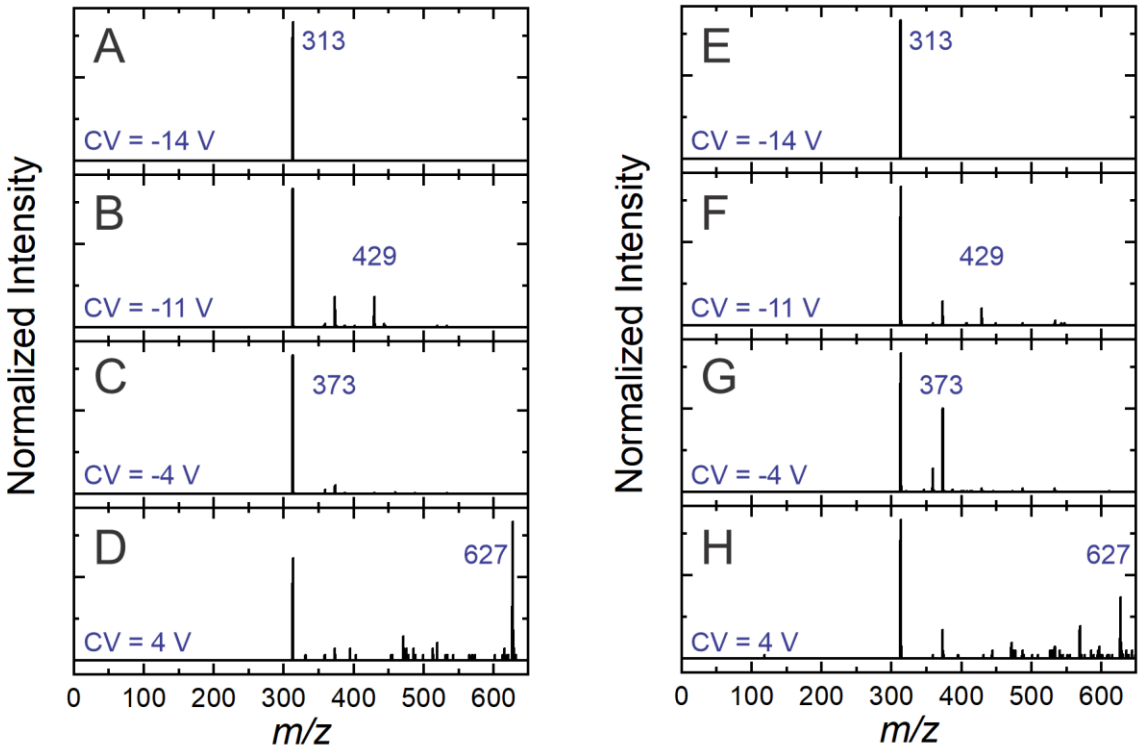

Figure A- 8. Precursor ion scans of peaks I-IV taken at DcP set to 0 V for [CBD-H]^- (**A** – **D**) and $[CBC - H]^-$ (**E** – **H**) in an N_2 carrier gas environment seeded with 1.5% (*v/v*) acetone. Ions of interest are labelled.

A.5.3 Precursor Ion Studies of MeCN-Modified Conditions

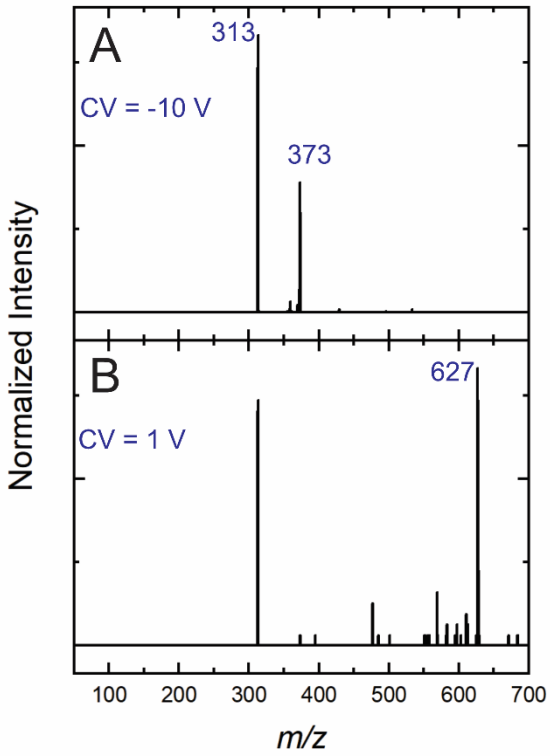

Figure A- 9. Precursor ion scans of deprotonated THC in N_2 seeded with 1.5% (*v/v*) MeCN at SV = 3600 V for the ion populations at (**A**) CV = −10 V and (**B**) CV = 1 V. The ion population at CV = −10 V includes an adduct with acetic acid, while the ion population at CV = 1 V includes a THC dimer.

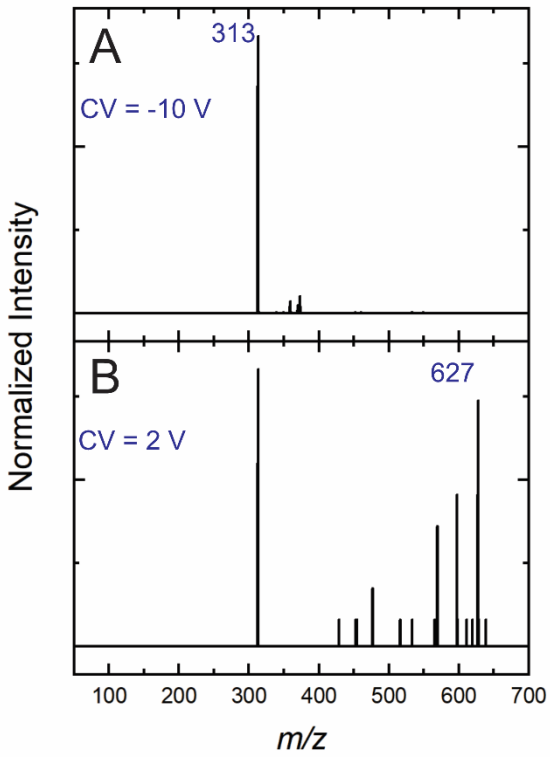

Figure A- 10. Precursor ion scans of deprotonated CBD in N_2 seeded with 1.5% (*v/v*) MeCN at SV = 3600 V for the ion populations at (**A**) CV = −10 V and (**B**) CV = 2 V. The ion population at CV = 2 V includes a CBD dimer.

A.5.4 IPA Modifier Studies

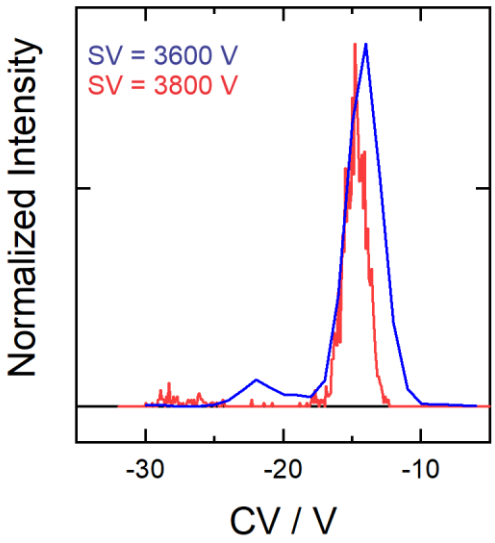

Figure A- 11. Ionogram of $[THC - H]^-$ taken under N_2 gas conditions seeded with 1.5% (*v/v*) IPA at T = 150 °C at SV = 3600 V (*blue*) and SV = 3800 V (*red*) shows the disappearance of the minor ionogram peak with increasing SV.

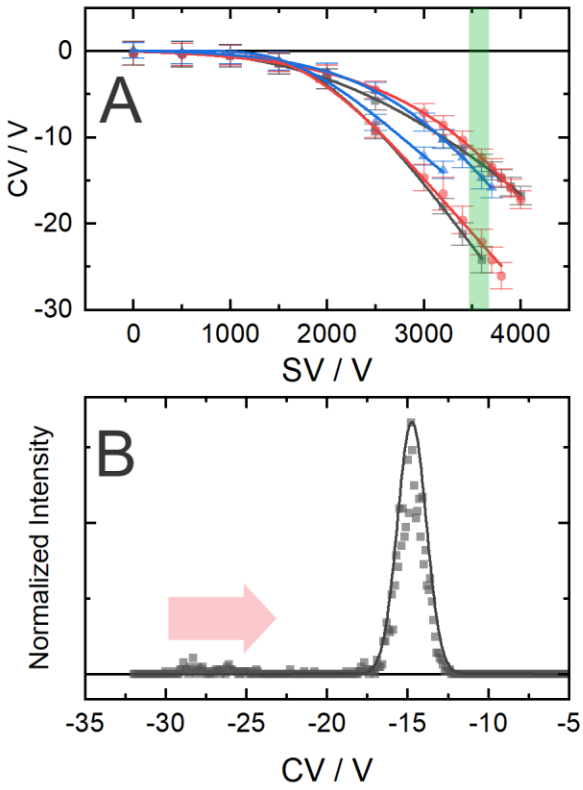

Figure A- 12. (**A**) Dispersion plots of $[CBD - H]^-$ taken under N_2 gas conditions seeded with 1.5% (*v/v*) IPA at T=150 °C (*black*), T=225 °C (*red*), and T=300 °C (*blue*). (**B**) The ionogram of $[CBD - H]^-$ under N_2 gas conditions seeded with 1.5% (*v/v*) IPA at T=150 °C and SV = 3800 V. As temperature is increased, the dominant peak does not change significantly in DMS behavior, while the minor peak trends towards weaker clustering.

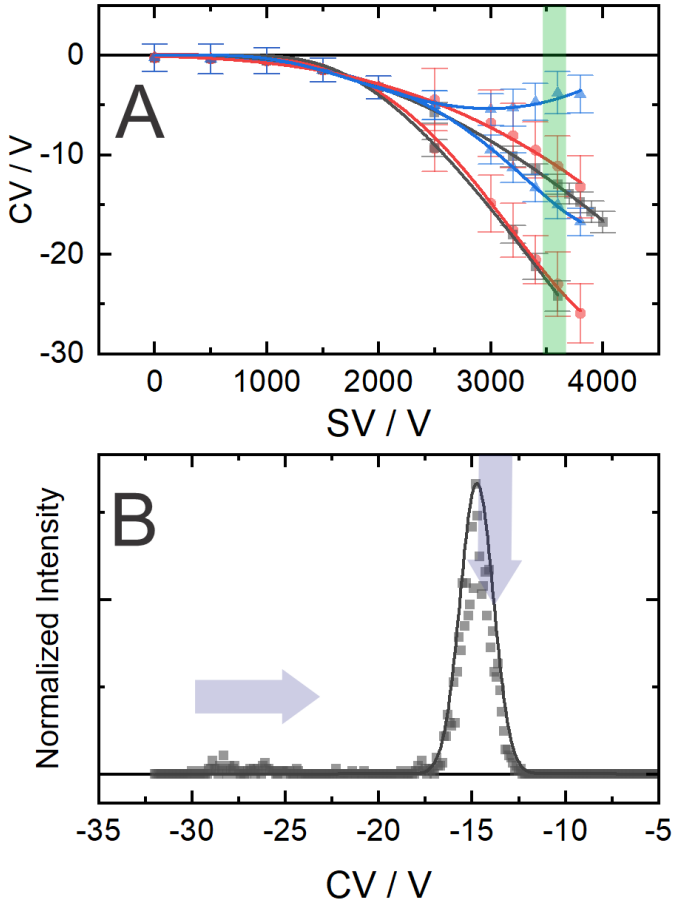

Figure A- 13. (**A**) Dispersion plots of $[CBD-H]^-$ taken under N_2 gas conditions seeded with 0.6% (*v/v*) IPA (*black*), 0.3% (*v/v*) IPA (*red*), and 1.5% (*v/v*) IPA (*blue*) at T=150 °C. (**B**) The ionogram of $[CBD-H]^-$ under N_2 gas conditions seeded with 1.5% (*v/v*) IPA at T=150 °C and SV = 3800 V. As the concentration of IPA reduces in the carrier gas, the dominant peak decreases in intensity while the minor peak shifts towards weaker clustering.

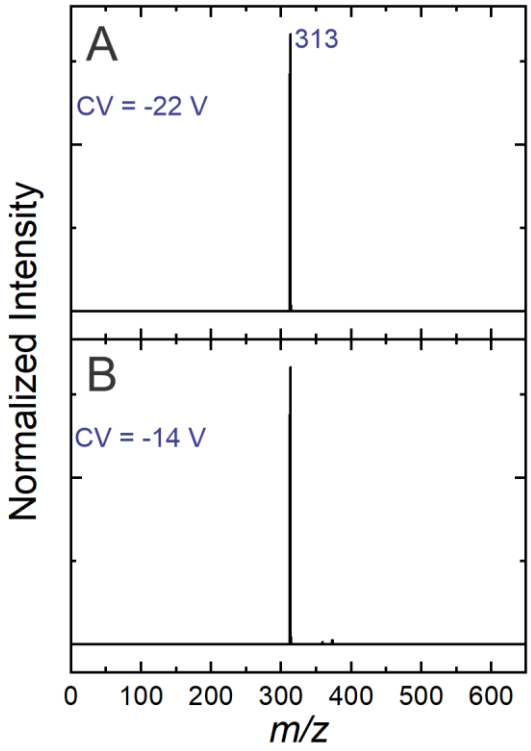

Figure A- 14. Precursor ion scans of peaks I and II taken at DcP set to 0 V for $[THC - H]^-$ in an N_2 carrier gas environment seeded with 1.5% (*v/v*) IPA at (**A**) CV = −22 V and (**B**) CV = −14 V. No *m/z* ion peak other than the parent ion mass is detected.

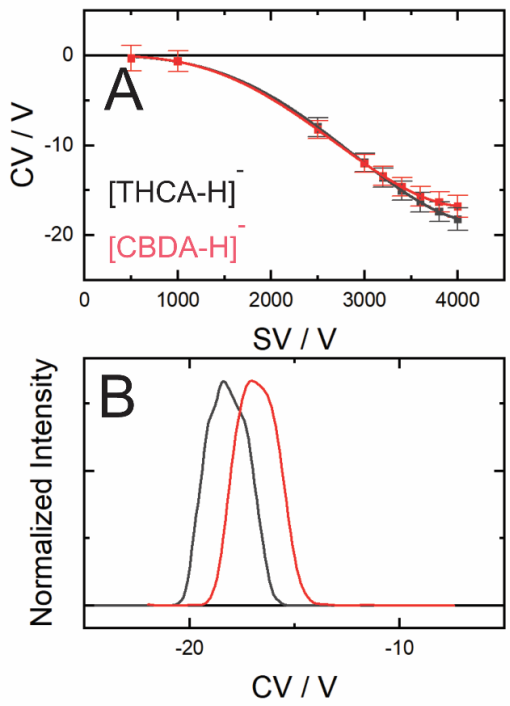

Figure A- 15. (**A**) Dispersion plots of deprotonated (−)-THCA (*black*) and CBDA (*red*) under an N_2 seeded with 1.5% (*v/v*) IPA at T = 150 °C shows inadequate separation at high SV. (**B**) An ionogram taken at SV = 4000 V of the two isomers with resolving gas shows insufficient separation at these conditions.

Table A- 3. Computed binding energies ($kJ\ mol^{-1}$)) of adducts formed between anionic cannabinoid molecules, $[M-H]^{-1}$, and neutral solvent molecules at T = 298 K.

Cannabinoid	Binding Energy				
	MeOH	MeCN	ACE	IPA	AA
Δ^9-THC	32.6	22.7	17.4	34.1	93.0
CBD	37.5	28.7	17.9	43.4	78.3
CBC	35.2	14.3	7.5	49.2	85.6
(−)-THCA	21.6	9.4	5.3	19.6	67.1
CBDA	10.6	10.1	2.3	11.8	37.1

A.6 Quantification of Cannabinoid Derivatives

The standard addition method for THCA yielded precise results, allowing for the quantification of THCA using this method. In the case of CBDA, due to the effect of ionization efficiency, the use of an internal standard is better suited for calibration, to account for the ionization efficiency occurring. An internal standard calibration curve is shown for the case of CBDA. Accurate measurements of CBDA were achieved using this method. A calibration plot of CBDA is also provided to determine the LOD and LOQ values using the separation methods employed.

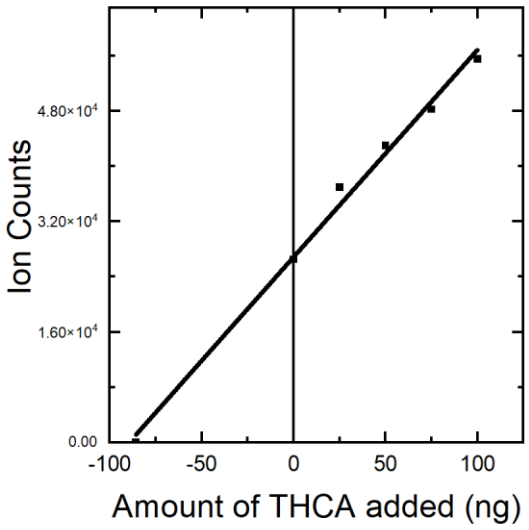

Figure A- 16. Standard addition calibration curve of THCA in marijuana flower extract Blueberry Haze

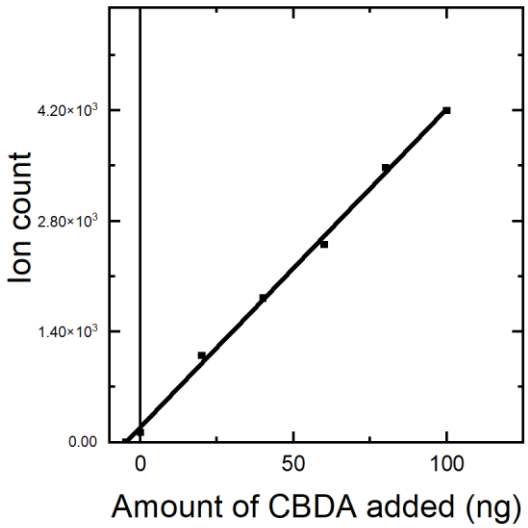

Figure A- 17. Standard addition calibration curve of CBDA in marijuana flower extract Blueberry Haze.

Table A- 4. LOD and LOQ of the proposed method and accuracy determination

Isomer	LOD (ng/mL)	LOQ (ng/mL)	R^2
(−)-THCA	13	41	0.993
CBDA	7	21	0.996

A second marijuana extra (Pure Sun) was acquired and extracted using the methods mentioned previously. A 200 ng/mL concentration of flower to solvent was used in the quantification of THCA and CBDA in the extract. The concentration of the two carboxylated isomers was determined using standard addition.

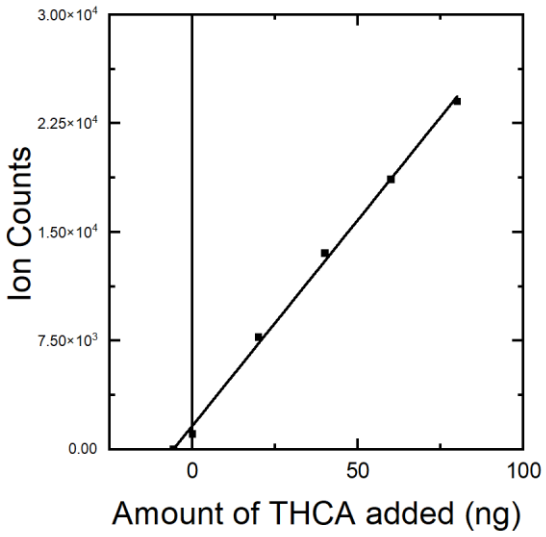

Figure A- 18. Standard addition calibration curve of THCA in marijuana flower extract Pure Sun.

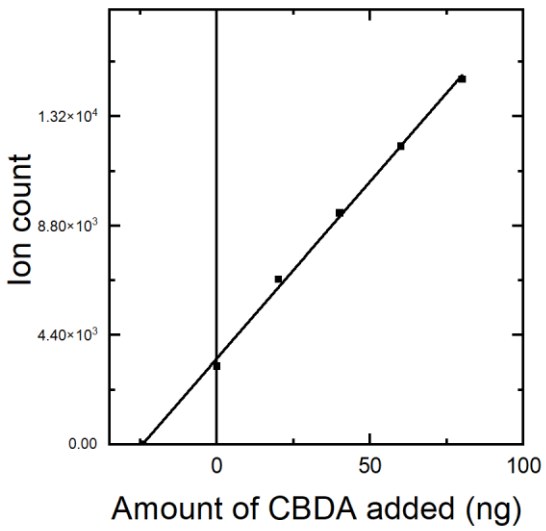

Figure A- 19. Standard addition calibration curve of CBDA in marijuana flower extract Pure Sun.

Table A- 5. Calculated results from quantification of Pure Sun Marijuana extract.

Isomer	Expected (*w*/w) Percentage (%)	Calculated (*w*/w) Percentage (%)	R^2
(−)-THCA	0-2	2.8 ± 0.06	0.997
CBDA	10-15	12.1 ± 0.2	0.997

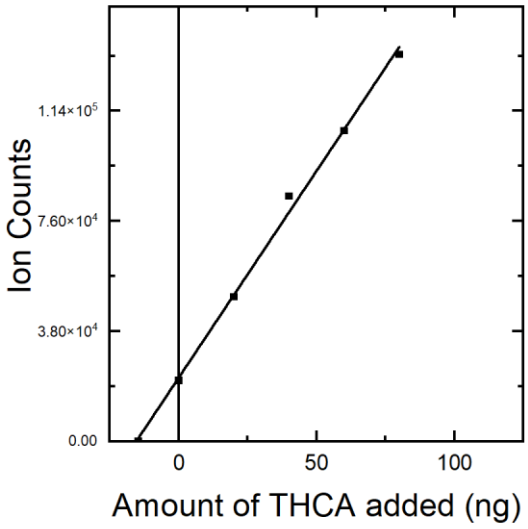

Figure A- 20. Standard addition calibration curve of THCA in marijuana flower extract Skunky Haze.

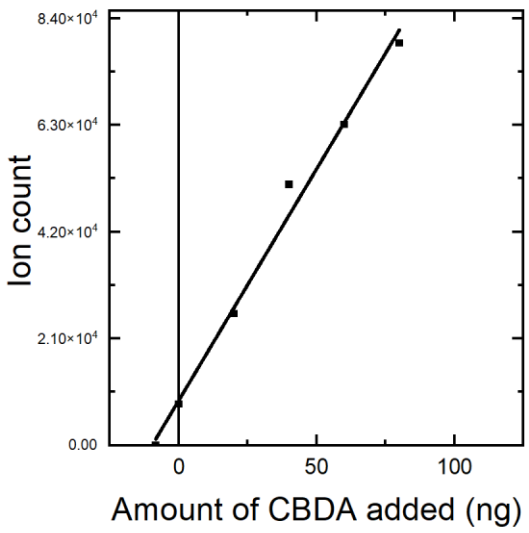

Figure A- 21. Standard addition calibration curve of CBDA in marijuana flower extract Skunky Haze.

Table A- 6. Calculated results from quantification of Skunky Haze Marijuana extract

Isomer	Expected (*w/w*) Percentage (%)	Calculated (*w/w*) Percentage (%)	R^2
(−)-THCA	7-12	7.3 ± 0.06	0.995
CBDA	7-12	4.2 ± 0.04	0.987

A.7 Quantification of the decarboxylated isomer sets

The amounts of THC, CBD, and CBC were negligible in the marijuana flower extract tested, as expected. To test the accuracy of quantifying these isomers using the developed method, a 1:1:1 standard mixture of a predetermined concentration of each isomer was measured in the DMS and quantified via standard addition. A summary of the accuracy of the quantification step is provided in Table A7.

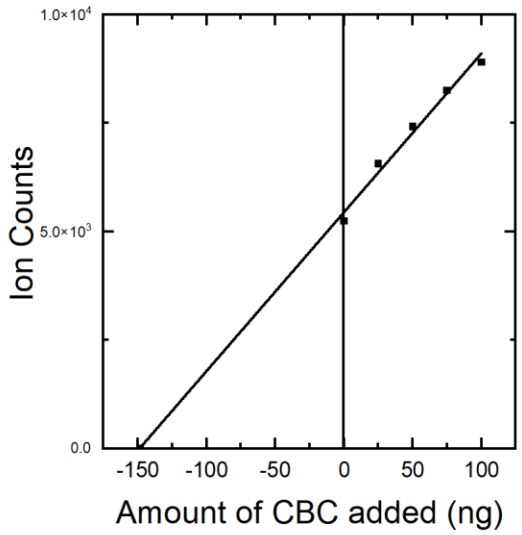

Figure A- 22. Standard addition calibration curve of CBC in standard mixture

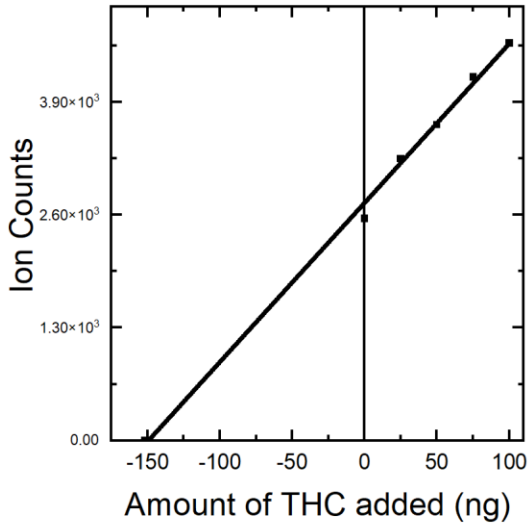

Figure A- 23. Standard addition calibration curve of THC in standard mixture.

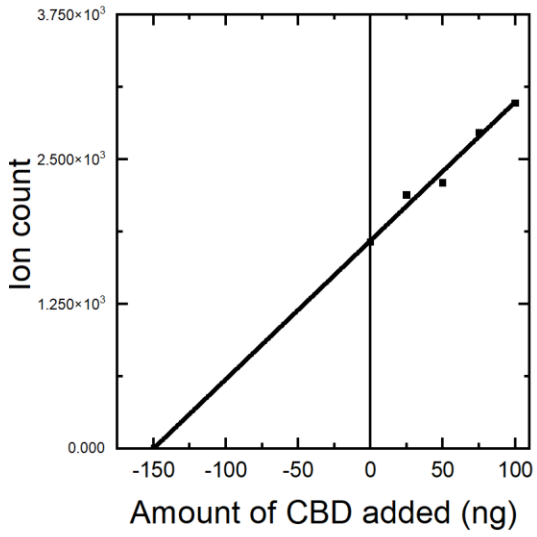

Figure A- 24. Standard addition calibration curve of CBD in standard mixture.

Table A- 7. Calculated results from quantification of THC, CBD, and CBC standard mixture.

Isomer	Concentration in Sample (ng/mL)	Measured Concentration (ng/mL)	LOD (ng/mL)	LOQ (ng/mL)	R^2
THC	150	152.0	7	23.9	0.990
CBD	150	149.0	18.9	57.2	0.978
CBC	150	148.2	18.4	55.7	0.982

A.8 XYZ Coordinates of Optimized Cannabinoid Isomer Structures

The XYZ coordinates of the optimized cannabinoid isomer structures can be found in the supplementary information belonging to the manuscript from which Chapter 3 and this appendix were reproduced. Details are given in the Statement of Contributions section.

Appendix B – The Study of Positional Isomers using DMS

B.1 Preliminary Experimental Results

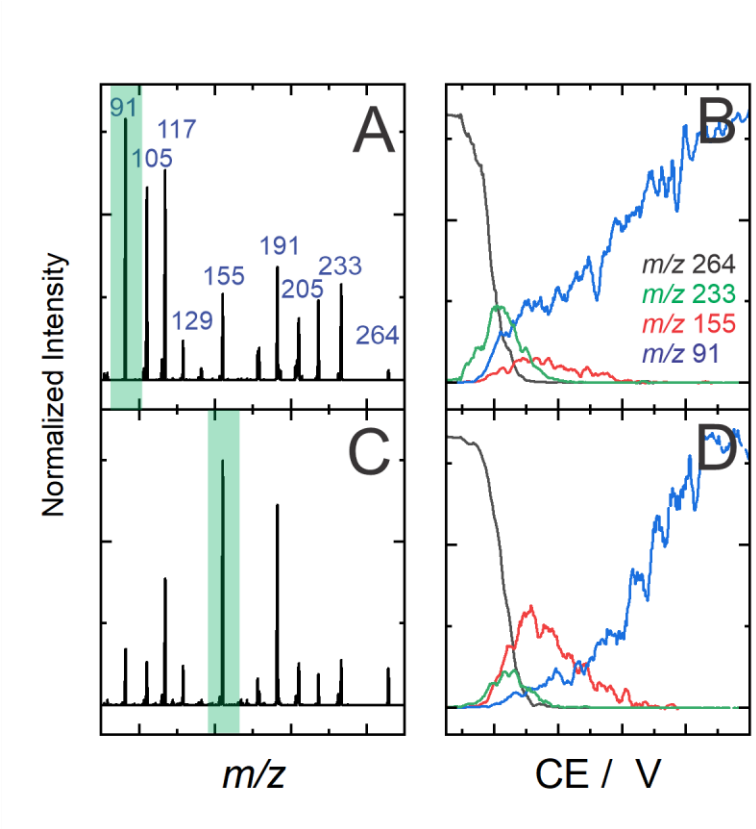

Figure B- 1. MS/MS spectra of (A) nortriptyline and (C) protriptyline at a collision energy of 30 V result in the same product ions varying only in relative intensity. Breakdown curves highlighting the main product ion channels are shown in B and D for nortriptyline and protriptyline, respectively.

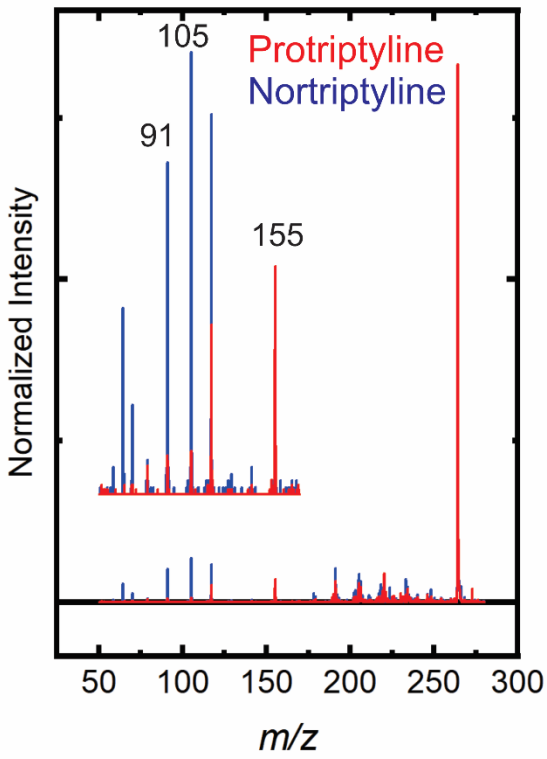

Figure B- 2. Mass spectra of (A) nortriptyline and (B) protriptyline of the product ions resultant from UV irradiation and photodissociation at 250 nm.

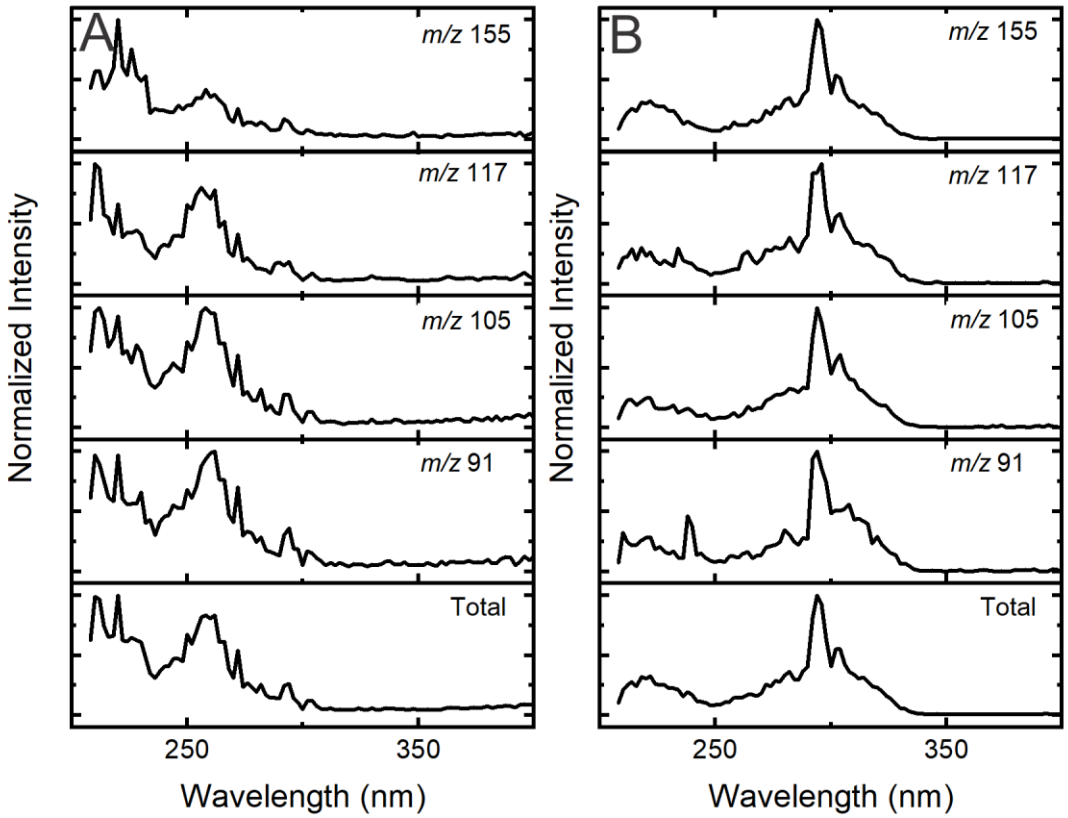

Figure B- 3. UVPD action spectra of the individual fragmentation channels explored shown for nortriptyline (A) and protriptyline (B). No difference in relative spectral band intensities is observed except for the case of the m/z 155 fragment, which showed a smaller intensity for the spectral band around 250 nm.

B.2 Additional Computational Results

Table B- 1. Computed binding energies (kJ mol^{-1}) of nortriptyline and protriptyline bound to $N = 1 - 3$ acetonitrile solvents.

Isomer	**Binding Energy ($kJ\ mol^{-}$)**		
	1MeCN	2MeCN	3MeCN
Nortriptyline	41.6	32.84	5.1
Protriptyline	50.2	27.6	9.7

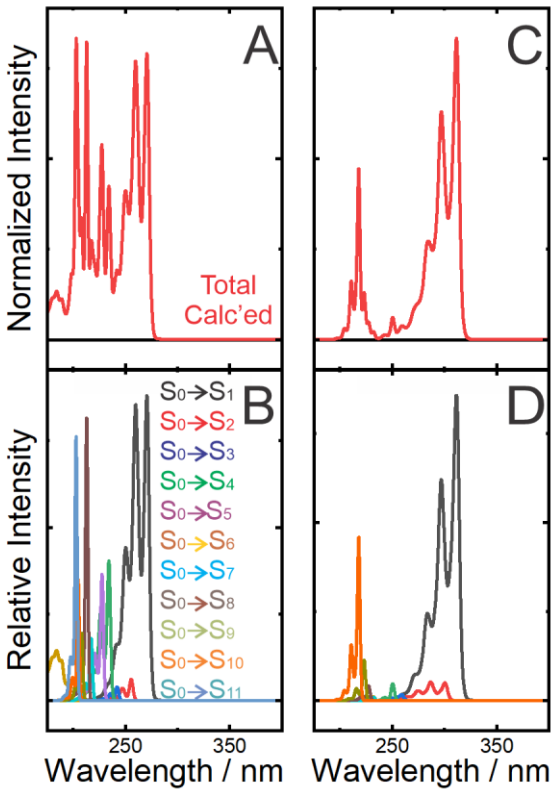

Figure B- 4. The calculated spectrum of nortriptyline (A) and protriptyline (C). The relative intensity of each excited state transition shown in (B) and (D) for nortiptyline and protriptyline, respectively, to determine the contribution of each excited state transition.

Table B- 2. Excited state calculations of the electronic transitions in Nortriptyline.

Transitions:	Wavelength (nm):	Electronic Oscillator Strength:
$S_0 \rightarrow S_1$	255.3	0.15911
$S_0 \rightarrow S_2$	248.4	0.08030
$S_0 \rightarrow S_3$	236.9	0.00133
$S_0 \rightarrow S_4$	227.5	0.01883
$S_0 \rightarrow S_5$	223.5	0.03441
$S_0 \rightarrow S_6$	221.3	0.03422
$S_0 \rightarrow S_7$	214.2	0.02242
$S_0 \rightarrow S_8$	209.1	0.04759
$S_0 \rightarrow S_9$	205.1	0.16327
$S_0 \rightarrow S_{10}$	202.5	0.12942

$S_0 \rightarrow S_{11}$	201.8	0.04425

Table B- 3. Excited state calculations of the electronic transitions in Nortriptyline.

Transitions:	Wavelength (nm):	Electronic Oscillator Strength:
$S_0 \rightarrow S_1$	294.5	0.13245
$S_0 \rightarrow S_2$	286.5	0.24187
$S_0 \rightarrow S_3$	259.3	0.00225
$S_0 \rightarrow S_4$	246.7	0.00271
$S_0 \rightarrow S_5$	240.0	0.00539
$S_0 \rightarrow S_6$	239.8	0.00220
$S_0 \rightarrow S_7$	232.8	0.00997
$S_0 \rightarrow S_8$	225.6	0.00389
$S_0 \rightarrow S_9$	224.0	0.02130
$S_0 \rightarrow S_{10}$	219.3	0.06299
$S_0 \rightarrow S_{11}$	218.1	0.02968

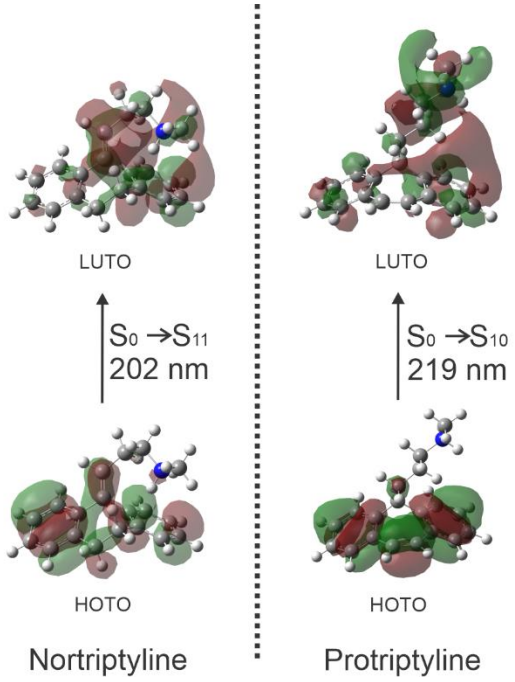

Figure B- 5. The excited state transitions responsible for the spectral band present around 200 nm for each isomer.

B.3 Optimized Geometries

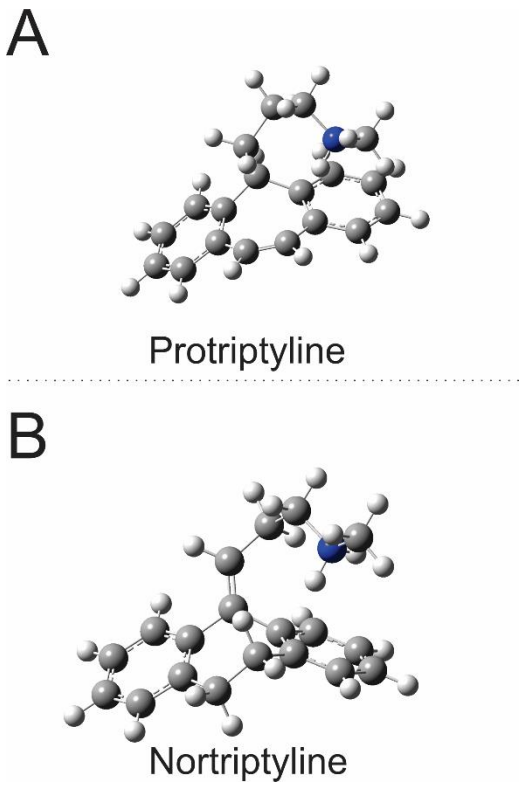

Figure B- 6. Optimized geometries of nortriptyline and protriptyline.

Appendix C – The Investigation of Rivaroxaban Prototropic Isomers

C.1 Experimental Conditions

Table C- 1. Instrumental parameters and conditions employed in this study.

Source/Gas Conditions			
Ion Source:	TurboSpray	**Temperature:**	34 ˚C
Curtain Gas:	20 psi	**Ion Source Gas 1:**	20 psi
Collision Gas:	High	**Ion Source Gas 2:**	0 psi
Polarity:	Positive Mode	**Ion Spray Voltage:**	5500 V
Compound Conditions			
Declustering Potential:	100.0 V	**Excitation Energy:**	0.100 V
Collision Energy:	30.0 V	**CE Spread:**	0.00 V
Entrance Potential:	10.0 V		
DMS Conditions			
DMS Temperature:	150 ˚C, 225 ˚C, 300 ˚C	**CV Ramp:**	0.1 V
DMS Offset:	−3.0 V	**Carrier Gas:**	100% N_2, N_2 with 1.5% (*v/v*) MeCN

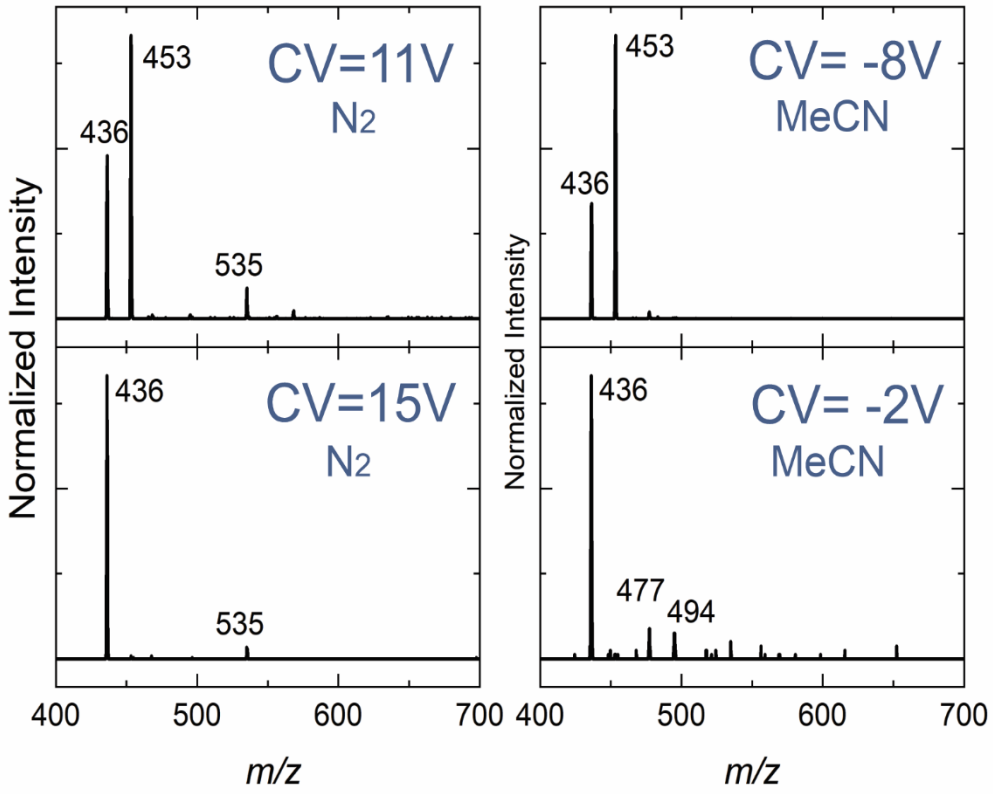

Figure C- 1. Precursor ion scans for ESI of Rivaroxaban in pure N2 environment at (top left) SV = 3600 V and CV = 11 V and (bottom left) SV = 3600 V and CV = 15 V. Precursor scans for ESI of Rivaroxaban in a modified MeCN environment at (top right) at SV = 3600 V and CV = −8 V and (*bottom right*) SV = 3600 V and CV = −2 V. Rivaroxaban-containing species were monitored via the m/z 436 → 145 MRM transition. The ion population at CV ≈ 11 V (top left) shows dominant mass peaks at $[M+H]^+$ and $[M+18]^+$, corresponding to protonated Rivaroxaban bare ion and a Rivaroxaban-ammonium adduct, respectively. The ammonium adduct is also present in the ion population eluting at SV = 3600 V and CV = −8 V (top right) in the modified MeCN environment. No significant adduct formation was observed for the peaks eluting at SV = 3600 V and CV = 15 V in N_2 or at SV = 3600 V and CV = −2 V in the MeCN-modified environment. However, an *m/z* 477 peak found at SV = 3600 V and CV = −2 V confirms the presence of a $[M+H+MeCN]^+$ cluster.

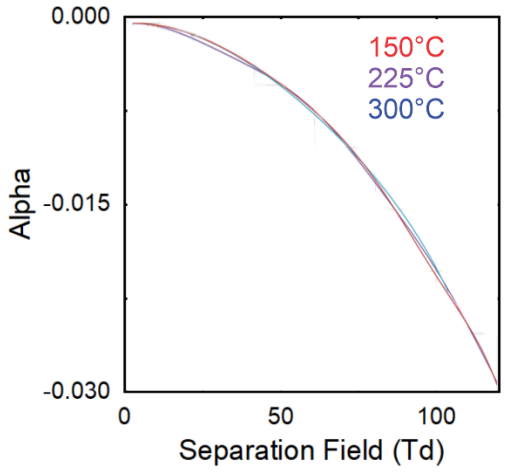

Figure C- 2. Alpha curve plot of the ion population eluting at SV = 3600 V and CV = 15 V in pure N2 environment (T = 225 °C). The values of the DMS temperature used in the calculation were modified to account for the effective temperatures, changing the DMS temperature to 111 °C for 150 °C, 145 for 225 °C, and 190 °C for 300 °C.

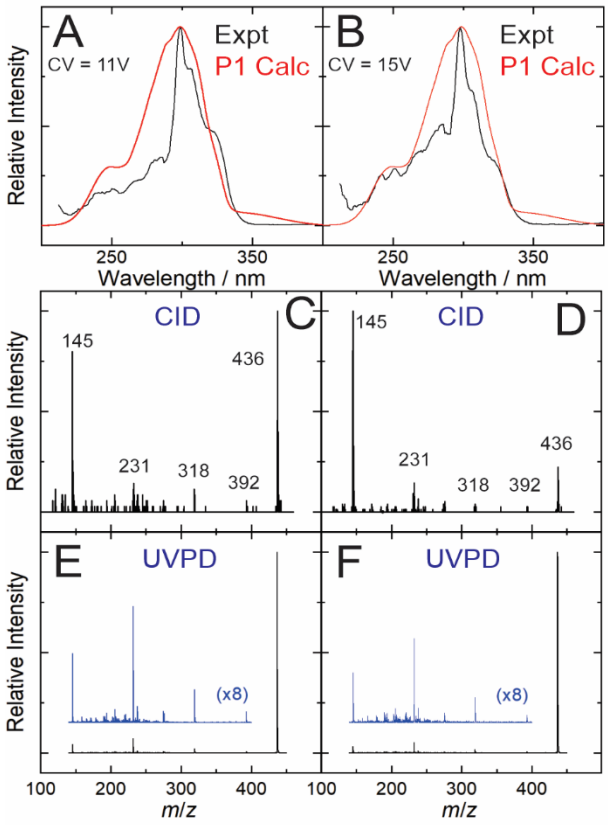

Figure C- 3. The UVPD action spectra of the Rivaroxaban ion populations isolated at (A) SV = 3600 V, CV = 11 V and (B) SV = 3600 V, CV = 15 V in the pure N2 environment. The UVPD mass spectra observed when gating on the ion population at (C) SV = 3600 V, CV = 11 V and (**D**) SV = 3600 V, CV = 15 V in the MeCN-modified environment. Both ion populations exhibit identical UPVD spectral features.

C.2 Rivaroxaban Product Ion Fragment Identification

Table C- 2.The m/z of the most abundant Rivaroxaban fragment ions and the corresponding assignment.

Fragment *m/z:*	Product Assignment:
392	$[M+H-CO_2]^+$
318	$[M+H-C_4H_3SCl]^+$
231	$[M+H-C_6H_4NO_3SCl]^+$
145	$[M+H-C_{14}H_{17}N_3O_4]^+$

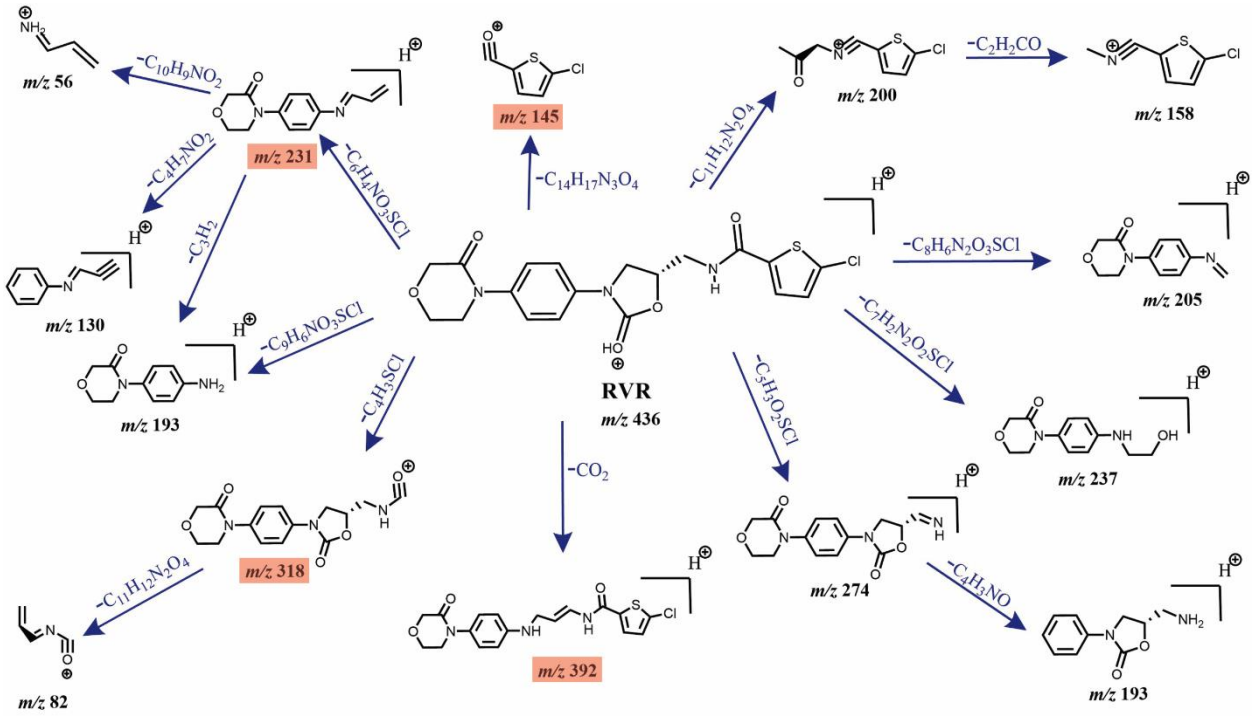

Figure C- 4. The fragmentation pathway of protonated Rivaroxaban and resultant fragment ions. Fragments observed during the CID and UVPD process are highlighted in red.

C.3 Additional Experimental Figures

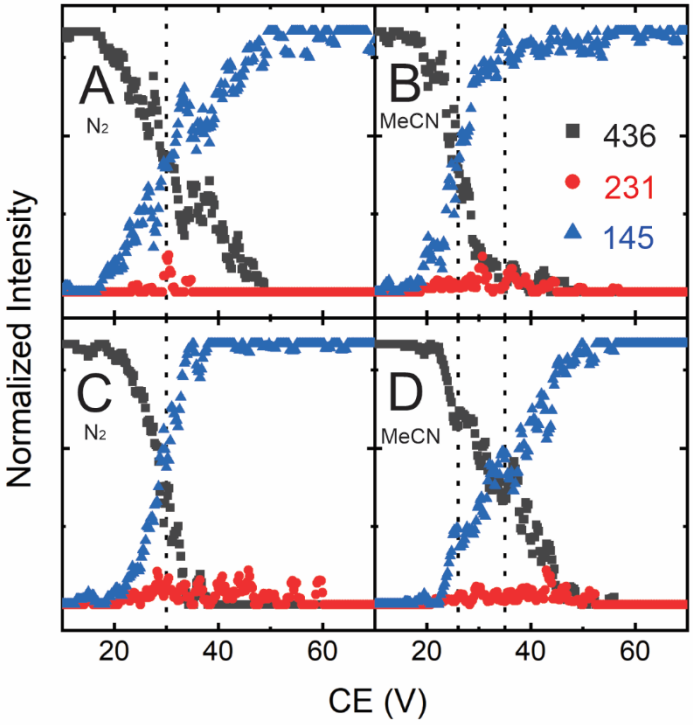

Figure C- 5. Breakdown curves of the ion populations separated in a pure N2 environment at (A) SV = 3600 V and CV = 11 V and (C) SV = 3600 V and CV = 15 V. Breakdown curves of the ion populations separated in 1.5% (v/v) MeCN at (B) SV = 3600 V and CV = -8 V and (D) SV = 3600 V and CV = −2 V. The *m/z* 145 fragment corresponds to the dominant ion for each breakdown curve. Relatively little amounts of the *m/z* 231 product were produced, and trace amounts of other fragmentation products were observed.

C.3.1 UVPD Spectra from Individual Product Channel

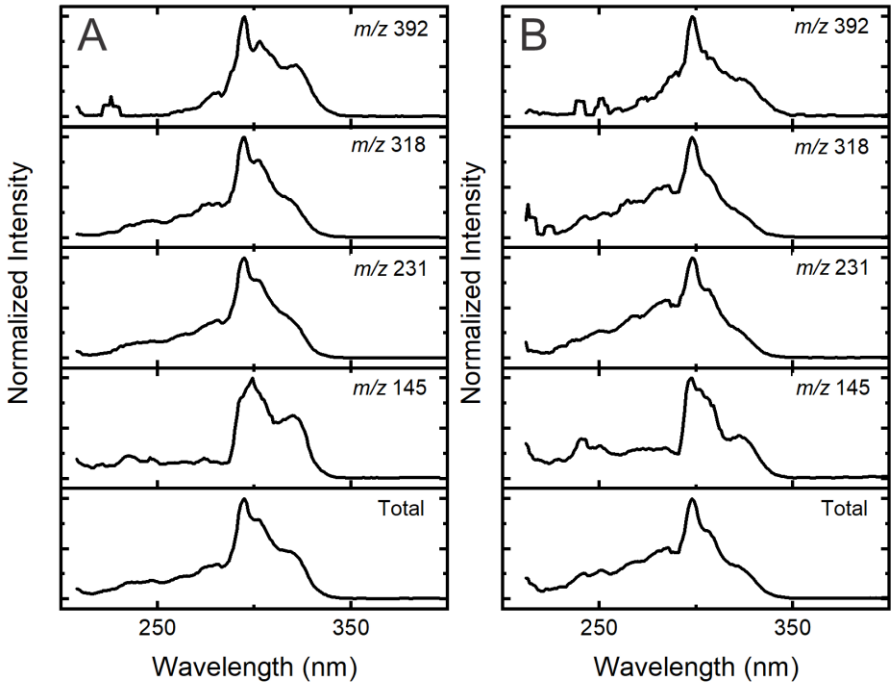

Figure C- 6. UVPD spectra observed via individual product channels of protonated Rivaroxaban following mass- and mobility-selection of ion populations eluting at (A) SV = 3600 V and CV = 11 V and (B) SV = 3600 V and CV = 15 V in a pure N_2 environment.

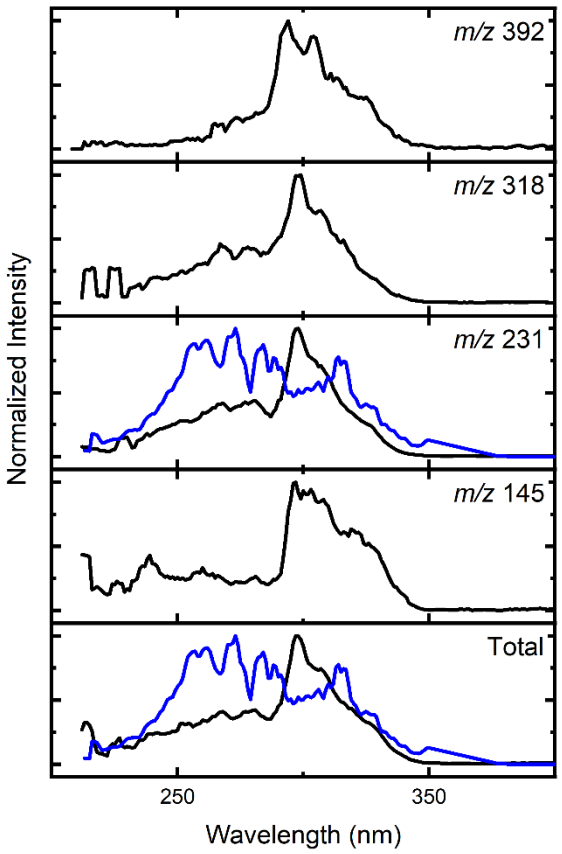

Figure C- 7. UVPD spectra for each product channel observed following separation in the MeCN-modified environment eluting at (black curves; Peak I) SV = 3600 V and CV = -8 V and (*blue curves*; Peak II) SV = 3600 V and CV = −2 V. The individual UVPD spectra for *m/z* 145, 318, and 392 suffer from poor signal-to-noise ratio owing to low signal intensity; these were too weak to be recorded for Peak II.

C.3.2 Additional Computational and Excited State Dynamics Results

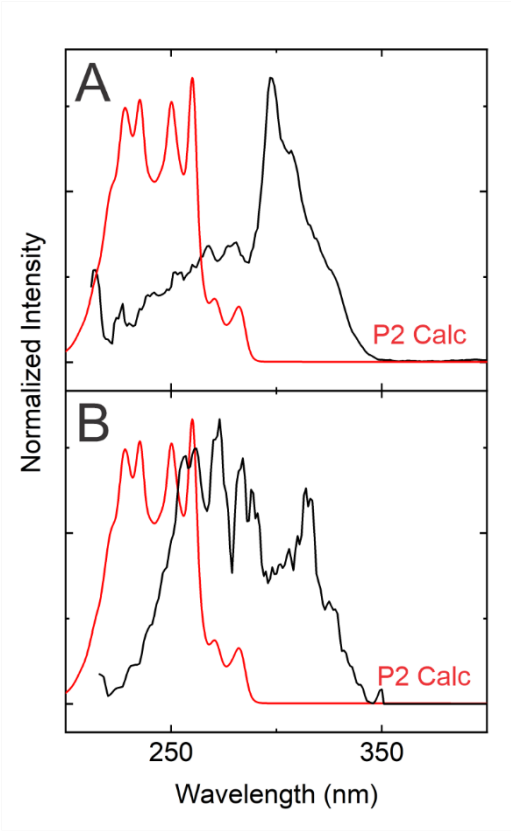

Figure C- 8. Comparison between calculated vibronic spectrum of P2 (in red) and experimental UVPD action spectra acquired in a modified MeCN environment at (**A**) SV = 3600 V and CV = −8 V and (**B**) SV = 3600 V and CV = −2 V.

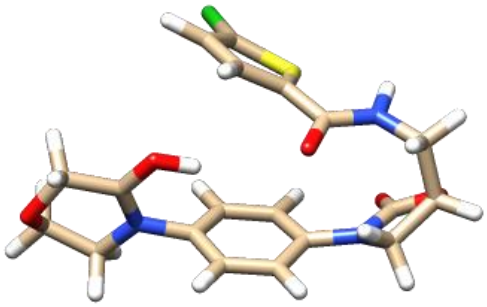

Figure C- 9. Optimized geometry of the P1 and P2 transition state shows a slightly more folded geometry than the P2 isomer. The calculated transition state structure is 13 kJ/mol higher in energy than P2.

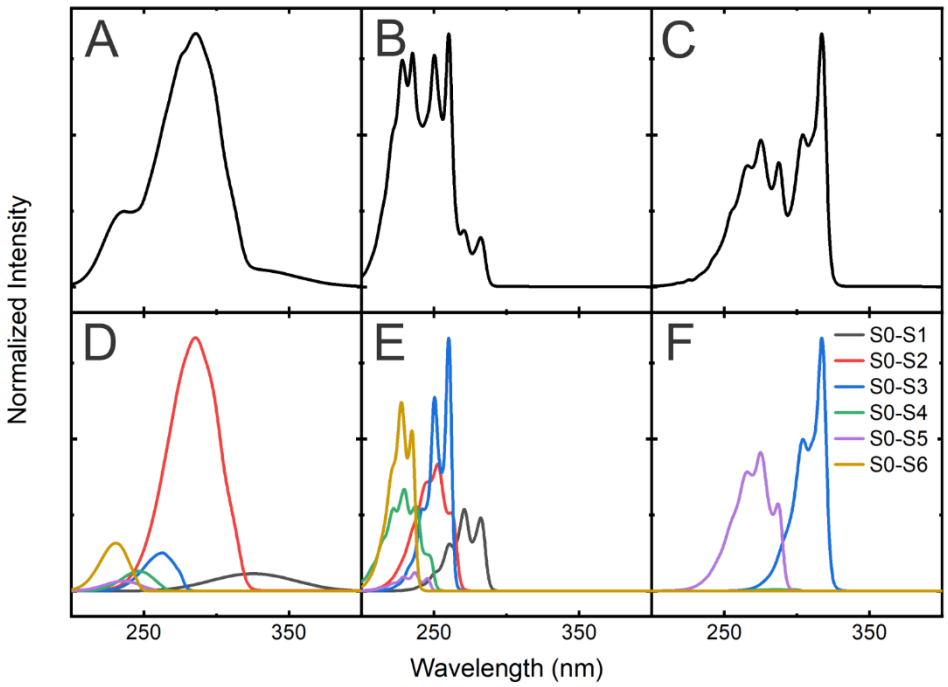

Figure C- 10. The total simulated vibronic spectra generated for (**A**) P1, (**B**) P2, and (**C**) P3, and the individual band intensities of the corresponding transitions (**D -E**, respectively).

Table C- 3. Excited state calculations of the electronic transitions for P1 and the NTO analyses for each.

Transitions:	Electronic Oscillator Strength:	Contribution of Orbital Transitions:		
		HOMO → LUMO	[HOMO − 1] → [LUMO + 1]	[HOMO − 2] → [LUMO + 2]
$S_0 \rightarrow S_1$	0.05856	0.9938	0.0035	0.0011
$S_0 \rightarrow S_2$	0.26911	0.9736	0.01350	0.0096
$S_0 \rightarrow S_3$	0.03822	0.9626	0.0229	0.0106
$S_0 \rightarrow S_4$	0.00266	0.5774	0.4190	0.0057
$S_0 \rightarrow S_5$	0.01005	0.7381	0.2549	0.0053
$S_0 \rightarrow S_6$	0.24063	0.8336	0.1362	0.0131

* Note that vibronic intensities differ from electronic transition intensities owing to Franck Condon overlap

Table C- 4. Excited state calculations of the electronic transitions in P2 and the NTO analyses for each.

Transitions:	Electronic Oscillator Strength:	Contribution of Orbital Transitions:		
		HOMO → LUMO	[HOMO − 1] → [LUMO + 1]	[HOMO − 2] → [LUMO + 2]
$S_0 \rightarrow S_1$	0.02633	0.8166	0.1548	0.0168
$S_0 \rightarrow S_2$	0.20706	0.7181	0.2436	0.0179
$S_0 \rightarrow S_3$	0.02799	0.7168	0.1466	0.1283
$S_0 \rightarrow S_4$	0.06202	0.8699	0.0944	0.0291
$S_0 \rightarrow S_5$	0.10085	0.7340	0.2096	0.0304
$S_0 \rightarrow S_6$	0.06585	0.6471	0.2832	0.0563

Table C- 5. Excited state calculations of the electronic transitions in P3 and the NTO analyses for each.

Transitions:	Electronic Oscillator Strength:	Contribution of Orbital Transitions:		
		HOMO → LUMO	[HOMO − 1] → [LUMO + 1]	[HOMO − 2] → [LUMO + 2]
$S_0 \rightarrow S_1$	0.00140	0.9992	--	--
$S_0 \rightarrow S_2$	0.00008	0.9999	--	--
$S_0 \rightarrow S_3$	0.46573	0.9797	0.0148	0.0076
$S_0 \rightarrow S_4$	0.00324	0.9983	0.0015	--
$S_0 \rightarrow S_5$	0.00003	0.9992	--	--

$S_0 \rightarrow S_6$	0.04285	0.9861	0.0151	0.0080

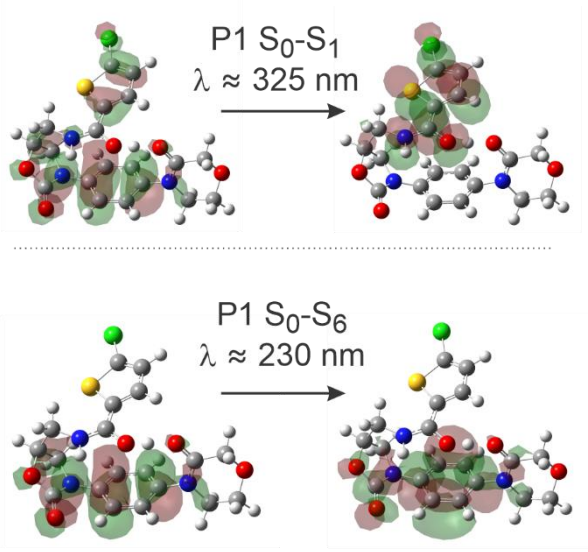

Figure C- 11. The highest occupied transition orbital (HOTO) and lowest unoccupied transition orbital (LUTO) of the (*top*) $S_0 \rightarrow S_1$ and (*bottom*) $S_0 \rightarrow S_6$ electronic transitions of the P1 isomer. The $S_0 \rightarrow S_1$ transition is not observed in the UVPD action spectrum.

C.4 Geometries of Optimized Structures

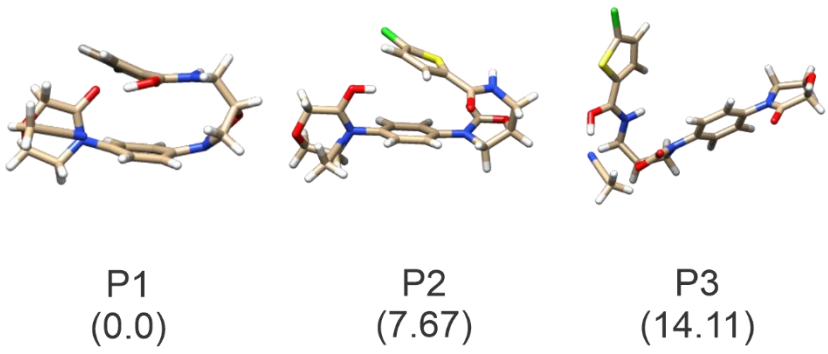

Figure C- 12. Optimized geometries of the protonated Rivaroxaban prototropic isomers, singly solvated with MeCN.

C.4.1 XYZ Coordinates of Optimized Structures

The XYZ coordinates of all optimized geometries can be found on the supplementary information document corresponding to the article reproduced in Chapter 4. Please refer to the Statement of Contributions for citation into the article.